

PHOTOLUMINESCENCE AND SURFACE PHOTOVOLTAGE STUDIES OF DEFECTS AT
NANOSCALE SURFACES AND INTERFACES IN THIN FILMS OF ZnO, TiO₂ AND
DIAMOND

by

ANASTASIIA NEMASHKALO

Bachelor of Science, 2009
V. N. Karazin Kharkiv National University
Kharkiv, Ukraine

Submitted to the Graduate Faculty of College of Science and Engineering
Texas Christian University
in partial fulfillment of the requirements
for the degree of

Doctor of Philosophy

August 2014

Acknowledgements

I would like to deeply thank my advisor Dr. Yuri Strzhemechny for guidance, patience, accessibility and especially for teaching me to think independently. His thoughtful mentorship throughout these years helped me grow both as a professional and a personality.

I also want to thank Dr. Waldek Zerda for useful advice, help with Energy lab course and lab equipment in general.

I certainly express my gratitude to all the physics faculty and graduate students. I want to thank TCU in general for the outstanding opportunity to obtain education here.

I am grateful to D. Yale (TCU Machine Shop) for help in machining vacuum chamber parts and J. Katchinska (TCU Electronics Shop) for help with troubleshooting electronics in the lab.

I would also like to thank our collaborators in Prof. Kulish's group for the titanium dioxide containing thin films, Prof. Chabanov's group for ZnO ALD-grown thin films, and Dr. Gupta for diamond thin films.

Contents

Acknowledgements.....	ii
Contents	iii
List of Figures.....	v
List of Tables.....	ix
List of Abbreviations.....	x
1. Introduction	1
1.1 Titanium Dioxide (TiO ₂)	4
1.2 Zinc Oxide (ZnO)	12
1.3 Diamond.....	15
2. Experimental.....	18
2.1 Surface Photovoltage Spectroscopy.....	18
2.2 Photoluminescence Spectroscopy.....	24
2.3 Auger Electron Spectroscopy.....	29
3. Optical studies of electronic band structure in sol-gel anatase TiO ₂ modified by Ag, Au, ZrO ₂ , and Ti ⁺ -irradiation.....	33
3.1 Thin film growth	33
3.2. Stoichiometry and crystal structure of the samples	34
3.3 Electronic structure of the samples.....	37
TiO ₂	37
TiO ₂ /Ag.....	43
TiO ₂ /Au.....	48
TiO ₂ /ZrO ₂	53

3.4 Effects of Ti^+ irradiation (self-doping).....	58
4. Studies of optoelectronic characteristics of ZnO homoepitaxial thin films grown by atomic layer deposition.....	62
5. Optoelectronic surface-related properties in boron-doped and irradiated diamond thin films..	75
6. Conclusions	88
7. Future Work.....	92
References.....	94

VITA

ABSTRACT

List of Figures

Figure 1. Photocatalysis mechanism.....	6
Figure 2. Crystal structure of anatase TiO ₂ . gray – Ti; red – O.....	7
Figure 3. Principle of photoluminescence.....	25
Figure 4. Basic principle of AES spectroscopy.....	30
Figure 5. XRD spectra of TiO ₂ films before (black) and after (red) Ti ⁺ irradiation. Inset shows slight broadening and shift of the (101) anatase peak after irradiation.....	34
Figure 6. AES spectrum of TiO ₂ /Ag film after remote plasma cleaning.....	35
Figure 7. Content of carbon at the surface of a trial sample as a function of Ar plasma treatment time.....	36
Figure 8. Band diagram of the anatase TiO ₂ thin film based on the SPV (left) and low temperature PL results (right).....	39
Figure 9. SPV spectra of a TiO ₂ thin film showing transitions at 1.2 eV, 2.0 eV and a weak transition at ~ 1.4 eV are shown.....	40
Figure 10. Low temperature (8 K) spectrum of the TiO ₂ thin film.....	41
Figure 11. Band diagrams of TiO ₂ and TiO ₂ /Ag samples.....	43
Figure 12. (A) SPV spectra for the TiO ₂ /Ag film showing transitions at 1.3 eV, 1.5 eV into the conduction band and 1.4 eV and 1.8 eV from the valence band. (B) Transition at 2.8 eV from the valence band and the bandgap transition at ~ 3.7 eV.....	44
Figure 13. SPV transitions at ~ 1.8 eV and ~ 2.2 eV from VBM in the TiO ₂ /Ag film.....	45
Figure 14. PL spectra measured at 8 K for the TiO ₂ film (left) and the TiO ₂ /Ag film (right).....	46

Figure 15. Relative intensities and spectral locations of the low temperature PL bands in the TiO ₂ and TiO ₂ /Ag thin films. The values on the y-axis represent intensities of individual peaks, normalized to the total intensity.....	48
Figure 16. Band diagrams of TiO ₂ and TiO ₂ /Au films.....	49
Figure 17. SPV spectra of TiO ₂ /Au film.....	50
Figure 18. PL spectra of TiO ₂ and TiO ₂ /Au films, measured at 8K.....	51
Figure 19. Normalized intensities and spectral locations of low temperature PL peaks for TiO ₂ and TiO ₂ /Au thin films.....	52
Figure 20. Band diagrams of TiO ₂ and TiO ₂ /ZrO ₂ based on SPV and low temperature PL results.....	53
Figure 21. SPV spectra of TiO ₂ /ZrO ₂ . The transitions shown are (A) 1.2 eV into the conduction band (B) 1.4 eV from the valence band and (C) a relatively weak transition at 2.0 eV from the valence band.....	54
Figure 22. SPV spectrum of TiO ₂ /ZrO ₂ showing the bandgap transition at ~ 3.6 eV.....	55
Figure 23. PL spectra of TiO ₂ and TiO ₂ /ZrO ₂ taken at 8K temperature.....	57
Figure 24. Normalized intensities and spectral locations of the PL bands, resolved in the spectra of Figure 23.....	57
Figure 25. Comparison between low temperature PL spectra of the self-doped (A) TiO ₂ and (B) TiO ₂ /Au films. No significant changes are observed after Ti ⁺ -irradiation.....	58
Figure 26. SPV transition at 1.4 eV observed in TiO ₂ /ZrO ₂ and TiO ₂ /Ag after Ti ⁺ irradiation...	60
Figure 27. The SPV transition at ~ 1.7-1.8 eV observed in TiO ₂ /Ag film before and after Ti ⁺ irradiation.....	60
Figure 28. TEM image of ZnO thin film grown on O-face ZnO substrate at 150°C showing columnar growth and structural defects.....	63

Figure 29. Low temperature (left) and room temperature (right) PL spectra of the ZnO thin film ALD-grown at 150 °C.....	64
Figure 30. SPV spectrum of the ZnO film grown on a ZnO substrate at 150°C.....	65
Figure 31 (A). Temperature dependence of the BEx peaks for the sample grown at 150°C in the 10 K - 55 K temperature range with a 5 K increment.....	66
Figure 31 (B). Temperature dependence of the excitonic peak positions for the sample grown at 150°C.....	66
Figure 32. Temperature dependence of the intensity of the bound excitonic peak I_7 for the ZnO thin film grown at 150°C. The fit (red curve) to the theoretical dependence in Eq. 2 yields activation energy indicated in the graph	68
Figure 33. Low temperature PL spectrum of the ZnO film grown at 150°C demonstrating phonon replicas of the excitonic peaks and the ~ 3.33 eV peak related to the due to excitons bound to extended defects.....	69
Figure 34. Low temperature (left) and room temperature (right) PL spectra of the ZnO thin films grown at three different temperatures.....	70
Figure 35. Temperature dependence of the excitonic peak positions for ZnO thin films ALD-grown at three different temperatures. The same red shifts are observed regardless of the growth temperature.....	70
Figure 36. Temperature dependence of the intensity of the I_7 BEx peak for the ZnO thin films grown at 120°C, 150°C and 200°C. The fits (red curves) to the theoretical dependence yield the activation energies indicated in the graphs.....	71
Figure 37. Low temperature PL spectra of the three ZnO films grown at different temperatures demonstrating the phonon replicas of the excitonic peaks and a varying relative intensities of the ~ 3.33 eV peak related to the excitons bound to structural defects.....	72

Figure 38. The visible luminescence range in the room temperature PL spectra of the ZnO samples grown at three different temperatures.....74

Figure 39. SEM images of the diamond thin film samples studied.....77

Figure 40. SPV transition for the surface state 3.1–3.2 eV above the top of the valence band for the samples 19B-4, 23B, and 27-1.....80

Figure 41. Undulations in the SPV spectrum of the UNCD sample. The inset diagram illustrates possible explanation of the undulations due to thin film interference.....81

Figure 42. Visible parts of the low temperature (8 K) PL spectra for the 19B-4, 23B, Micro-diamond, 19B-1, 27-1, and SG10 samples. Also shown is fitting obtained for each spectrum by a superposition of three Gaussian peaks at 2.4, 2.9, and 3.1 eV.....83

Figure 43. Dependence of the relative intensity of the PL band at 3.1 eV on the grain surface-to-volume ratio for three groups of diamond thin films – undoped, MPACVD-, and HFCVD-doped. The trend for the increase of the relative intensity of this feature with the decrease of the grain size is probably due the relative surface abundance the sp^2 C clusters.....84

Figure 44. Temperature dependence of the PL spectra for the micro-diamond sample in the near-UV range featuring two narrow lines at 3.32 and 3.37 eV.....86

Figure 45. Low temperature (10 K) PL spectrum (left) of the TiO₂ film (right) synthesized in our lab.....92

List of Tables

Table 1. Gap states related to TiO ₂ reduction and observed in TiO ₂ using various experimental methods or theoretical calculations (CBM –Conduction band minimum; VBM – Valence band maximum).....	9
Table 2. Description of studied diamond thin films	76

List of Abbreviations

ALD – Atomic Layer Deposition

BEx – Bound Exciton

CBM – Conduction Band Minimum

CPD – Contact Potential Difference

CVD – Chemical Vapor Deposition

DFT – Density Functional Theory

EG – Electron Gun

FEx – Free Exciton

HFCVD – Hot-Filament Chemical Vapor Deposition

HR TEM – High Resolution Transmission Electron Microscopy

LT – Low Temperature

MPACVD – Microwave Plasma-Assisted Chemical Vapor Deposition

PC - Photocatalytic

PL – Photoluminescence (Spectroscopy)

RP – Remote Plasma

RSM – Reciprocal Space Mapping

SEM – Scanning Electron Microscopy

SPV – Surface Photovoltage (Spectroscopy)

STE – Self-Trapped Excitons

SCR – Space Charge Region

VBM – Valence Band Maximum

XRD – X-Ray Diffraction

UHV – Ultra High Vacuum

Chapter 1

1. Introduction

Currently two large groups of technological materials – oxides and nanocarbons – are at the focus of major research efforts, both fundamental and applied. The scope of the existing and potential applications of these materials includes optoelectronics, biotechnology, energy generation and storage, industrial chemistry, etc. In particular, nanotechnology applications garner a growing share of the market, with oxides and nanocarbons being among the most versatile and impactful components in biosensors, data storage, optoelectronic devices, etc.¹⁻³ However, the fundamental properties of nanocarbons and nanooxides are far from being well-understood.

With the reduction in size, the surface of the material becomes increasingly important since it comprises a larger part of the material as a whole. In particular, since the surface-to-volume ratio increases significantly in such systems, surface itself becomes the determining factor in the properties of the system. In this regard, understanding of many underlying surface-related phenomena is still missing and requires systematic studies. Free surface is often associated with defects, which essentially are formed due to termination of the periodic structure of the solid. These defects most of the time induce energy levels within the semiconductor's forbidden gap, and such states, in turn, influence many properties of a material. In our work we focus our interest on the surface defect properties of thin films of such representatives of oxide and nanocarbon materials as titanium dioxide, zinc oxide and diamond. The abundance and energetics of intrinsic and/or extrinsic localized gap states in these materials has significant impact on their performance in specific applications.

Defects may be introduced both intentionally and unintentionally during synthesis and processing of nanomaterials. Oxygen vacancies (V_o) are a good example of point defects frequently encountered in metal oxides, including systems studied here – TiO_2 and ZnO . In these materials oxygen deficiency may unintentionally arise as a result of annealing, electron bombardment and UV irradiation.⁴ In TiO_2 ⁴ and arguably in ZnO ⁵ defects associated with oxygen deficiency provide the basis for the *n*-type conductivity. These defects also act as color centers and cause absorption of certain wavelengths (see Refs. 6 and 7 for TiO_2 and ZnO respectively). On the other hand intentional introduction of defects (defect engineering) is commonly used to tailor the desired properties of materials via such approaches as extrinsic and intrinsic doping, employing ion implantation, irradiation, etc. Such modifications result in induced gap states, modified bandgap values, structural/phase transformations, which, in turn, affect the macroscopic properties: free carrier concentration, conductivity type, magnetic characteristics, etc. The three materials studied here represent examples of how manipulations with the content and type of defects during growth or post-growth treatments can be used to tailor their application-specific properties.

In TiO_2 systems studied here we show that native defects in combination with dopants can be used to control its electronic structure. Indeed, this material has to be sensitized to visible light in order to be an efficient visible light photocatalyst. This issue is addressed via intentional doping. Specifically, native defects play a large role in visible light sensitization of TiO_2 . While significant number of studies exists on the ways to sensitize TiO_2 to visible light, a lot of questions remain unanswered. In particular, modifications of TiO_2 with zirconia, silver and gold were reported to improve its photocatalytic properties. However, effects of such modifications on electronic structure of TiO_2 and the role of native defects in such systems were not studied.

In an attempt to elucidate such effects, we performed systematic experimental studies of TiO₂ thin films containing zirconia, silver and gold nanophases. We obtained a clear picture of the effects of these “dopants” on the electronic structure of TiO₂.

In addition to oxygen vacancies, a variety of other unintentionally introduced defects may exist in the solid: Native or extrinsic interstitials, dangling bonds, extended defects such as dislocations, stacking faults, shear planes, etc. It should be noted that one or another type of defects could be either beneficial or detrimental depending on a specific application of the material in question. As opposed to the case of TiO₂ where the native defects can enable visible light sensitization, in ZnO thin films studied here it is desirable to minimize the occurrence of defects. If present, these defects reduce the quality of the material and hinder its applications in flexible electronics, memory elements, photodetectors, and displays. Defects hold back realization of *p*-type doping of ZnO as well as fabrication of *p-n* homojunctions. It is suggested that atomic layer deposition (ALD) could be a suitable technique to grow a ZnO *p-n* homojunction. To verify this it is necessary to establish the overall quality of the resulting ZnO layers ALD-grown on ZnO substrates as well as to obtain information about the nature of defects and establish optimum conditions for obtaining films with a minimal concentration of defects. To address this in our studies, we characterized homoepitaxial ALD thin films of ZnO to confirm their high quality and also to determine the types of defects present.

Specimens synthesized in a bulk form or as thin films may contain submicron grains, with grain boundaries having a substantial impact on the overall properties of the material. This occurs in boron-doped diamond thin films studied here. We show that in these specimens doping may affect not only the conductivity type, but also the size of the grains. Boron-doped diamond can be used in device applications in harsh environments. However, the effects of boron doping

as well as the effects of irradiation on the defect properties of diamond grain surfaces are not well understood. We have characterized boron-doped diamond thin films and observed a correlation between the mechanisms of conductivity (bulk vs. grain surface) and the electronic structure of these samples.

In our work, the outlined issues were addressed employing non-destructive surface and bulk defect-sensitive experimental probes – surface photovoltage (SPV) and photoluminescence (PL) spectroscopy, which will be discussed in detail below.

1.1 Titanium Dioxide (TiO₂)

Potential applications of titanium dioxide have driven extensive studies of this material. In particular, TiO₂ in the anatase form is preferred for photocatalytic (PC) applications due to its relatively high activity, availability, nontoxicity, chemical and thermal stability and resistance to corrosion.⁸ PC reactions can start as a result of electron-hole separation induced by incident radiation. Subsequently, separated charge carriers can participate in the decomposition of surface adsorbents. The efficiency of the PC reaction at the surface of a semiconductor material is determined by, among other factors, the electronic bandgap structure. Such factors as charge recombination rate, bandgap energy, presence and spectral locations of gap states are crucial. Anatase TiO₂ (a polymorph studied here) has an indirect bandgap of ~ 3.2 eV⁹ and the charge separation can occur if ultraviolet (UV) light is used. However, in order to utilize a broad solar spectrum, which contains ~ 43% visible light and ~ 5% UV radiation,¹⁰ sensitization of TiO₂ to visible light is desirable. Modification of TiO₂ sub-bandgap electronic structure is one of the accepted approaches to visible light sensitization. Modifications can include doping with different metals or nonmetals, co-doping with metal oxides, self-doping and growth of various nanostructures.⁸ The main goals of all these approaches would be reduction of the bandgap

energy and formation of gap states, capable of visible light absorption. This, in turn, allows PC reaction to be induced in a broader range of wavelengths of incident solar illumination and thus a much greater number of charge carriers to participate in the process. Indeed, experiments show that adequate doping introduces states within the TiO₂ bandgap, which enable absorption of visible light.¹¹ Enhancement of such absorption in turn improves visible light PC performance.¹¹ Native defects (oxygen vacancies and titanium interstitials) also induce energy levels within the bandgap of anatase and play a role in both visible and UV light-activated PC reactions.¹²

We studied electronic structure of anatase TiO₂ thin films modified by adding nanophases of noble metals (Ag or Au) and by blending with zirconia. Addition of noble metals (Ag, Au) or ZrO₂ to the anatase matrix was reported to improve PC activity of these composites due to various reasons explained below. To better understand phenomena behind the improved PC activity of such modified systems detailed analysis of their electronic structure is necessary and, in particular, elucidation of the roles of dopant- and native defect-related states. The influence of the latter can be also addressed via self-doping (e.g., Ti⁺-irradiation). In this work thereby experimental characterization of the electronic structure was performed for both as-grown and Ti⁺-irradiated TiO₂, TiO₂/Ag, TiO₂/Au and TiO₂/ZrO₂ thin films. The films were grown by the sol-gel method, which is commonly used for the synthesis of catalytic materials because of low thermal budget, accurate grain size control, reduced contamination due to the usage of pure materials, etc.¹³

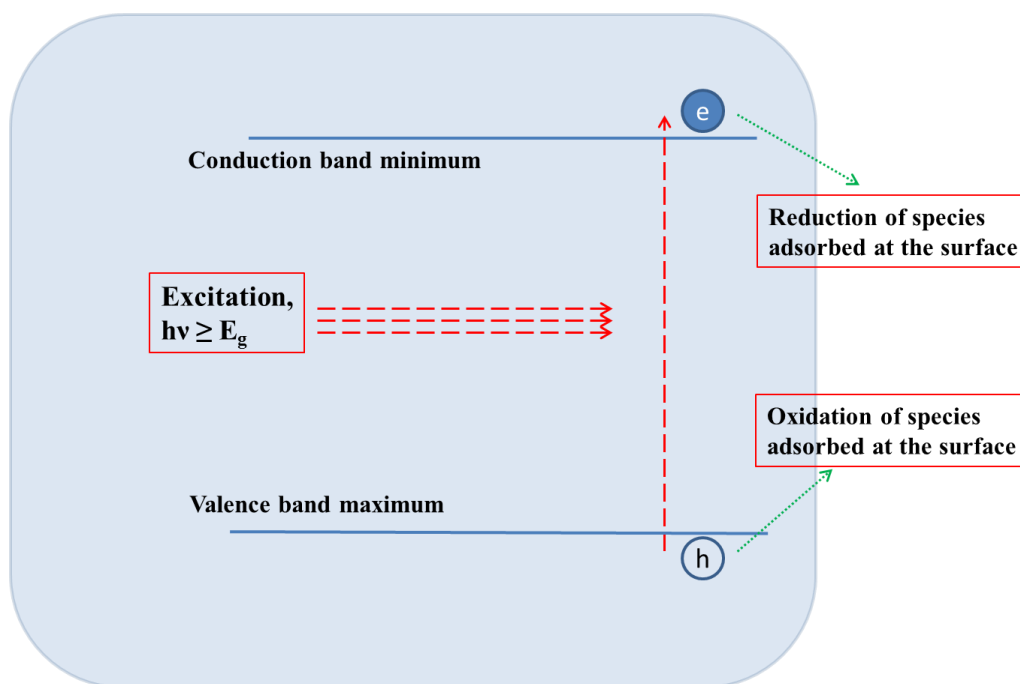


Figure 1. Photocatalysis mechanism

Schematically, the basic mechanism of photocatalysis is shown in Fig. 1. When a photocatalyst, such as TiO_2 , is illuminated with photons of energy greater than its bandgap, the electrons and holes become separated. Part of these optically generated charge carriers quickly recombine while the remaining carriers can take part in photodegradation of adsorbates at the surface of the photocatalyst.⁹ The efficiency of such photodecomposition process depends, among other factors, on the ability of electrons (holes) of the photocatalyst to reduce (oxidize) species absorbed at the surface, e.g. water. As a result of such reduction/oxidation reactions, active radicals such as OH-groups, hydrogen peroxide (H_2O_2) and superoxides (O^{2-} radicals resulting from the reduction of O_2) can be created.⁸ These active radicals can react with organic molecules absorbed at the surface and decompose them down to basic compounds.⁸

In nature, titanium dioxide can form three crystal structures (polymorphs): rutile, anatase and brookite. Rutile and anatase are more thermodynamically stable¹⁴ and are thus the most studied phases, especially the rutile phase. If TiO_2 is synthesized in the laboratory, the structure

of the resulting TiO_2 largely depends on the temperature of calcination - the concluding step of the growth process. The anatase phase is produced at calcination temperatures of at least 400°C while crystallization of rutile requires temperatures of up to 1000°C .¹⁵ Having a tetragonal crystal structure, anatase and rutile belong to different space groups. Anatase is often reported to be more photocatalytically active in some type of reactions.¹² In this work we investigate anatase phase only and therefore hereinafter “ TiO_2 ” or “titanium dioxide” will denote primarily the anatase phase. The phase will be stated explicitly if comparison to rutile TiO_2 is made.

In a TiO_2 crystal, bonding between Ti and O atoms is of a mixed nature - ionic and covalent. Titanium dioxide has each Ti atom surrounded by six O atoms, forming slightly distorted octahedra as the building blocks of the tetragonal lattice (Figure 2).⁹

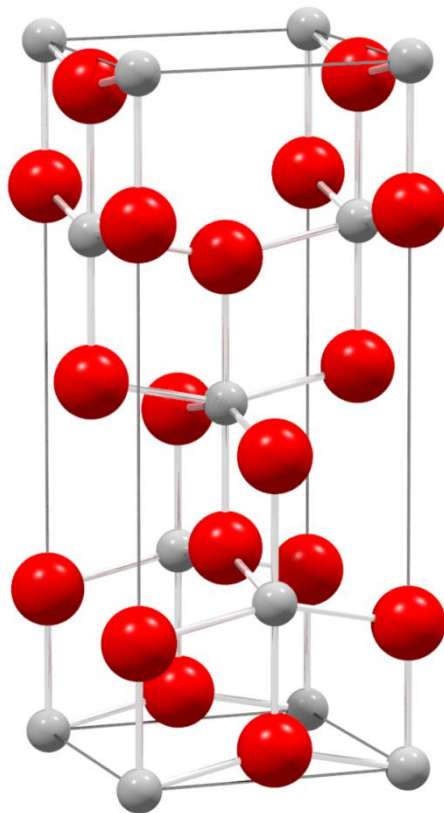


Figure 2. Crystal structure of anatase TiO_2 , gray – Ti; red – O.

The valence band is formed by the $2p$ states of oxygen and the conduction band – by the $3d$ states of titanium. The bandgap is indirect and its value is 3.2 eV.⁹ It is well known that the lattice of both naturally occurring and synthetic TiO_2 is abundant in such native defects as oxygen vacancies (V_o) and/or titanium interstitials (Ti_{int}).¹⁶ These defects can be easily created during growth and post growth treatments.¹² Density functional theory (DFT) calculations show that creation of V_o is more favorable than creation of Ti_{int} .¹⁷ A missing oxygen atom (whose electron configuration is $1s^2 2s^2 2p^4$) in the TiO_2 lattice is the oxygen vacancy with two electrons trapped in it (which previously occupied the $2p$ states), the so called an F -center,⁶ which can thus trap two holes. V_o can also exist in two alternative states – singly ionized, with only one electron in the vacancy (F^+ color center) and doubly-ionized, with no electrons in the vacancy (F^{++} color center).⁶ Additionally, some or all of the electrons left after O removal can reduce neighboring Ti^{4+} ions to Ti^{3+} ions.⁶ It should be noted, that reduction of Ti^{4+} to Ti^{3+} can be caused by the presence of Ti_{int} as well.¹⁶ Therefore, a simple oxygen vacancy could create several types of defects – the F -type color centers and/or the Ti^{3+} ions. These defects introduce electronic levels in the bandgap¹⁷ of TiO_2 . Table 1 presents a synopsis of energy values assigned in literature to oxygen deficiency-related defects, most of which are located in the energy range of ~ 1.9 eV- 2.9 eV above the top of the valence band.

Table 1. Gap states related to TiO₂ reduction and observed in TiO₂ using various experimental methods or theoretical calculations (CBM –Conduction band minimum; VBM – Valence band maximum).

Energy	Origin	Phase
1.9 eV	Oxygen vacancies ¹⁸	Anatase single crystal
	Oxygen vacancies ¹⁸	Anatase nanopowders
2.0 – 2.1 eV	Oxygen vacancies ²⁰	Anatase thin films
	Oxygen vacancies ¹⁹	Rutile thin films
2.2 eV	Ti ³⁺ or Ti ²⁺ states ²¹	Rutile thin films
2.3-2.4 eV	Ti ³⁺ states ¹⁸	Anatase single crystal
	Oxygen vacancies ²²	Anatase nanoparticles
2.5-2.6 eV	Oxygen vacancies ²³	Anatase thin films
	Oxygen vacancies ²²	Anatase nanoparticles
	Oxygen vacancies ²³	Anatase thin films
2.7- 2.8 eV	Oxygen vacancies ²⁴	Anatase nanotube arrays
	Oxygen vacancies ²²	Anatase nanoparticles
	Oxygen vacancies ²²	Anatase nanoparticles
2.9 eV	Oxygen vacancies ²²	Anatase nanoparticles
0.5 eV below the CBM	Ti ³⁺ states ²⁵	Anatase thin films
0.8 eV below the CBM	Singly ionized oxygen vacancies ²⁶	Anatase nanopowders
	Titanium interstitial ¹⁶	DFT anatase
1 eV below the CBM 2 eV above the VBM.	Ti ³⁺ states ²⁷	DFT anatase
1.5 eV below the CBM	Oxygen vacancies ¹²	DFT

In photoluminescence experiments at low temperatures an emission at ~ 2.3-2.4 eV is commonly detected in TiO₂. It is usually attributed to recombination of self-trapped excitons (STE). Formation of STE is an intrinsic feature of the anatase TiO₂ and is not observed in the rutile polymorph. This emission is observed in both single crystals^{28,18} and nanostructures.^{18,29,30}

STE are likely formed in anatase TiO₂ upon superbandgap excitation due to strong exciton-phonon interaction.³¹ In Ref. 32 it is suggested that STE are more readily formed under superbandgap excitation of the sample while if subbandgap light is used, the observed PL emission is defect-related. With the increase in temperature, STE emission in TiO₂ was reported to shift to higher energies and quench significantly at room temperature.³¹ In BaTiO₃ low temperature STE emission was observed at ~ 2.3 eV as well and this emission quenched at 150 K.³³ However, the PL band at ~ 2.3-2.4 eV was still observed for some TiO₂ samples at room temperature. For example, in anatase nanostructures²² the room temperature PL band at ~ 2.3 - 2.4 eV was attributed to oxygen vacancies. In the TiO₂ samples studied here we observed the ~ 2.3-2.4 eV PL band at low temperature in all the samples whereas at room temperature – only for some samples. Interpretation of this observation will be given Chapter 3.

In view of the PC applications, presence of gap levels affects light absorption and charge carrier dynamics in TiO₂. As seen in Table 1, defect states related to oxygen deficiency or Ti excess all lie in the visible spectral range. The role of these defect states in photocatalysis is not completely understood in pristine TiO₂ and is frequently overlooked in modified TiO₂. In visible light-activated PC reactions, native defects facilitate absorption of visible light. On the other hand, in UV-activated PC reactions native defects could hinder recombination of generated charge carriers³⁴ and enable reactions of TiO₂ surface with water,³⁵ although some reports suggest that native defects may act as recombination centers and their presence is detrimental.²⁷

As mentioned above, we studied two types of modified anatase: TiO₂ thin films with added nanophases of noble metals (Ag or Au) and thin films blended with zirconia (ZrO₂). Both UV and visible PC reactions were tested on noble metal-doped TiO₂ while TiO₂/ZrO₂ PC was studied mostly with UV illumination. In both cases the PC activity was improved. It is

suggested that addition of zirconia could increase the surface area of the compound and/or induce defect-related gap states.³⁶⁻³⁹

Noble metals are thought to facilitate charge transfer at the semiconductor-metal interface,⁴⁰ hinder recombination process,^{41,42} as well as enhance absorption of light due to both the surface plasmon resonance (Ag^{43,44}, Au⁴⁵) and presence of Ag- or Au-induced gap states (TiO₂/Ag^{46,47} and TiO₂/Au⁴⁸).

To elucidate the role of electronic states related to extrinsic and intrinsic defects we performed comparative studies of the electronic structure of TiO₂, TiO₂/Ag, TiO₂/Au and TiO₂/ZrO₂ thin films and discuss possible implications of such modifications on PC applications of these systems.

Self-doping of TiO₂ nanoparticles was reported to also improve their visible light PC activity.⁴⁹ Thin films of TiO₂ are good candidates for applications in harsh environments and therefore the response of TiO₂ or its composites to irradiation is of interest. For our samples, a low energy (140 KeV) Ti⁺ irradiation was used to study the effects of self-doping on the content of native defects, important for applications in harsh environments. As described in Ref. 50, either electronic or nuclear stopping in the material may prevail depending on the energy of the incident ion beam. 140 KeV is sufficient for electronic stopping mechanism to dominate.⁵⁰ In general, a variety of phenomena may result from the electronic or nuclear ion stopping in matter: translational motion and/or ionization of the target atoms, excitation of electrons into the conduction band, creation of defects or their complexes.⁵⁰ Some point defects may disappear as a result of ion implantation, for example vacancy-interstitial complexes.⁵⁰ Both beam energy and the electronic structure of the target material prior to implantation affect the outcome of the implantation. In our work studies of electronic structure of TiO₂, TiO₂/Ag, TiO₂/Au and TiO₂/ZrO₂ were performed after Ti⁺ self-doping (Ti⁺ irradiation).

1.2 Zinc Oxide (ZnO)

ZnO has a broad spectrum of existing and potential applications. ZnO is a II-VI semiconductor, with a direct wide bandgap of ~ 3.3 eV.⁵ Its unique combination of properties, such as UV-bandgap, high excitonic binding energy (~ 60 meV), thermal stability, make its implementation possible in blue/UV optoelectronic devices, gas sensors, transparent conducting oxides, etc.⁵

The valence band of ZnO is formed by the O $2p$ states and the conduction band - by the $4s$ states of Zn. ZnO crystallizes mainly in the hexagonal wurtzite structure.⁵ The bonding is a mixture of ionic and covalent types. In the lattice, each zinc ion is surrounded by four oxygen ions.

Native defects and/or impurities impact many properties of ZnO. Undoped ZnO is an n -type semiconductor⁵ and the origin of such intrinsic conductivity is still unclear. Although it was suggested that hydrogen can act as a shallow donor⁵¹ recent studies demonstrated that this can only partially explain the persistent n -type behavior of as-grown ZnO.⁵² Native defects in ZnO can be created during growth in Zn-rich conditions at concentrations as high as ~ 1 %.⁵² Calculations show that oxygen vacancies should be formed at significantly greater concentrations than those of zinc interstitials.⁵² Oxygen deficiency was also suggested as a possible source of shallow donor-type states.⁵ Although neutral V_o introduce deep donor levels into the ZnO bandgap, it was proposed that the excited state of the V_o (ionized V_o) is a shallow state.⁵² A neutral oxygen vacancy introduces a deep donor level at ~ 2.4 eV with respect to valence band maximum, as established in both experimental^{53,54} and theoretical studies.⁵ In addition to native defects, residual impurities such as Al, H, Ga are found in synthetic ZnO.⁵⁵

For many prospective applications it is desirable to grow *p*-type ZnO thin films. Low defect/impurity content together with minimal effects of the film/substrate interface are essential for electronic device applications and robust *p*-type doping, yet many stumbling blocks remain en route to the realization of reliable and high-performance *p*-type ZnO. Since the source of the intrinsic *n*-type conductivity in undoped ZnO is still in question, it is also not clear what dopant can readily compensate the existing shallow donors and ensure adequate abundance of shallow acceptors for a *p*-type ZnO.

Thus a significant research effort is focused on the growth of ZnO thin films with low concentration of point and extended defects as a precursor for successful shallow acceptor doping. Currently, various growth methods are employed to obtain both heteroepitaxial (the substrate and film are two different materials) and homoepitaxial (the materials of the substrate and the film are the same) ZnO. Homoepitaxial growth was performed using chemical vapor deposition,⁵⁴ radio frequency sputtering,⁵⁵ pulsed laser deposition,⁵⁶ liquid phase epitaxy,⁵⁷ metal organic vapor phase epitaxy.⁵⁸ The substrate/film interface is one of the sources of defects in ZnO thin films. This is a major problem in heteroepitaxial layers due to substrate/film lattice mismatch and the difference in the coefficients of thermal expansion, leading to the presence of residual carrier concentration.⁵⁹ Currently heteroepitaxial growth of ZnO thin films is performed mostly on sapphire substrates. On the other hand, homoepitaxial films represent an advantage due to the absence of mismatch in lattice characteristics between the substrate and the film along with identical thermal properties of the two.⁶⁰ Polarity of the ZnO substrate seems to influence the quality of ZnO thin films as well⁵⁵. Defects can cause lattice strains and affect electrical and optical properties of the films. Matsui *et al.* studied strained homoepitaxial *a*-plane ZnO layers and concluded that the strain was caused by basal stacking faults in the layers.⁵⁶ Other challenges and open questions still exist in attaining a desired quality of the ZnO/ZnO

homoepitaxy, such as a choice of suitable substrates,⁶¹ finding adequate substrate treatment methods prior to film growth,^{59,62,63} effects of substrate polarity⁵⁴ and diffusion (of zinc) at the film/substrate interface.⁶⁴

Nevertheless, homoepitaxy seems to be preferable to heteroepitaxy for a growth of high-quality ZnO films. High-quality homoepitaxial ZnO films were to date obtained using synthesis methods requiring growth temperatures in excess of 400°C.^{54, 62, 65-68}

In our work we studied high-quality ZnO layers grown on O-face ZnO substrates by the so called ALD technique. The samples were grown at the University of Texas at San Antonio (Prof. Chabanov's group). These specimens combine the advantages of the ALD technique (uniform layer-by-layer growth, precision, low deposition temperatures, repeatability, simple doping protocols) and homoepitaxy (no substrate/film lattice mismatch). The samples were grown at three different relatively low temperatures: 120°C, 150°C, and 200°C. To the best of our knowledge, ALD ZnO on ZnO growth has not been implemented before, since to date ALD has been employed to grow primarily hetero-epitaxial ZnO, mainly on Si substrates. ALD-grown ZnO has been studied on the subject of device applications.^{69,70} For example, optoelectronic properties of ALD-grown ZnO films were investigated as a function of substrate temperature,^{71,72} purging and pulsing times.⁷³

In order to establish whether ALD is suitable for high-quality ZnO homoepitaxy we need to: a) determine the overall quality of the ZnO layers; b) identify the nature of dominant defects; c) study the effects of growth conditions on defect concentration. In this work optoelectronic properties of the ZnO thin films grown at three different temperatures were probed using room temperature and low temperature PL spectroscopy and SPV spectroscopy. We demonstrated that the quality of these samples is better than or comparable to the quality of homoepitaxial ZnO thin films grown by other methods referenced above.

1.3 Diamond

In many systems grain boundaries play a pivotal role, where grain sizes, their defect content and other interface conditions determine overall figures of merits such as conductivity for example. In turn, grain morphology can be affected by the doping levels, growth parameters and post-growth treatments. One of such thin film materials studied by us is boron-doped diamond.

Diamond exhibits outstanding physical and electronic properties, such as record-setting mechanical hardness, deep UV band gap (~5.5 eV), high thermal conductivity, chemical stability, biocompatibility and radiation-hardness, etc.^{74,75} Following rapid advancements of growth techniques in recent years it became possible to synthesize diamond thin films using chemical vapor deposition (CVD), thus avoiding high pressures/high temperatures.⁷⁶ Such advantage in combination with the outstanding physical properties of diamond make diamond thin films (both homo- and heteroepitaxial) quite attractive for applications in optoelectronic devices, mechanical tools and biomedical technology. The exceptional radiation-hardness, in particular, makes applications of diamond thin films possible in, for example, devices operating in harsh radiation environments such as radiation/particle detectors, dosimeters, nuclear radiation batteries, outer space equipment, nuclear micro-battery and other devices operating in intense radiation environments.⁷⁵ Therefore, explication of the microscopic response of diamond to radiation – formation and evolution of bulk and surface defects, changes in the electronic characteristics, chemistry of dopants – is necessary for reliable control and reproducibility in diamond-based applications. Many of these phenomena are still poorly understood and require detailed studies. In this regard we addressed the questions of: a) the primary mechanism of conductivity in boron-doped CVD diamond thin films; b) the effects of various levels of B doping on films'

conductivity and microstructure and c) the effects of gamma irradiation on the conductive properties of CVD-grown diamond thin films.

Diamond is one of the most researched carbon allotropes (others being graphite, amorphous carbon, carbon nanotubes, graphene etc.). The carbon atoms covalently bonded via the sp^3 hybridization are arranged to form a diamond lattice. Graphite, on the other hand, is formed through the sp^2 hybridization of carbon atoms. Usually surfaces of diamond nanocrystals, grains included, contain graphite forming during growth.⁷⁵ In the literature the grain surfaces in a polycrystalline CVD diamond are presumed to be rather rich in the graphitic sp^2 bonded carbon configuration. The presence of both types of bonding in the synthesized films influences their electronic properties, especially in conjunction with the presence of dopant. Doping is necessary to utilize diamond's semiconducting properties, since pure diamond is insulating at normal conditions due to its deep UV bandgap. Boron is usually employed as one of the dopants rendering diamond a *p*-type semiconductor.⁷⁵

Growth and post-growth treatments are commonly used to tailor microstructure as well as grain size and morphology. Until recently, control of diamond microstructure was geared towards influencing the crystal orientation (so-called texturing) but not, in a significant way, the crystallite size. A major advance in the growth protocol was achieved via modification of the gas phase chemistry such that the crystallite size spanned from micron to nanometer, a factor of a million in volume. The size can be controlled continuously and reproducibly over this range by changing the gas-phase chemistry of the plasma-enhanced chemical vapor deposition process, i.e, using the noble gas argon instead of the H_2 gas feedstock.⁷⁷ It not only produced smaller crystallites of nanometer grain size, but theory predicted that there is an almost a 10% increase in grain boundary concentration. Variations in grain size in turn could influence other properties of

the material. Establishing such relationship was one of the objectives of the current work with diamond thin films.

Recently a series of comprehensive investigations was reported on the effects of boron doping and gamma irradiation on the properties of diamond thin films grown by microwave plasma-assisted chemical vapor deposition (MPACVD).^{74,78} In particular, it was established that with an increase in boron concentration the abundance of conductive clusters has noticeably increased, especially in the vicinity of grain boundaries rich in sp^2 -hybridized carbon (sp^2C). It was also demonstrated that gamma irradiation transformed quasi-metallic films with elevated B content into semiconducting via hydrogen-assisted passivation of boron acceptors. In short, whereas B doping may lead to a semiconductor-metal transition, gamma irradiation is capable of reversing the transition bringing about an additional way to engineer the electronic properties. Here we present a confirmation of the hypothesis of the semiconductor-metal transition with the increased B concentration and the subsequent reversal to a semiconducting behavior after gamma irradiation. Therefore, in our work on CVD diamond thin films, employing surface and bulk defect-sensitive experimental techniques, we were able to answer questions regarding the dominant mechanisms of conductivity (bulk vs. grain surface), effects of gamma irradiation as well as the relationship between the variation of boron concentration and grain size. To the best of our knowledge, the current studies represent pioneering SPV spectroscopy studies of CVD diamond thin films (undoped or doped). Luminescence studies of various diamond systems (bulk and thin films) have been commonly reported, however, they lack a consensus even on the most common emission signatures/features, let alone when combined with B doped diamond films in conjunction with irradiation. Moreover, we report on the evidence of sp^2C clusters, with minor impact from B, being a primary contributor to the surface-state recombinations in the studied diamond specimens.

Chapter 2

2. Experimental

Adequate experimental probes, sensitive to surface and interface defect states, are necessary to observe the effects of metal oxides and/or Au, Ag nanoparticles on the electronic structure of TiO₂ films, the influence of boron doping on the behavior of grain boundaries in diamond thin films, as well as the correlation between the growth parameters and the thin film quality in the ALD grown homoepitaxial ZnO. We performed such analysis of these different thin films employing SPV and PL spectroscopies, both of which provide information primarily on the states localized within the bandgap along with other useful information about the electronic structures of the studied specimens. Importantly, the two techniques are rather complementary having different sensitivities to the bulk vs. surface states, with PL being more of a bulk-specific tool, while SPV – a surface-sensitive one.

2.1 Surface Photovoltage Spectroscopy

SPV spectroscopy represents an effective way to experimentally characterize optoelectronic properties of the surface of a material. Because of space limitations we will discuss herein only the most fundamental concepts of SPV.

Let us concentrate on the processes occurring at a boundary between a solid and vacuum (a free surface) or between two solids (an interface). A crystalline solid is characterized by a periodic arrangement of atoms forming a crystal lattice. Atoms form unit cells specific for each lattice structure; these closely spaced atoms create a periodic potential. However, if the periodicity of the lattice is violated, in the vicinity of localized defects or at the crystal boundary

(surface or interface), the unit cells are no longer equivalent to the bulk ones, with entailing change in potential.⁸⁰ Because of the termination of the periodic lattice structure dangling bonds are formed at the surface, interface. Surface reconstruction and/or termination can be also accompanied by surface adsorption of foreign species. These phenomena result in the formation of localized surface states. For semiconducting and insulator crystals these states are located mostly within the energy bandgap.

In semiconductors, as a consequence, the surface states may start trapping charge carriers coming within the vicinity of the surface.⁸⁰ As a result, the surface may accumulate excess charge and give rise to an electric field build-up at the surface, which in turn would repel other carriers. This could create a difference in the density of charge carriers between the bulk and the surface leading to the formation of a charged near-surface layer, known as the space charge region (SCR), which is significantly depleted in mobile majority charge carriers. The concentration of these carriers in the SCR is smaller than its value in the bulk (equilibrium value), but still larger than that of the minority carrier concentration.⁸⁰ Consequently, the energy bands bend in the SCR often creating a surface potential barrier (a.k.a. surface potential) characterized by its value at the surface V_s .⁸⁰ The shape of the surface barrier has to satisfy the charge neutrality condition, i.e. that the sum of the net charge in surface states (Q_{ss}) and the net charge in the SCR (Q_{sc}) should result in zero:

$$Q_{ss} + Q_{sc} = 0 \quad (1)$$

By definition, the surface photovoltage effect refers to the change in the surface potential induced by a flux of photons.

If the photon energy exceeds the value of the bandgap, illumination may have valence electrons excited across the bandgap leading to generation of electron-hole pairs (super-bandgap illumination). On the other hand, if the photon energy is smaller than the value of the bandgap (sub-bandgap illumination) then illumination can either liberate a surface-trapped charge carrier into the bulk or “bump” a free near-surface carrier into a surface trap state. The outcome of both the super- and sub-bandgap illumination is a change in the net charge at the surface, and thus in the surface potential. The illumination-induced change in V_s depends mainly on the electronic structure of and within the bandgap. Condition (1) is still satisfied, and although both Q_{ss} and Q_{sc} may change as a result of illumination, their sum remains zero.

In an SPV spectroscopy experiment, the surface potential (V_s) is monitored as a function of a variable wavelength of an incident monochromatic light. A contactless method to measure V_s , going back to Lord Kelvin, is based on measuring the difference between the work functions ϕ_s of two materials in proximity of each other, the surfaces of which are equivalent to plates of a parallel-plate capacitor. The reason for monitoring the work function difference is that the surface potential and the work function of a semiconductor are dependent so that if V_s changes, the corresponding change in ϕ_s is the same. In practice, while the surface under study represents one side of a capacitor, the other side is produced by a reference metallic surface with the work function that does not change with illumination (the so called Kelvin probe). When the two sides of capacitance are connected through a zero DC bias, the resulting charge flow will lead to an equilibration of the two Fermi levels. Charge flow produces an electric field and a potential difference between the two sides equal to the difference in the work functions of the two surfaces, known as the contact potential difference (CPD). Thereby, the CPD is equal in magnitude to the change in surface potential (SPV signal).⁸⁰

It is not trivial to measure the value of the CPD. It could be accomplished by the null method, proposed by Kelvin, as follows. If the plates are connected through a nonzero DC bias equal to the difference between the work functions, then there is no net flow of charge. Under these conditions, if the capacitance is changed via the change in the distance between the plates the charge should flow. If the Kelvin probe is vibrating, it will produce an AC current (unless the capacitor is discharged). So, the way to obtain the value of the CPD is to apply such external bias to the plates, that there will be no current in the circuit. The value of such required bias is the magnitude of the difference in the work functions of the two surfaces. To detect a change in the surface potential, a periodically vibrating Kelvin probe is placed close to the surface of the sample while the value of the bias needed to discharge the capacitor (to nullify the AC current) is determined using dedicated electronics. This bias is equal in magnitude to V_s , and its magnitude provides the value of the work function difference and thus the CPD.

Analysis of the spectra allows one to obtain a number of important parameters. One of them is the value of the bandgap energy. When the energy of incident photons reaches the value of the bandgap energy, the absorption of photons significantly increases through generation of electron-hole pairs.⁸⁰ This leads to an increase in the value of the surface potential and thus in the value of the CPD which depends on the total charge of the SCR, Q_{sc} .⁸⁰ So, in the SPV spectrum, the onset of the greatest change in the CPD signal would correspond to the approximate value of the bandgap.⁸⁰ The more accurate way to determine the value of the bandgap from the spectrum is to look at the extremum of the derivative of the SPV spectrum.⁸⁰ The error in the determination of the bandgap value can nevertheless be as large as 0.1 eV.⁸⁰ Importantly, from the direction of inflection (up or down) of the CPD signal around the band gap energy one can deduce the type of conductivity of the studied semiconductor – *n*-type vs. *p*-type.

Similar phenomena happen during a sub-bandgap illumination albeit within the bandgap. When photons have enough energy to induce trap-to-band or band-to-trap transitions, the value of V_s should change accordingly, and a “knee” in the SPV spectrum will be observed, i.e. the change in the slope of the monitored CPD. Specifically, if there exists a state with the energy E_t below the bottom of the conduction band and the incident light photons have energy $E > E_t$, electrons can be excited from that state to the conduction band. Depopulation of this state will reduce the negative charge at the surface, which corresponds to a change in the CPD.⁸⁰ Consequently, one would see a change in the slope in the SPV spectrum at the threshold energy corresponding to the approximate position of the trap state relative to the conduction band.⁸⁰ Similarly, if the energy separation between the localized surface state and the top of the valence band is E_t' , photons with energy $E \geq E_t'$ can excite electrons from the valence band into this surface state. In this case the surface gains electrons becoming more negatively charged and producing a change in the CPD opposite to that described above in this paragraph. As a result it is possible not only to determine the value of the energy separating the state from the band edge but also to distinguish trap-to-band from band-to-trap transitions. Moreover, the relative magnitude of the slope change can provide a qualitative estimate of the intensity of this transition and thus the abundance of the corresponding surface state.

The SPV signal obviously depends on the population or depopulation of the surface states. Thus, careful preparation of the surface is necessary for systematic and repeatable experimental outcomes. Such conditions can be achieved in the following way. First, the surface is exposed to an intense illumination in a broad spectral range (IR through UV) in order to achieve dynamic equilibrium of free charge generation and recombination in the vicinity of the surface. During this, the CPD is monitored by the Kelvin probe as a function of time to determine the saturation phase. Then the illumination is turned off and the CPD is allowed to

stabilize in complete darkness to ensure “relaxation” of the surface states. Times necessary to reach equilibrium in light and in the dark depend on the electronic structure within the bandgap, concentration of charge carriers, cross-sections of contributing transitions as well as the competition between thermal and optical excitation.

It is worthwhile to mention that ambient conditions may affect the outcome of the experiment. There are no pressure limitations for the SPV measurements and it can generally be run at atmospheric pressure. However, in many cases it is preferable to probe contamination-free surfaces. In this case an ultra-high vacuum (UHV) environment is highly advantageous.

In our experimental SPV setup all measurements are done inside a vacuum chamber (pressure $\sim 10^{-8}$ Torr). During the experiments, to minimize mechanical vibrations, a mechanical pump is turned off and the vacuum is maintained by the ion pump only. The vibrating Besocke Kelvin Probe S is a circular mesh electrode ~ 2 mm in diameter. It is gold-coated to ensure constancy of the work function over the lifetime of the probe.⁸⁰ The position of the probe is fixed inside the experimental chamber whereas the position of the sample is adjusted using the XYZ-manipulator to be ~ 1 mm below the probe. An ex-vacuo 250W QTH (Quarz Halogen Tungsten) lamp is used as a source of illumination with a continuous spectrum from IR to UV. The light is fed via a pair of fused silica lenses into an Oriel Cornerstone grating monochromator with two diffraction gratings operating in the 180-750 nm and 450-2000 nm spectral ranges. Thus, the combined SPV spectral energy range is ~ 1.1 eV – 6.5 eV. To eliminate higher diffraction orders in the spectra a filter wheel with different bandpass filters is placed between the light source and the monochromator. In some experiments the illumination is also chopped by a mechanical light chopper. A monochromator is coupled via an F-number matcher to an optical fiber bundle, which is fed through a vacuum feedthrough into the immediate vicinity of the Kelvin probe inside the vacuum chamber. The time constant and

stepping of the monochromator are controlled by a LabView program. As a result, light of variable frequency is incident onto the surface of the sample. The SPV spectroscopy experiments are performed in complete darkness. Prior to running the SPV spectra, the light-dark saturation is achieved to equilibrate the surface, as described above, with the CPD monitored as a function of time.

2.2 Photoluminescence Spectroscopy

The second defect-sensitive technique used in our studies is PL spectroscopy. The information depth of PL is of the order of the absorption depth of the laser beam, which is usually significantly greater than the SPV information depth, limited by the diffusion length of the charge carriers. Therefore one can say that the PL characterization is more bulk-specific compared to SPV. Since bulk intrinsic and extrinsic defects give rise to electronic states within the bandgap, their energies can be identified by measuring the energies of photons emitted as a result of recombination involving the defects energy levels. The principle of PL spectroscopy is illustrated by the diagram shown in Figure 3.

As a result of super-bandgap illumination, the valence band electrons acquire enough energy to jump into the conduction band leaving mobile holes in the valence band. The electrons then thermalize quickly via exchange with the lattice to the bottom of the conduction band. Subsequent recombination of the electron-hole pairs across the bandgap may lead (in the case of direct bandgap materials) to an emission of photons with the energy equal to the bandgap value. However, recombination may occur not necessarily involving two free charge carriers of an opposite sign.

An electron from the bottom of the conduction band or a hole from the top of the valence band may be trapped by a nearby defect state in the gap followed by an emission of the photon of corresponding sub-bandgap energy. There are other, more complex, recombination mechanisms involving defect states.

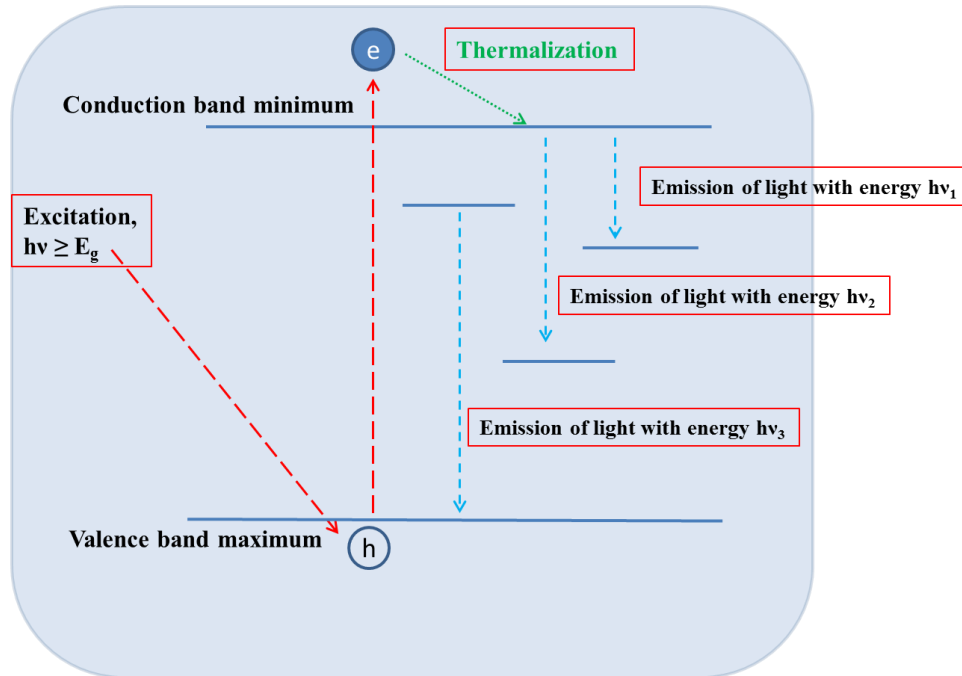


Figure 3. Principle of photoluminescence

In addition to providing information about the bandgap energy and the energetics of the defect states, analysis of PL spectra can yield information regarding the overall quality of the thin films. Usually an intense and narrow bandgap peak points to a crystal lattice of good quality. Looking at the intensity of the defect luminescent features, one can qualitatively determine their relative concentration.

Obviously, the possibility of nonradiative transitions has to be taken into account. They do not contribute to the emitted light and thus are not observed in the spectra. A possible

mechanism for the nonradiative energy transfer could be, e.g., an exchange with lattice vibrations (phonons). Nonradiative transitions are more common in indirect bandgap materials.

PL does not have the ability to distinguish between transition from or to the gap states, as opposed to the SPV spectroscopy. Usually, the unambiguous assignment of the defect state positions in the gap has to be performed using complementary techniques, and SPV is an outstanding candidate in this respect. Moreover, the PL signal is more bulk-related, although it contains radiative contributions from the surface as well. On the other hand, SPV spectra are collected from the defects in the near-surface vicinity. Thus combination of SPV and PL can provide numerous advantages.

Under appropriate circumstances (relatively low temperatures, high quality of a crystalline lattice, etc.) electrons and holes may be coupled by a modified Coulomb interaction to form hydrogen-like complexes, called excitons. The binding energy of an exciton depends on the composition and structure of the host material, as well as possible size effects, such as confinement in a nanoscale crystal. For example, in ZnO the energy of exciton dissociation is ~ 60 meV, i.e. greater than the thermal energy at room temperature (~ 25 meV), which implies the existence of excitons in ZnO even at and above the room temperature.

If the motion of an exciton through the lattice is not significantly obstructed, it is referred to as a free exciton (FEx). Recombination of an excitonic electron-hole pair results in the emission of a photon with an energy somewhat smaller than the bandgap energy, the so called FEx recombination.

Defects present in the system distort the lattice thus creating potential wells. At low temperatures, these wells can trap excitons, mostly via modified dipole interaction. Such captured excitons are then referred to as bound excitons (BEx). The BEx recombinations results in the emission of photons of smaller energy compared to FEx emission.⁸¹ Since excitons are

hydrogen-like complexes, they possess discrete energy levels, from the ground level up. On the other hand, the binding defects themselves have systems of discrete electronic levels. Plus, the lattice distortion wells create their own quantum levels for the trapped excitons. Thus, sometimes it is not easy to unambiguously interpret the PL spectra at low temperatures. Nevertheless, low temperature PL measurements reveal substantial additional information on the properties of the material, especially when spectral evolution vs. temperature can be obtained.⁸²

For example, from the analysis of the T -dependence for the PL peak intensity one can extract the activation energy (the energy needed to separate the exciton from the binding defect).

Theoretically, the temperature dependence of the BEx peak intensity is described by the following expression:⁸³

$$I(T) = \frac{I_0}{1 + Ae^{-E_a/kT}} \quad (2)$$

Where I_0 is the peak intensity at 0 K, A – a fitting constant (see below), E_a – the activation energy, k – Boltzmann constant, T – the absolute temperature. This formula can be derived from the following considerations. We will assume that a predominant mechanism of thermal excitation of BEx is its complete liberation from the potential well rendering it free. Within this approximation, at certain temperature, the sum of the number of BEx in the ground state and FEx will give the total number of excitons:

$$N_F(T) + N_B(T) = N_T(T) \quad (3)$$

Setting the BEx energy to be E_B and the FEx energy – E_F , the number of excitons with these energies at temperature T will be approximately described by Boltzmann statistics:

$$N_F(T) = N_T \alpha_F \exp(-E_F/kT)/Z \quad (4)$$

$$N_B(T) = N_T \alpha_B \exp(-E_B/kT)/Z \quad (5)$$

Here α_F and α_B are the degeneracies of FEx and BEx in the states with energies E_F and E_B respectively. If the total number of excitons is conserved, then the value of $N_T(T)$ is a constant, since at 0 K all excitons are bound: $N_T(T) = N_T(0)$. Incidentally, for ZnO this holds true since FEx survive even at room temperature.

Using equations (3), (4) and (5), the following relation can be obtained:

$$\frac{N_B(T)}{N_T(T)} = \frac{1}{1 + Ae^{-E_a/kT}} \quad (6)$$

Here $A = \alpha_B/\alpha_F$ and $E_a = E_F - E_B$, the activation energy necessary to free BEx. Now, since the intensity of the BEx luminescence is proportional to the number of bound excitons at certain temperature, we can rewrite the above formula in the following way:

$$\frac{I(T)}{I_0} = \frac{1}{1 + Ae^{-E_a/kT}} \quad (7)$$

Fitting of experimental data with the formula above allows one to obtain the value of the activation energy, which oftentimes provides key information about the nature of the recombination. Additional information can be obtained from the thermal evolution of the position and broadening of BEx peaks.⁸⁴

A typical setup for the PL experiment would include an excitation source such as a laser, optical elements to guide the laser beam to the sample and then to collect the emitted luminescence into the spectrometer.

In our PL setup we use a continuous wave dual beam HeCd Kimmon laser (model IK5452R-E) operating at 325 nm or 442 nm. The laser beam is directed onto the sample, mounted on the sample holder designed for the Janis CCS-150 closed cycle helium gas cryostat. Helium gas is cooled using the water cooled compressor. Prior to cooling, the cryostat should be evacuated using a mechanical vacuum pump to pressures below 10 mTorr. The temperature of the sample

can be varied in the 6 - 325 K range. The monochromator used in our setup is SPEX 1401 with a spectral resolution of 0.18 cm^{-1} , an optical path of ~ 4 meters and an F-number of 7.8. The monochromator has two gratings, rotation of which can be controlled by a stepper motor. At the exit slit of the spectrometer a photomultiplier tube (PMT) PR C31034 detector collects the signal, converting it into a current output. A Stanford Research lock-in amplifier is connected to the PMT for background noise reduction. The reference frequency for the lock-in amplifier is provided by the external chopper which chops the laser beam at a fixed frequency. Lock-in amplifier converts the current signal from the PMT into the DC voltage, which is then supplied into a PC through the GPIB National Instruments card.

2.3 Auger Electron Spectroscopy

Auger Electron Spectroscopy (AES) is a technique used to determine the chemical composition of the material surfaces. Low probing depth of AES (several nanometers) makes this technique suitable specifically for surface characterization.

It is often used for the thin film studies since conventional energy dispersive X-ray spectroscopy analysis usually shows a significant contribution from the substrate in the spectrum and precise surface composition is difficult to determine (especially at low atomic concentrations). In our work AES was used to determine surface composition of TiO_2 and TiO_2 -based thin films (TiO_2/Ag , TiO_2/Au , and $\text{TiO}_2/\text{ZrO}_2$).

In AES the chemical composition is determined via analysis of the energy spectrum of the Auger electrons. These electrons (in addition to background of secondary and back-scattered electrons) are emitted as a result of interaction of the incident electron beam with the sample material. Figure 4 shows the schematics of the Auger process.

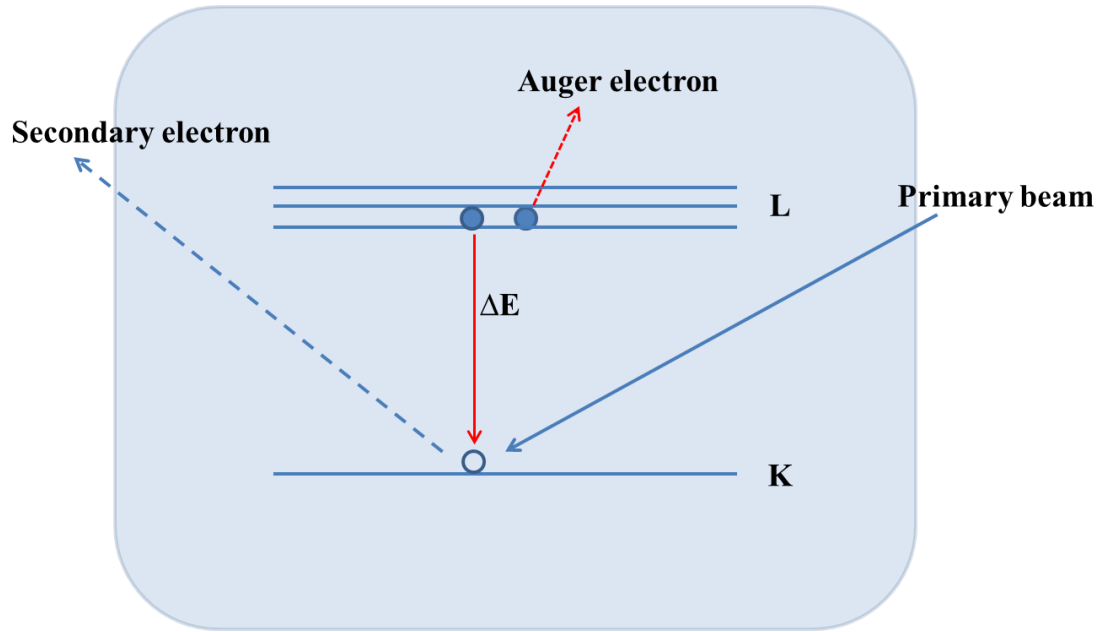


Figure 4. Basic principle of AES spectroscopy

An incident electron ejects an electron from the core level of an atom. Another electron from the outer level fills the core level vacant state. As a result of this “vertical” transition energy ΔE is released. This energy ΔE can be either emitted as an X-ray photon (radiative channel) or transferred to an electron which is subsequently ejected (non-radiative channel). This electron is called an Auger electron. The probability of the Auger process is higher than that for the emission of an X-ray.

In the AES experiment, the kinetic energy of the Auger electrons is measured. The Auger spectrum is unique for each element and therefore chemical elements present on the surface can be determined based on the energies of the observed AES peaks. Since the Auger peaks are usually superimposed on the background of secondary and backscattered electrons, it is not easy to determine their spectral locations in the number of electrons vs. energy dependence, $N(E)$. Conventionally, the data is collected in the differential mode, i.e., $dN(E)/dE$ as a function of energy.

Quantitative analysis of the composition can be performed as follows. The relative abundance of a certain element X is determined by Equation 8.

$$X = \frac{\left(\frac{I_x}{S_x}\right)}{\sum_{i=1}^N \left(\frac{I_i}{S_i}\right)} \quad (8)$$

I_x – value of the Auger signal for the element X .

S_x - relative sensitivity factor of the element X .

N - number of detected elements at the surface.

The relative sensitivity factors for all elements are determined with respect to the reference standard (usually an Ag peak) for a specific incident electron beam energy. These values are tabulated and for our analysis the values from Ref. 85 were used. It should be noted that the errors in the quantitative analysis of the AES spectra using Eq. 8 may originate from: the inaccuracies of determining the amplitude of the Auger signals, misshaped or shifted peaks, background contributions.

The AES experiments were performed in an ultra-high vacuum chamber at the pressure of $\sim 2.5 \times 10^{-7}$ Torr. An LK Technologies electron gun produced an incident 3 KeV electron beam which excited the Auger signal. LK Technologies cylindrical mirror analyzer (CMA) was used to detect the Auger electrons.

For accurate characterization of the surface composition, contamination should be minimized. Exposure of surfaces to air leads to chemisorption or physisorption of such ubiquitous elements as carbon, sulfur, chlorine, etc. If the contaminants coverage is high the true sample composition cannot be accurately determined by AES.

Prior to the AES analysis the surface of the samples was cleaned using remote argon plasma treatment. In our laboratory, plasma is obtained in a high vacuum chamber. Direct plasma is generated inside a Pyrex glass tube via inductively coupled RF power. The direct plasma is pulled towards the sample (i.e. remote plasma) by means of applying pressure differential and electric field to an electrode in the chamber. Details of this custom-built setup are described elsewhere.⁸⁶

Chapter 3

3. Optical studies of electronic band structure in sol-gel anatase TiO₂ modified by Ag, Au, ZrO₂, and Ti⁺-irradiation

3.1 Thin film growth

TiO₂ thin films were synthesized using tetraisopropoxide Ti(OC₃H₇)₄, acetylacetone (AcAc) and ethyl alcohol. After mixing 2ml of ethyl alcohol with 0.25 ml of AcAc, 0.84ml of Ti(OC₃H₇)₄ was added. After pre-hydrolysis of the precursor for 1.5-2 hours, 0.2 ml of water was added for complete hydrolysis. To obtain TiO₂/Ag films, a solution of AgNO₃ was added to the mixture. TiO₂/Au films were produced by addition of 0.25 molar HAuCl₄·3H₂O solution. The content of Au and Ag in the films was 3 mol% and 5 mol% respectively. To synthesize binary films of TiO₂/ZrO₂ (70:30 molar ratio), two separate solutions were prepared. First, 2 ml of ethyl alcohol was mixed with 0.2 ml of AcAc and 0.1 ml of HCl to avoid precipitation. After that, 0.38 ml of Zr(OC₃H₇) was slowly added to the solution. Following 30-40 minutes of pre-hydrolysis, the former solution was added to the mixture of Ti(OC₃H₇)₄ with AcAc in ethyl alcohol. The films were deposited on *n*-type silicon substrates by dip-coating with a pull rate of 1.5 mm/s. The ~ 200 nm-thick films were hydrolyzed in air for 2 hours and then annealed. During annealing the temperature in the furnace was gradually raised from room temperature to 500°C at a rate of 2°C/min. As the temperature reached 500°C, the samples were kept in the furnace for 4 hours.

3.2. Stoichiometry and crystal structure of the samples

Figure 5 shows the X-ray diffraction (XRD) spectra of the TiO₂ film before and after Ti⁺ irradiation, exhibiting anatase structure in both cases. The XRD spectra were excited using 0.154 nm monochromatic CuK α radiation and measured using a DRON-3M diffractometer. A slight shift of the diffraction peak after irradiation (see inset of Figure 5) indicates strain induced by lattice distortion. XRD spectra for the TiO₂/Au, TiO₂/Ag, and TiO₂/ZrO₂ films (not shown) also revealed the anatase structure of the specimens.

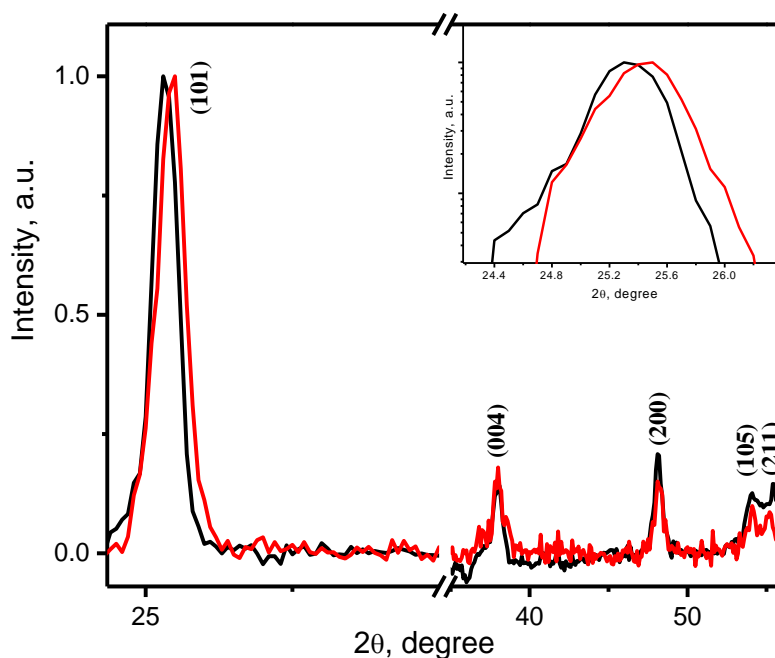


Figure 5. XRD spectra of TiO₂ films before (black) and after (red) Ti⁺ irradiation. Inset shows slight broadening and shift of the (101) anatase peak after irradiation.

Stoichiometry of the samples was determined using AES after *in situ* remote argon plasma cleaning for at least 30 minutes. Figure 6 shows an example of an AES spectrum for the Ag-containing film.

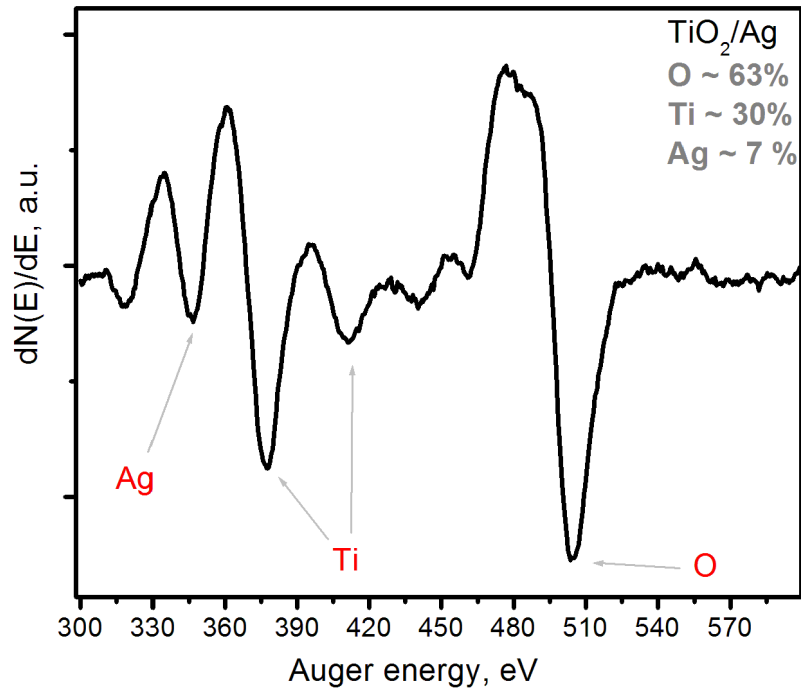


Figure 6. AES spectrum of TiO_2/Ag film after remote plasma cleaning.

To determine the necessary plasma cleaning time, we performed an experiment, where the plasma treatment time was gradually increased and the AES spectrum of the trial sample was taken after each treatment. The results of this experiment are shown in Figure 7. One can see that the content of carbon (one of the most abundant surface contaminants) decreased from $\sim 50\%$ to $\sim 3\%$ after 30 minutes of cleaning. Therefore, *in situ* remote argon plasma treatment demonstrated effectiveness in removing surface contaminants and was employed for each of the studied TiO_2 -based films. The AES spectra of the cleaned samples were obtained immediately after plasma cleaning.

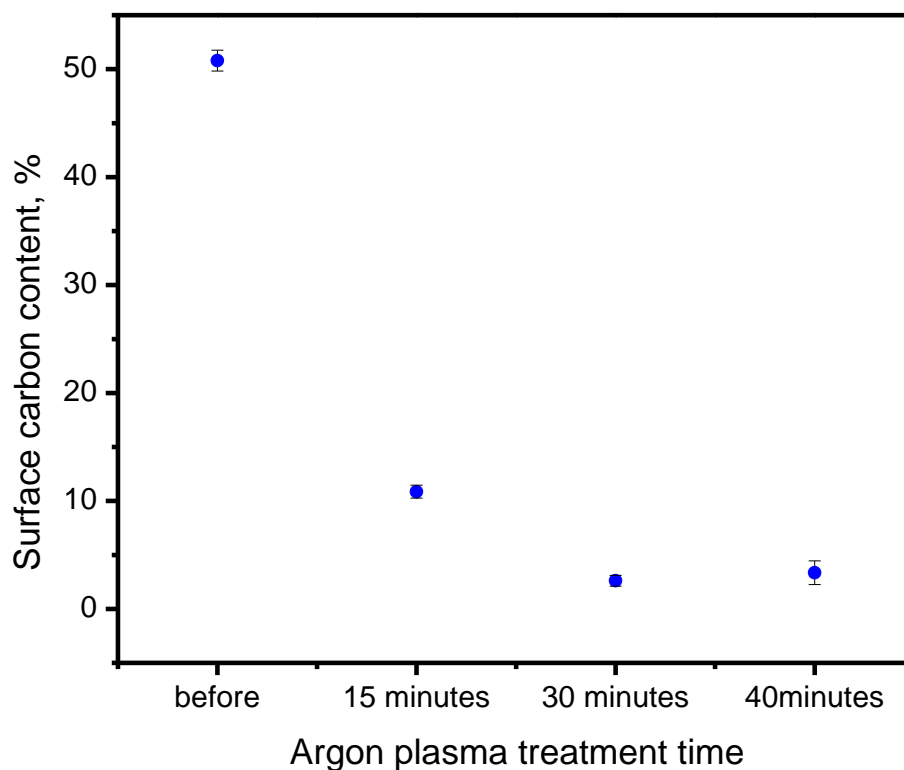


Figure 7. Content of carbon at the surface of a trial sample as a function of argon plasma treatment time.

Analysis of the AES spectra showed the following surface compositions:

TiO₂ film: ~35% Ti and ~ 65% O;

TiO₂/Ag film: ~ 31% Ti, 63% O and 7% Ag;

TiO₂/ZrO₂ film: ~ 28% Ti, 50% O and 22% Zr;

These compositions were calculated using Eq. 8. The calculated values agree well with the relative concentration of chemicals in solutions used for sample preparation. The gold-containing sample showed an expected (2:1) ratio of O:Ti while it was not possible to detect gold. We attribute this to the fact that the content of Au in the solution was as low as 3 mol%, while the AES sensitivity factor for gold is at least an order of magnitude smaller than those of Ti, O, Zr and Ag.

However, energy dispersive X-ray analysis of the TiO₂/Au sample (not shown) confirmed the presence of gold. Based on electron microscopy results (not shown here), the size of the Ag and Au nanoparticles in the TiO₂ films was ~ 7 nm, with noticeable clustering.

3.3 Electronic structure of the samples

Due to a low probability of the indirect bandgap luminescent transition in anatase TiO₂, this emission was not detected in PL spectra. The values of the bandgap E_g were determined by SPV spectroscopy. For all the samples the bandgap value is somewhat greater than reported in literature, probably due to quantum confinement effects. These are expected since the size of TiO₂ nanocrystallites is ~ 20-30 nm, as determined by electron microscopy (not shown). Below we discuss details of the electronic band structure separately for each type of the studied samples.

The PL spectra were fitted with multiple Gaussian peaks using the Origin software. The values of peak positions and peak intensities were determined by minimizing the root-mean-square error.

TiO₂

The band diagram based on the SPV and PL experiments for the as-received TiO₂ film is shown in Figure 8. The SPV and PL results are in good agreement. For the band diagrams in this dissertation we accept the VBM as the reference and the energies of the gap levels are labeled with respect to VBM. The directions of observed transitions are indicated with arrows. The italicized numbers next to arrows indicate the energies at which SPV transitions were observed experimentally. If the SPV transition was weak in intensity, the corresponding gap level is marked with a dashed line. For PL results, the italicized numbers indicate the energy of a PL

emission at low temperature (8 K). Since only the emission energy (not the direction of the observed transition) is measured in the PL experiment, there is an ambiguity in determining which band edge (valence or conduction) is involved in the transition. We assume that most of the PL features observed in our samples are associated with transitions to VBM (e.g., the 2.4 eV and 2.7 eV states in Figure 8) since the presence of such states was reported previously (see Table 1 for references). However, for some states this assertion may not be assured. For example, the PL emission at 2.2 eV could be a result of a transition from the conduction band to the 1.4 eV state, or a transition from the 2.2 eV state to the valence band (see Figure 8). Based on our results we do not rule out either of the possibilities, so such transitions are shown as dashed arrows in the PL portion of the band diagram (corresponding gap states are also shown as dashed lines). For other samples, such transitions and the corresponding energy levels are shown in dashed lines as well.

For the pristine TiO₂ thin film the following three gap states were detected by SPV: at ~ 1.4 eV, ~ 2.0 eV and ~ 2.4 eV above VBM. In general, the direction of an SPV transition is determined from the direction of the slope change in the plot of the contact potential difference as a function of energy. For example, an “inward knee” at energy E_t corresponds to the transition from VBM to the gap level at E_t . In our sample, the VBM-to-1.4 eV and VBM-to-2.0 eV transitions were observed as “inward knees” in the SPV spectrum (see Figure 9) and thus could be designated in the band diagram as 1.4 eV and 2.0 eV energy levels. It should be noted that the slope change at 1.4 eV is very weak, so the 1.4 eV state is indicated by a dashed line in Figure 8.

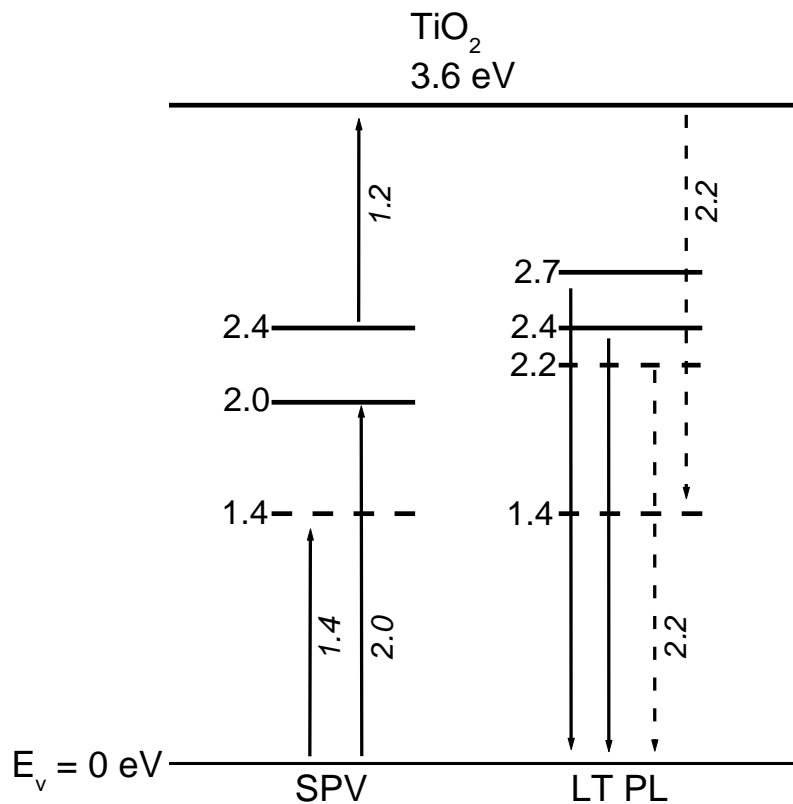


Figure 8. Band diagram of the anatase TiO₂ thin film based on the SPV (left) and low temperature PL results (right).

An “outward knee” in the SPV spectrum at energy E_t' indicates that the transition occurs from the state at E_t' to the conduction band. The E_t' energy interval in this case is measured from the bottom of the conduction band, so in our band diagram (where VBM is the reference) this state will be at $E_g - E_t'$. An example of this type of transition is the “outward knee” in the SPV spectrum at 1.2 eV which corresponds to the gap state at 2.4 eV above VBM (see Figures 8 and 9). The error in determining the values of SPV transitions could be up to 0.1 eV.⁸⁰

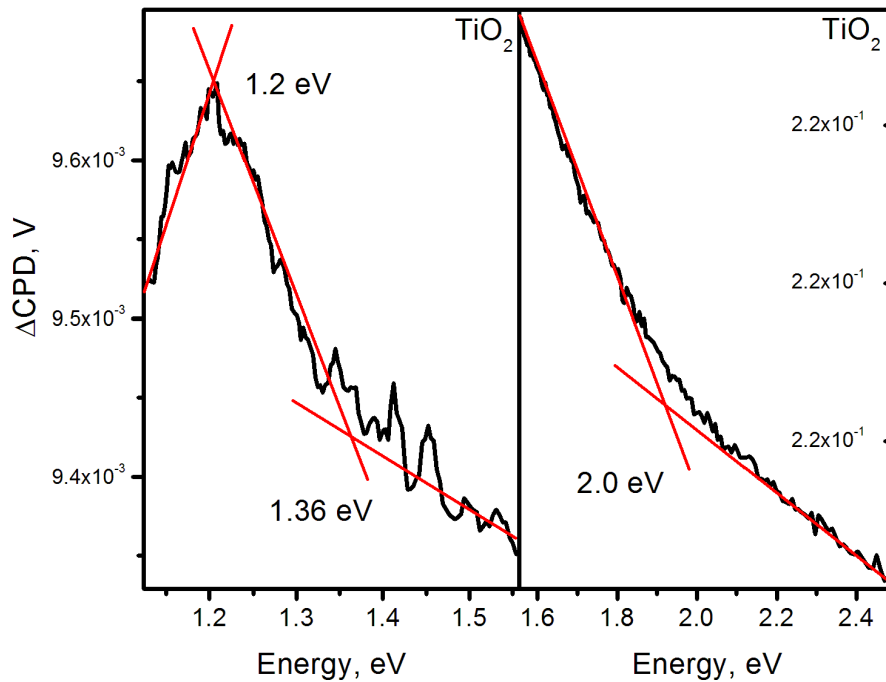


Figure 9. SPV spectra of a TiO₂ thin film. Transitions at 1.2 eV, 2.0 eV and a weak transition at ~ 1.4 eV are shown.

Emission bands at 2.2 eV, 2.4 eV and 2.7 eV were resolved in low temperature PL spectra (see Figure 10). As mentioned above, it is not clear whether the 2.2 eV emission is associated with the transitions from the conduction or into the valence band. States at 2.4 eV and 2.7 eV were previously reported for anatase TiO₂. Synthetic TiO₂ is usually reduced and contains such native defects as oxygen vacancies (V_o) and/or titanium interstitials. These defects can easily form during growth and post-growth treatments. Some DFT calculations show that creation of V_o is more favorable. Oxygen deficiency leads to formation of F , F^+ , and F^{++} color centers and/or Ti^{3+} ions, all of which introduce their energy levels within the bandgap and thus affect light absorption and charge carrier dynamics in TiO₂ (see references in the introduction). There is no certainty in assigning particular energy levels specifically to the V_o - or the Ti^{3+} -related states.

In our TiO₂ sample, the states at 2.0 eV, 2.4 eV observed in the SPV spectra as well as the states at 2.2 eV and 2.7 eV observed in the PL spectra can be attributed to oxygen deficiency (see Table 1). The intensity of the ~ 1.4 eV SPV transition is relatively weak in the pristine sample (Figure 9), yet in the modified samples it becomes more pronounced (see below). Incidentally, the ~ 2.2 eV PL emission could result from a transition involving this state, as shown in Figure 8. To the best of our knowledge, the 1.4 eV state in TiO₂ was not reported in SPV experiments. Therefore, the origin of this state remains unclear and more experiments are necessary to confirm presence of this state in the near-infrared energy range

In the TiO₂ film, we observed the ~ 2.3-2.4 eV emission at both low and room temperatures (the 8 K spectrum is shown in Figure 10).

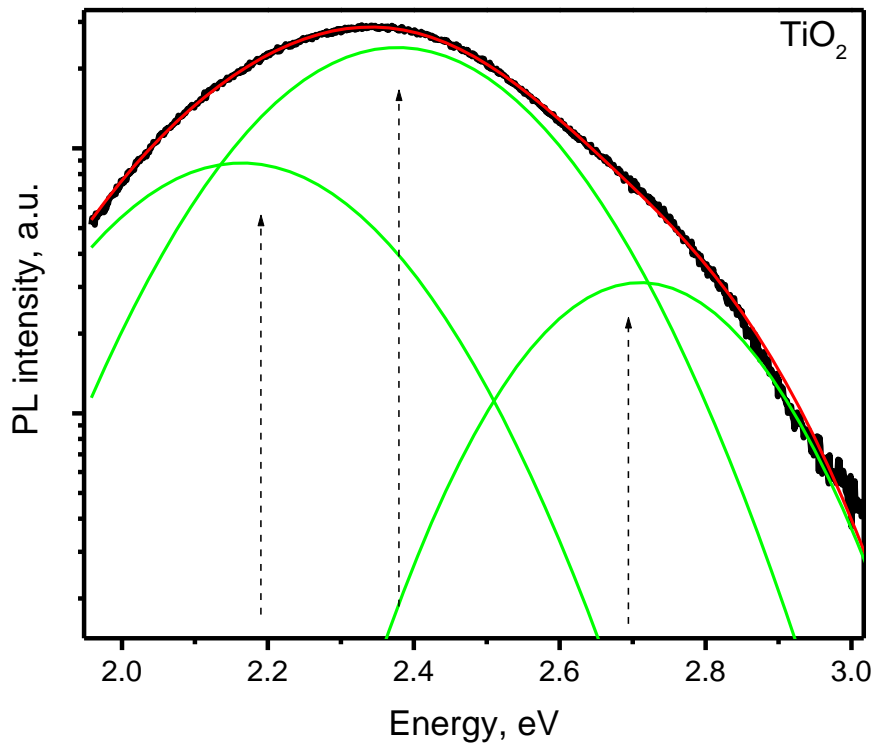


Figure 10. Low temperature (8 K) spectrum of the TiO₂ thin film.

As we mentioned above, the low temperature PL band at $\sim 2.3\text{-}2.4$ eV was reported in the literature for anatase single crystals and nanostructures. Commonly it is attributed to the recombination of self-trapped excitons (STE). STE are likely formed in anatase TiO_2 (not in rutile!) upon superbandgap excitation due to a strong exciton-phonon interaction. With increase in temperature, STE emission in TiO_2 was reported to shift to higher energies and quench significantly at room temperature.

However, the PL band at $\sim 2.3\text{-}2.4$ eV is still observed for some TiO_2 samples at room temperature. On the other hand, in anatase nanoparticles the ~ 2.3 eV PL band was attributed to oxygen vacancies. In the TiO_2 films studied here we observe the $\sim 2.3\text{-}2.4$ eV PL band at low temperature in all samples and at room temperature only in two samples – TiO_2 and TiO_2/Ag . Thus, it is possible that in those samples where the $\sim 2.3\text{-}2.4$ eV PL emission is observed at both temperatures (295 K and 8 K), STE do contribute to emission at 8 K while the defect-mediated recombination is dominating at room temperature. The 2.4 eV level was detected in SPV experiments at room temperature as a well-pronounced “knee” at 1.2. eV (cf. Figure 9). In view of the discussion above, we attribute this state to oxygen deficiency.

Overall, at least four different states were detected within the bandgap of the as-received anatase TiO_2 thin film: 2.0 eV, 2.2 eV, 2.4 eV and 2.7 eV. Conventionally, the literature attributes these states to oxygen deficiency. At low temperature, the 2.4 eV PL emission could also be related to formation and recombination of STE. Thus, even prior to modification, the bandgap of TiO_2 has a significant number of gap states, which could act as recombination centers for UV-generated charge carriers.

TiO₂/Ag

What visible light-active gap states are induced as a result of Ag modifications of sol-gel grown anatase TiO₂?

Our experiments indicate that Ag doping introduces new states within the TiO₂ bandgap. Figure 11 juxtaposes electronic band gap diagrams of the TiO₂ and TiO₂/Ag samples.

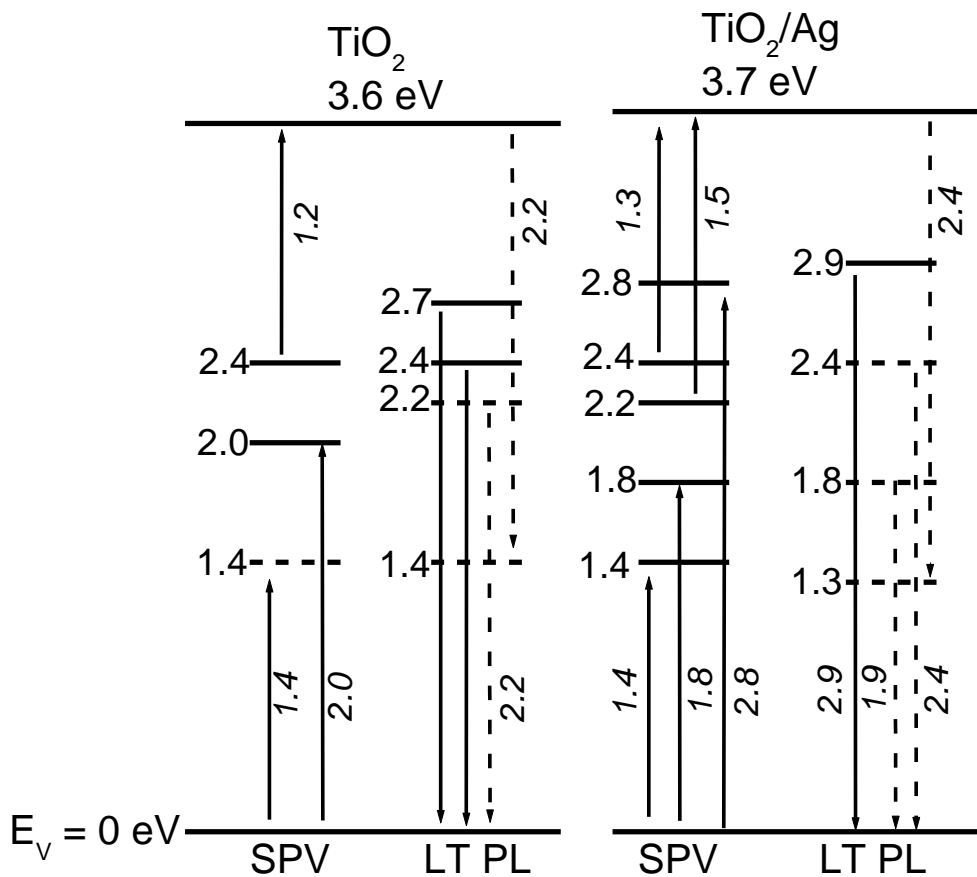


Figure 11. Band diagrams of TiO₂ and TiO₂/Ag samples.

As in the undoped TiO₂ sample, the energy level at 1.4 eV remains after Ag introduction. The intensity of the corresponding SPV transition in TiO₂/Ag is noticeably greater than in the

pristine TiO_2 (cf., Figures 9 and 12(A)). Gap states at 2.2 eV and 2.4 eV above VBM (Figure 11) contribute to the SPV transitions into the conduction band (see Figure 12A, “outward knees” at 1.5 eV and 1.3 eV). Figure 12(B) shows the bandgap transition at ~ 3.7 eV and a transition at ~ 2.8 eV from VBM. These states (2.2 eV, 2.4 eV and 2.8 eV) can be assigned to oxygen deficiency present in the Ag-modified film (see Table 1).

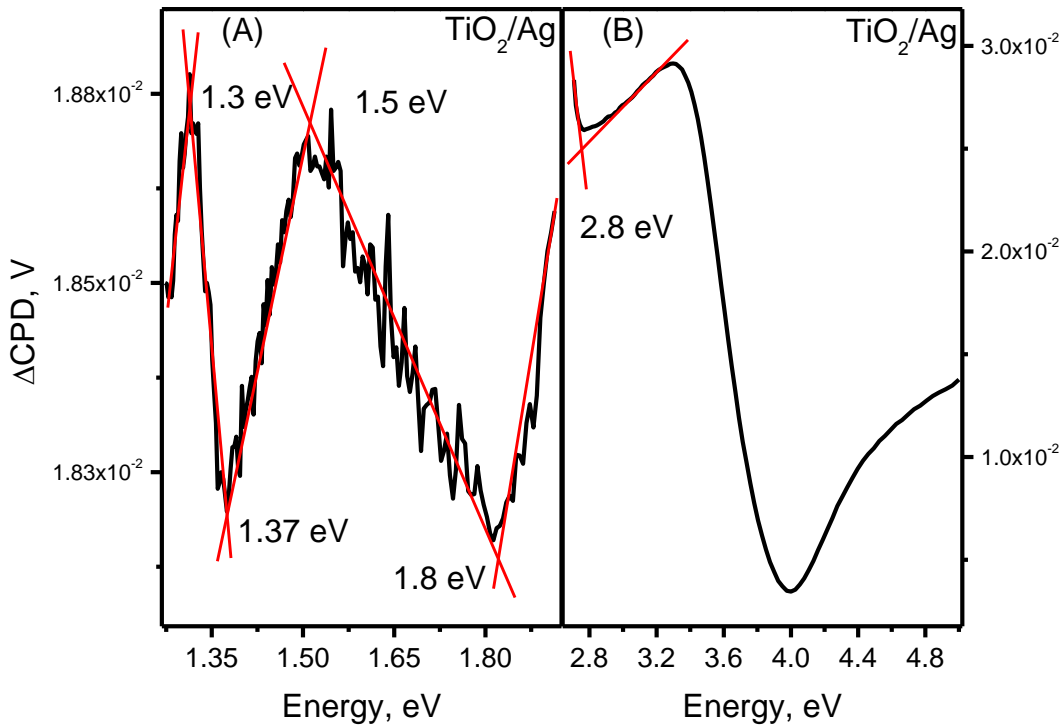


Figure 12. (A) SPV spectra for the TiO_2/Ag film showing transitions at 1.3 eV, 1.5 eV into the conduction band and 1.4 eV and 1.8 eV from the valence band. (B) Transition at 2.8 eV from the valence band and the bandgap transition at ~ 3.7 eV.

A new gap state at 1.8 eV was detected for the TiO_2/Ag film (Figure 12A). The corresponding SPV transition at 1.8 eV is shown in Figure 13. This state is not present in the undoped sample and we suggest that it arises due to Ag incorporation. Our hypothesis is supported by DFT calculations for Ag-doped TiO_2 ,⁴⁶ which yield a nonzero density of states in the middle of the

gap arising as a result of mixing of the Ag $4d$ and Ti $3d$ states. Such Ag-induced state could be responsible for an enhanced absorption of visible light and improved PC activity of the TiO_2/Ag system.⁵⁰ It should be mentioned that another Ag-related state in TiO_2/Ag nanoparticles was observed by absorption spectroscopy, but with a different location in the gap.⁸⁷

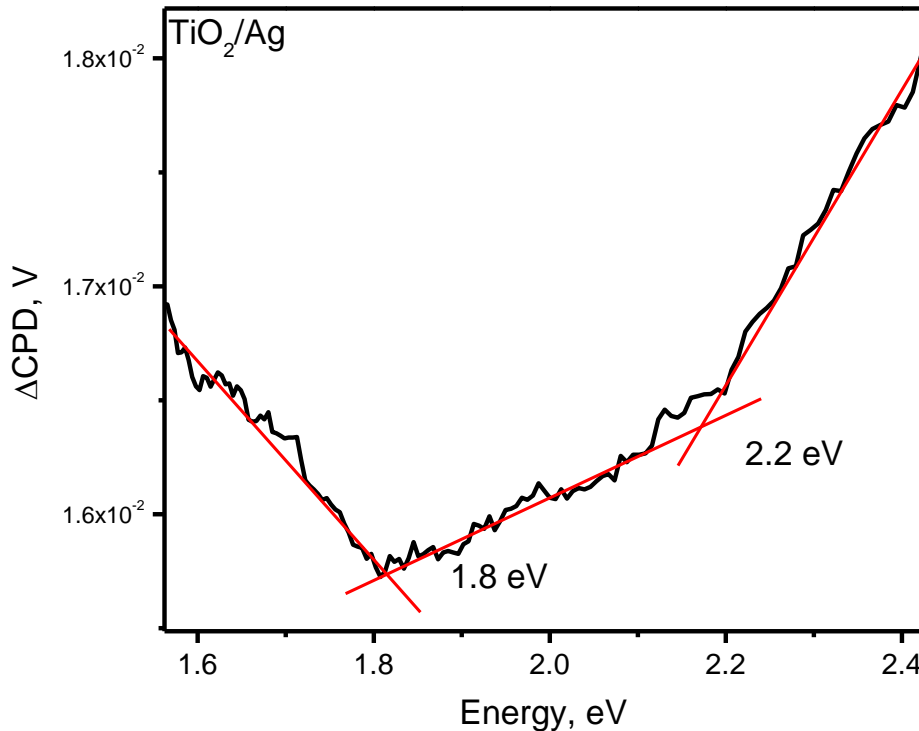


Figure 13. SPV transitions at ~ 1.8 eV and ~ 2.2 eV from VBM in the TiO_2/Ag film.

Pronounced differences between the TiO_2 and TiO_2/Ag films were also observed in the low temperature PL spectra. In contrast to the TiO_2 sample case, only two distinct luminescence bands were resolved after fitting the PL spectrum of TiO_2/Ag (Figure 14). It is possible that an additional very weak band centered below 2 eV is present, although its position could not be determined due experimental limitations (overlap with the first diffraction maximum of the laser line). This PL emission could be located at ~ 1.8 - 1.9 eV and thus related to the Ag-induced SPV transition at 1.8 eV discussed above. Thus, for the TiO_2/Ag film, the main contribution to the PL

emission at low temperature comes from the 2.4 eV band (Figure 14). The intensity of the band in the high-energy tail of the spectrum (2.9 eV) is rather weak. Nevertheless, the peak positions of the PL bands at 2.4 eV and 2.9 eV are in good agreement with our SPV results (see Figure 11). The PL emission at 2.9 eV and the SPV transition at 2.8 eV (cf. Figure 12B) are probably related to the same state (at $\sim 2.8\text{-}2.9$ eV above the VBM), assigned to oxygen deficiency.

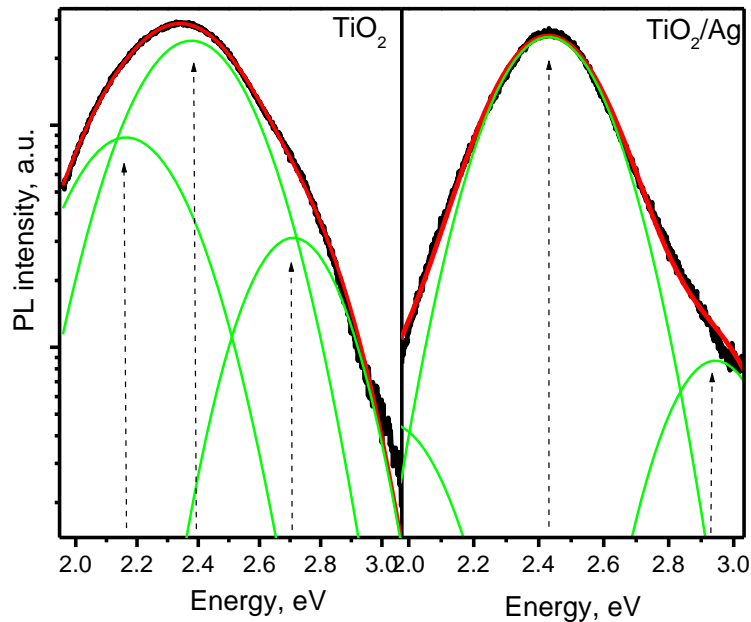


Figure 14. PL spectra measured at 8 K for the TiO_2 film (left) and the TiO_2/Ag film (right).

The origin of the states at 2.4 eV observed in both TiO_2 and TiO_2/Ag films is likely the same. Similarly to the TiO_2 sample, this state was detected in TiO_2/Ag by SPV as well as PL at room temperature (not shown) and at 8 K (Figure 14). As already mentioned, the low temperature PL emission at $\sim 2.3\text{-}2.4$ in TiO_2 is usually assigned to the STE recombination. On the other hand, room temperature emission at the same energy has been attributed to oxygen deficiency-related recombination. Thus, it is possible that both types of the emission could be observed at low temperature, whereas at room temperature – only the one arising from defect

recombination. Furthermore, as the diagram in Figure 11 shows, the transitions from the 1.3 eV energy level to the conduction band could also produce a PL emission at 2.4 eV. Additional measurements in the near-infrared spectral range could further elucidate the band structure of the sample.

Overall, based on the results shown above, the bandgap of TiO₂/Ag is rich in states that could be active in visible light. Most of these gap levels (2.2 eV, 2.4 eV and 2.8 eV) are related to oxygen deficiency. Moreover, in addition to the Ag-induced state at 1.8 eV, the F , F^+ , F^{++} color centers and/or the Ti³⁺ defects could have a direct influence on the PC activity of the TiO₂/Ag system in visible and UV light. Figure 15 shows the bar graph of the normalized intensities of PL bands in the TiO₂/Ag film juxtaposed with those of the TiO₂ film. One can see that as silver is added to TiO₂, the emission at 2.2 eV disappears and the relative intensity of the band in the high-energy tail of the PL spectrum increases slightly (cf. intensities of the 2.7 eV band in the TiO₂ film and the 2.9 eV band in the TiO₂/Ag film in Figure 15). These changes could result from a partial oxidation of silver at the TiO₂/Ag interface and/or creation of different color centers and Ti³⁺ ions during growth and post-growth treatment of TiO₂/Ag, as compared to TiO₂.

Within the assumption that the 2.4 eV emission at low temperature is attributed to the recombination of STE in TiO₂, the increase in the 2.4 band intensity after Ag-addition could be related to the disappearance of the 2.2 eV-type defects in the TiO₂/Ag sample. With fewer such defects in the sample, the self-trapping of excitons becomes more probable leading to an increase of the 2.4 eV band relative intensity. Additional experiments are necessary to confirm the STE nature of the 2.4 eV emission.

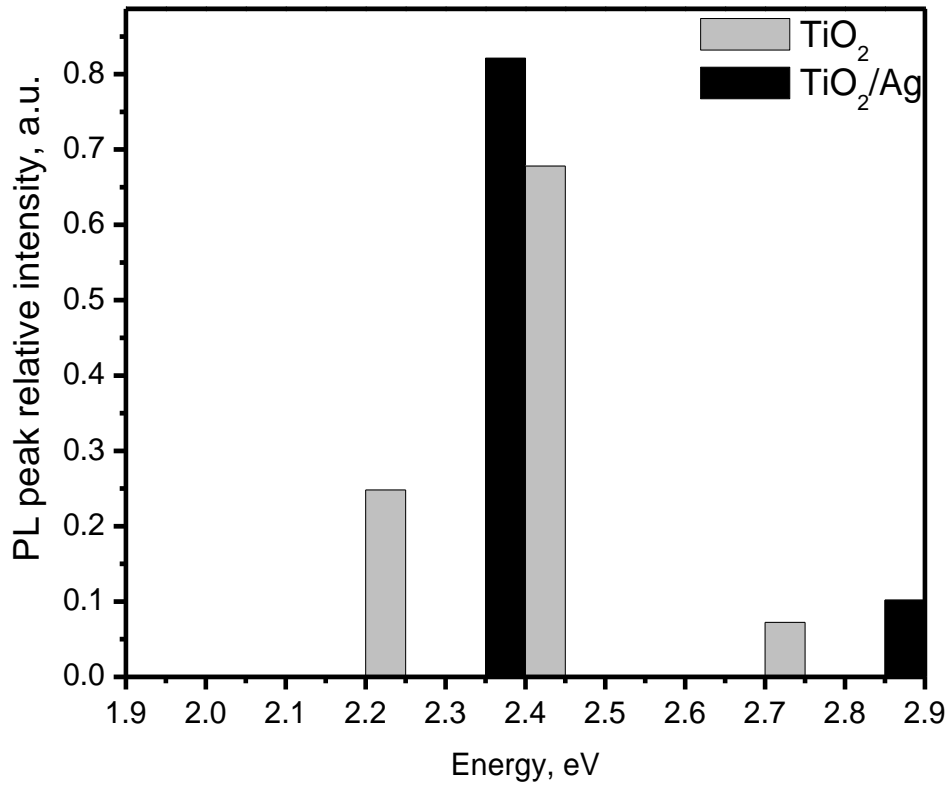


Figure 15. Relative intensities and spectral locations of the low temperature PL bands in the TiO₂ and TiO₂/Ag thin films. The values on the y-axis represent intensities of individual peaks, normalized to the total intensity.

TiO₂/Au

What visible light-active gap states are induced as a result of Au modifications of sol-gel grown anatase TiO₂?

Our results show that addition of gold introduces only minor changes into the electronic structure of TiO₂. Figure 16 compares the band diagrams of TiO₂ and TiO₂/Au.

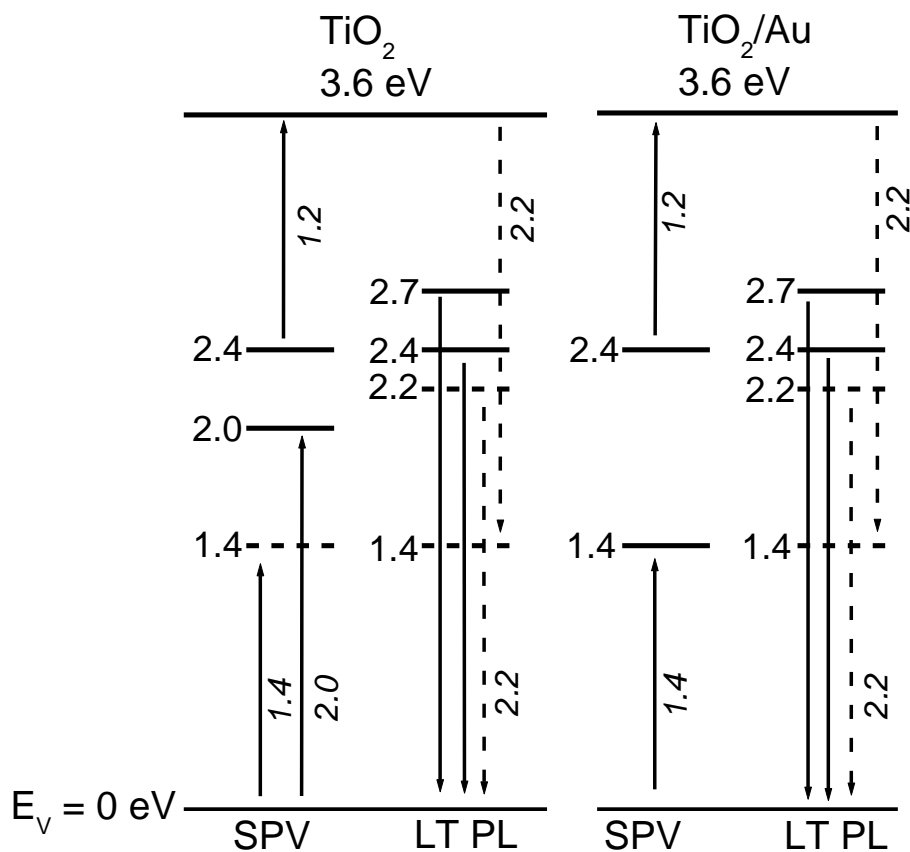


Figure 16. Band diagrams of TiO_2 and TiO_2/Au films.

In the SPV portion of these diagrams one can see that most of the gap states in the TiO_2/Au film are the same as in the pristine TiO_2 sample, with the exception of the midgap region (2.0 eV state). The bandgap value remains unchanged after Au addition (Figure 17(A)), which is consistent with studies reported in Ref. 42. The state at 2.4 eV detected by SPV was observed in both pristine and Au-modified samples. Another common gap state at 1.4 eV is marked on the band diagram in a dashed line. The corresponding SPV transitions – at 1.4 eV (from the valence band) and at 1.2 eV (into the conduction band) – are shown in Figure 17(B). The slope change at 1.4 eV is more pronounced in the TiO_2/Au film than a similar transition in TiO_2 (cf. Figure 9), however both transitions are relatively weak.

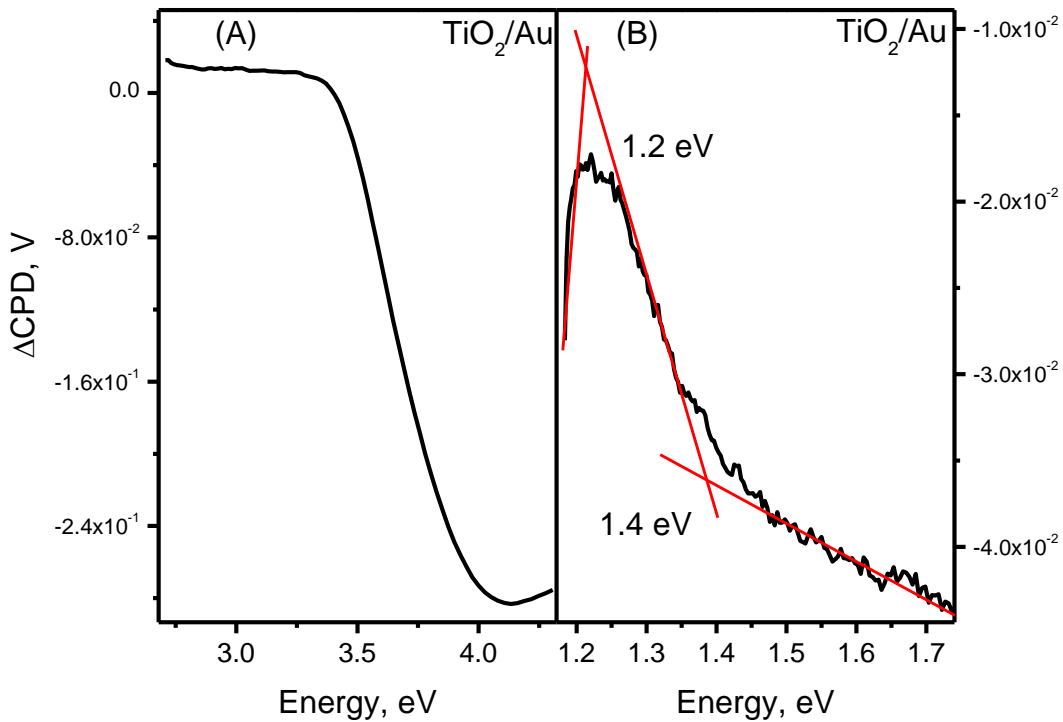


Figure 17. SPV spectra of TiO_2/Au film.

On the other hand, the ~ 1.4 eV SPV transition is significantly stronger in the TiO_2/Ag (compare Figures 9, 12(A) and 17(B)). Such changes in the intensity of the same transition with the composition of the sample are noteworthy, although, as mentioned above, the origin of the 1.4 eV transition is not certain.

The gap state at 2.4 eV could be related to TiO_2 reduction (caused by oxygen deficiency). Possibly the same state (within experimental error) was detected by room temperature PL measurements, where an emission band at 2.5 eV was resolved (not shown here). Therefore, the SPV transition at 1.2 eV (from the level 2.4 eV above VBM) and the room temperature PL band at 2.5 eV are likely related to the same gap state.

The 2.0 eV state present in the pristine film was not observed in the SPV spectra after gold addition (cf. band diagram in Figure 8). In literature the 1.95 eV PL emission was attributed to oxygen vacancies in single crystals (see Table 1). A similar state at 2.1 eV was observed in

SPV spectra for rutile TiO_2 thin film and was assigned to V_o (see Table 1). Absence of the 2.0 eV state in our TiO_2/Au sample could be related to changes in stoichiometry.

In the previous section it was mentioned that silver addition caused significant change in both the peak positions and intensities of PL bands (see Figure 15). The low temperature PL spectrum of the Au-modified TiO_2 does not differ significantly from that of the pristine TiO_2 , as seen in Figure 18. The positions of the peaks are the same as in TiO_2 sample – 2.2 eV, 2.4 eV and 2.7 eV. The bands at 2.2 eV and 2.7 eV (as already mentioned) are related to reduction of TiO_2 . The low temperature PL emission at 2.4 eV was also discussed above. Figure 19 shows the bar plot of the normalized peak intensities in the TiO_2 and TiO_2/Au samples. The slight changes in the relative peak intensities could be related to the changes in stoichiometry as well as content and type of defects, all resulting from Au incorporation.

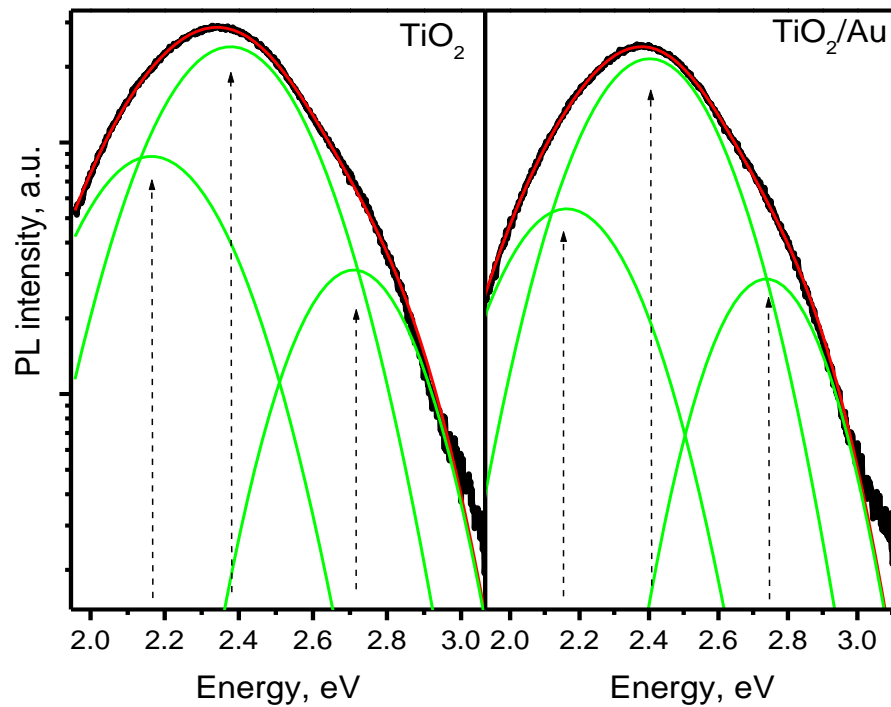


Figure 18. PL spectra of TiO_2 and TiO_2/Au films, measured at 8K.

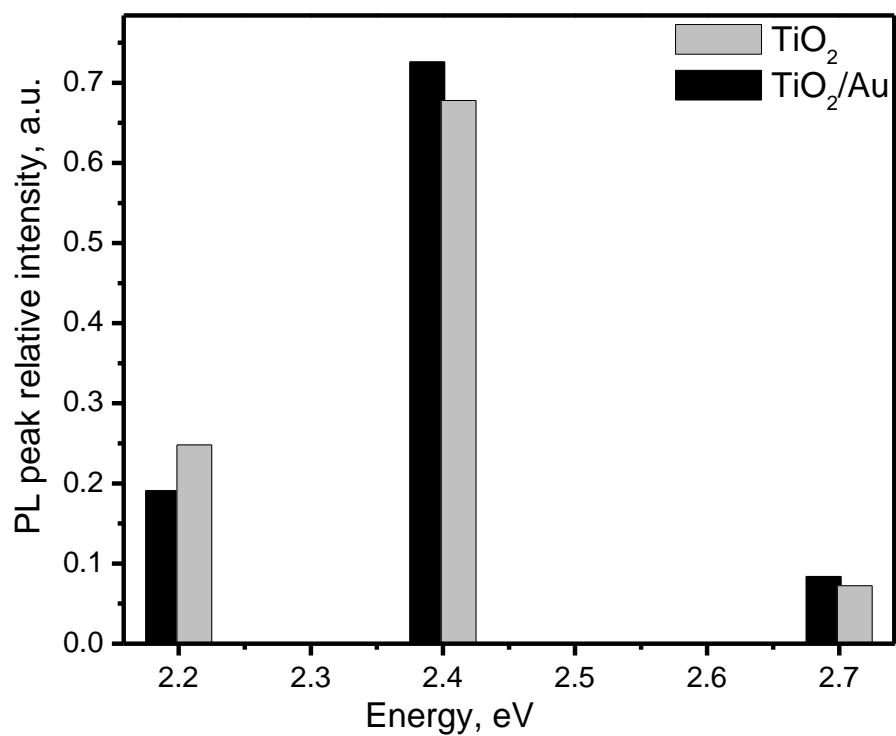


Figure 19. Normalized intensities and spectral locations of low temperature PL peaks for TiO₂ and TiO₂/Au thin films.

Hence, our results suggest that the electronic structure of the TiO₂/Au does not differ appreciably from that of the TiO₂ system. The reported enhanced visible light PC activity of TiO₂/Au is usually attributed to the presence of Au plasmon resonance absorption band at ~ 2.45 eV, which cannot be observed in our experiments.

TiO₂/ZrO₂

What visible light-active gap states are induced as a result of ZrO₂ modifications of sol-gel grown anatase TiO₂?

The effects of ZrO₂ incorporation into TiO₂ are shown in Figure 20.

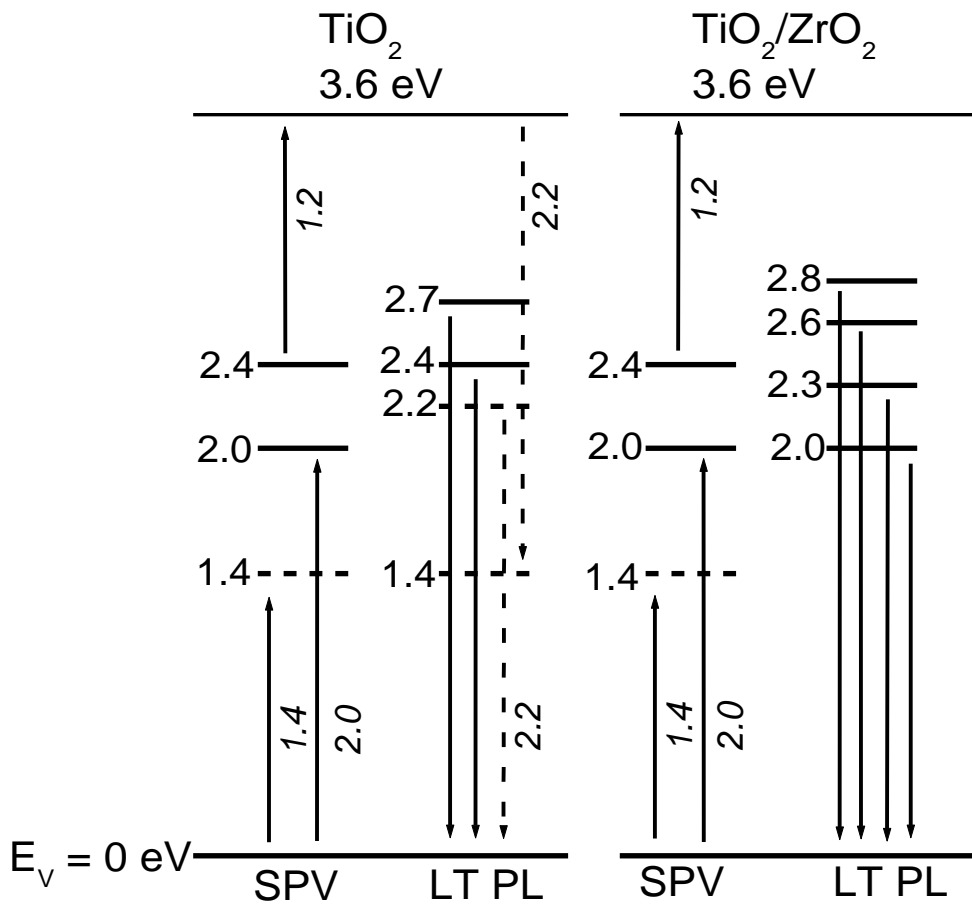


Figure 20. Band diagrams of TiO₂ and TiO₂/ZrO₂ based on SPV and low temperature PL results.

The SPV portions of the two diagrams are rather similar whereas more differences could be seen in the low temperature PL part of the diagram. The states at 1.4 eV and 2.0 eV detected by SPV are preserved after addition of ZrO_2 . The 2.4 eV state observed in the pristine sample, in $\text{TiO}_2/\text{ZrO}_2$ most likely yields an SPV transition at 1.2 eV into the conduction band. Figure 21 shows the SPV transitions at 1.2 eV into the conduction band, 1.4 eV from the valence band, and the 2.0 eV state as SPV transition involving the valence band. Figure 22 shows the bandgap transition at ~ 3.6 eV.

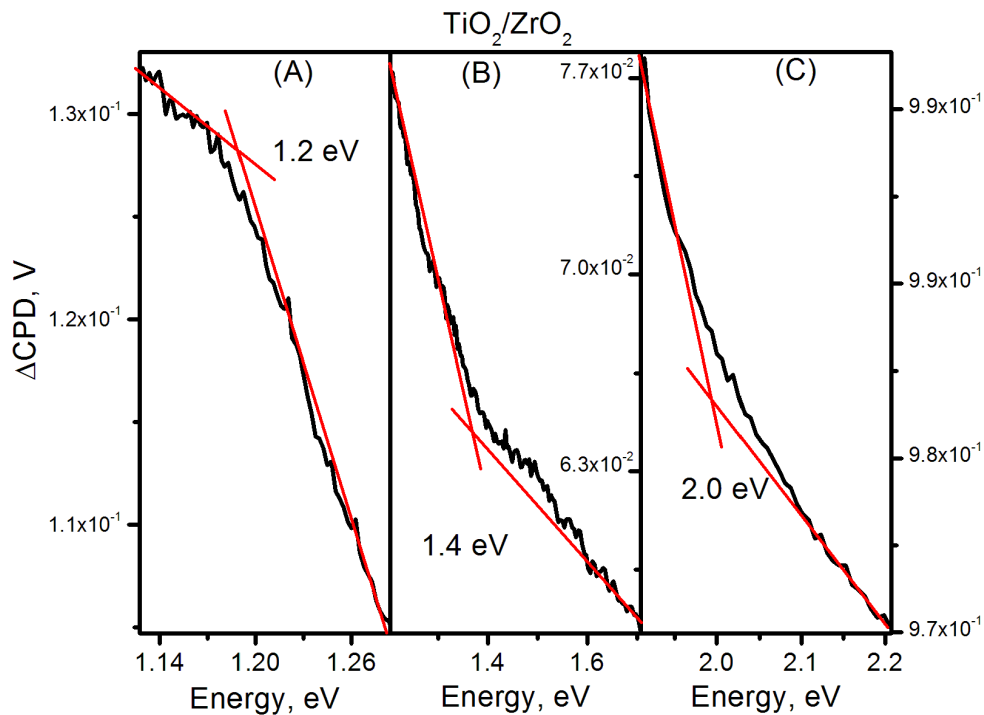


Figure 21. SPV spectra of $\text{TiO}_2/\text{ZrO}_2$. The transitions shown are (A) 1.2 eV into the conduction band (B) 1.4 eV from the valence band and (C) a relatively weak transition at 2.0 eV from the valence band.

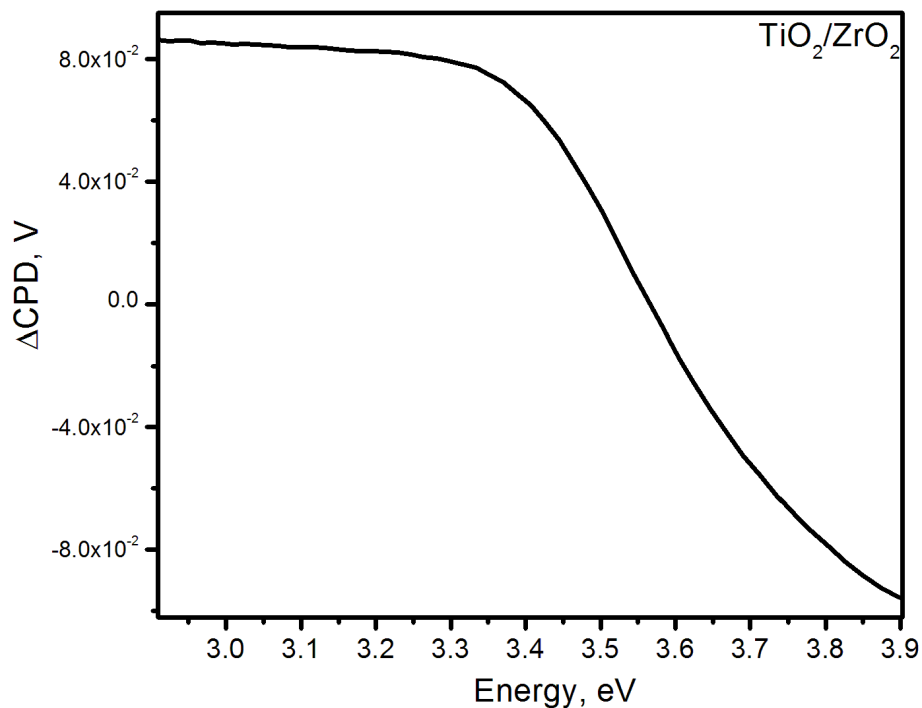


Figure 22. SPV spectrum of TiO₂/ZrO₂ showing the bandgap transition at ~ 3.6 eV.

The intensity of the 1.4 eV transition in TiO₂/ZrO₂ is comparable to the intensity of the same transition in the TiO₂/Au sample. In our samples, this transition is the most intense in the TiO₂/Ag sample and the weakest in the TiO₂ film. As we already mentioned, this gap state was not reported in literature and more experimental studies are necessary to make an adequate assignment of its nature. The state at 2.0 eV is related to color centers. An increase in the number of luminescent centers is seen in our PL results (Figure 23). The low temperature PL spectrum of TiO₂/ZrO₂ is rather different from that of the pristine TiO₂. The PL emission is a superposition of four Gaussians, not three, as in the TiO₂ sample. The positions of resolved peaks differ from those for the TiO₂ sample (Figure 10), which is also indicated on the band diagram of Figure 20. All these gap states are likely related to oxygen deficiency. Some of these

states are also observed in SPV measurements. E.g., the position of the 2.0 eV PL peak agrees well with the gap state at 2.0 eV observed by SPV (see above).

It should be noted that for this sample, we do not assign the low temperature PL band at 2.3 eV to STE recombination. First of all, the FWHM of this band is similar to the widths of the defect-related bands. For the rest of the samples, the 2.4 eV band was wider, than the defect-related bands, which is consistent with the nature of STE. Secondly, the increased number of defects in this sample could prevent the formation of STE.

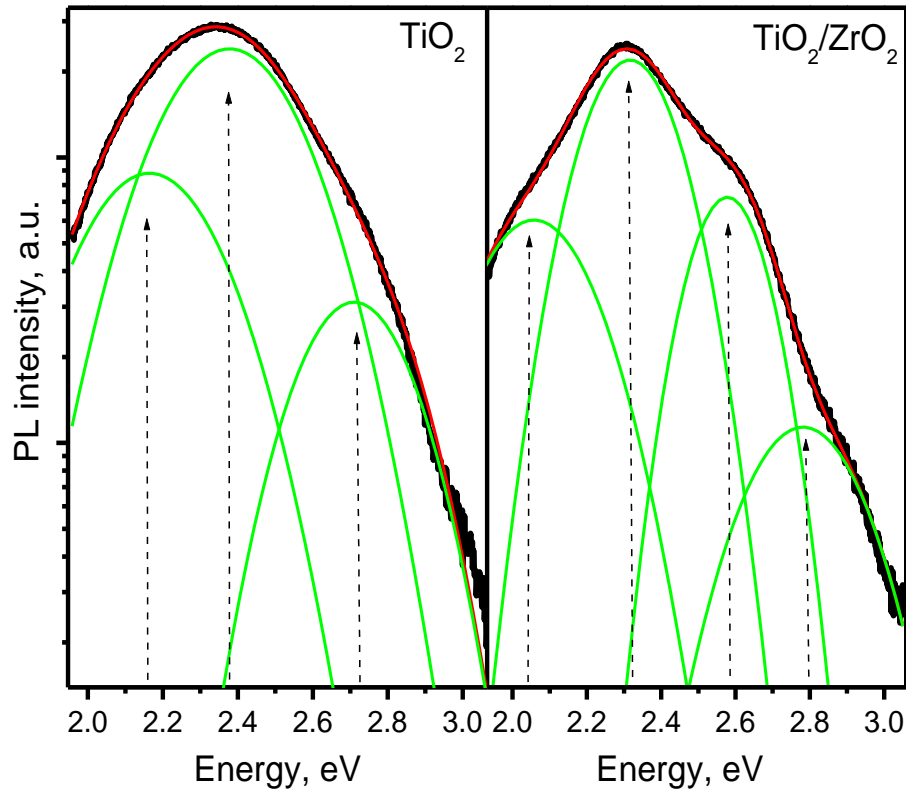


Figure 23. PL spectra of TiO_2 and $\text{TiO}_2/\text{ZrO}_2$ taken at 8K temperature.

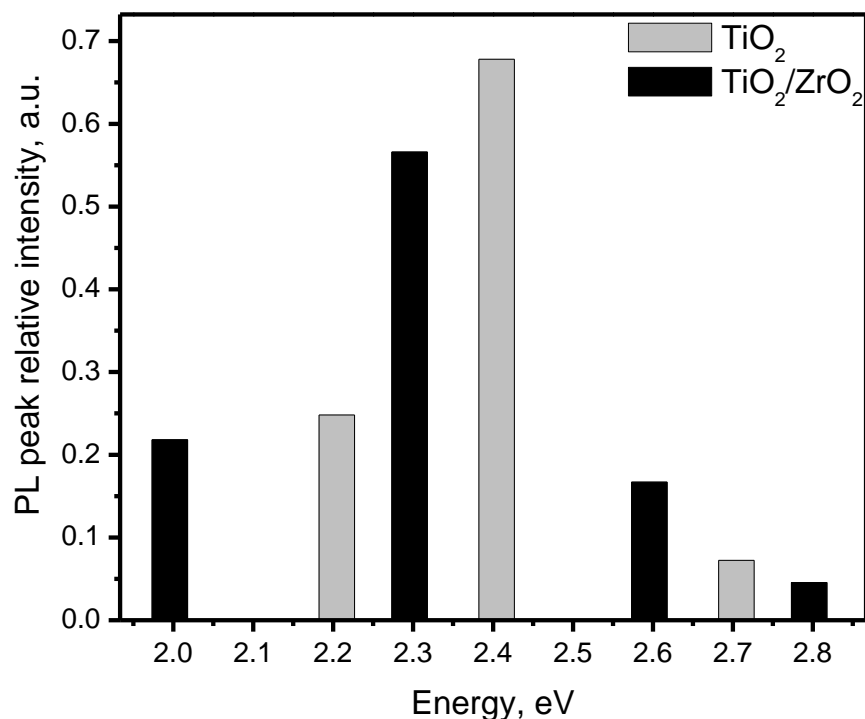


Figure 24. Normalized intensities and spectral locations of the PL bands, resolved in the spectra of Figure 23.

From the diagram in Figure 20 and the bar plot in Figure 24 one can see that there is a certain increase in the number of states related to TiO₂ reduction (oxygen vacancies and/or Ti³⁺ states). As described in the introduction, addition of ZrO₂ to TiO₂ could result in creation of structural defects, such as oxygen vacancies. Ref. 88 attributes this to the different ionic radii of Ti and Zr atoms. It is suggested that V_o could be formed to reduce the lattice strain, caused by a substitution of Ti atoms with larger Zr atoms.⁸⁸ Overall, our analysis of zirconia-modified TiO₂ shows that addition of ZrO₂ does not seem to induce Zr-related states; only the number and/or type of color centers is changed. Improved UV light PC activity of the TiO₂/ZrO₂ could be attributed to an increased surface area and/or increased oxygen deficiency content.

3.4 Effects of Ti^+ irradiation (self-doping)

How does irradiation affect electronic structure of these TiO_2 -based films?

Our results show that Ti^+ -irradiation did not cause significant changes in the electronic structure of our samples. We did not detect any systematic changes related to a specific defect state. The electronic bandgap structure remained mostly unchanged with the dominating contribution from the oxygen deficiency-related states. The number of such states increased slightly compared to the non-irradiated samples. PL spectra showed that the same luminescent bands were resolved after Ti^+ -irradiation with minor position and intensity variations from sample to sample, with a dominating emission still at 2.4 eV. Figures 25A and 25B illustrate this point. The absence of systematic changes could be due to the fact that, even prior to irradiation, the native defect content is not the same in each film, as shown in the previous sections (c.f. bar plots for all non-irradiated samples).

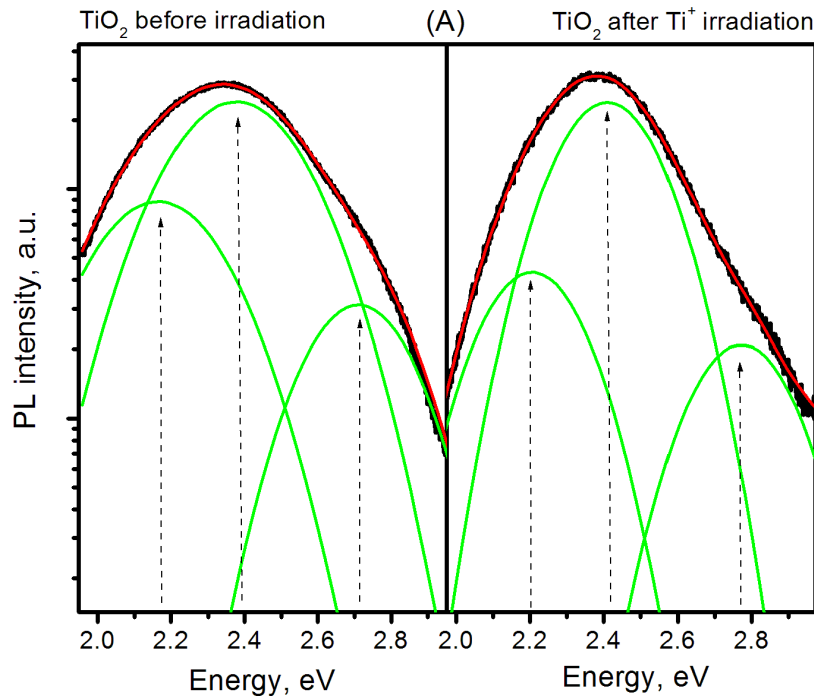


Figure 25(A). Comparison between low temperature PL spectra of the self-doped TiO_2 . No significant changes are observed after Ti^+ -irradiation.

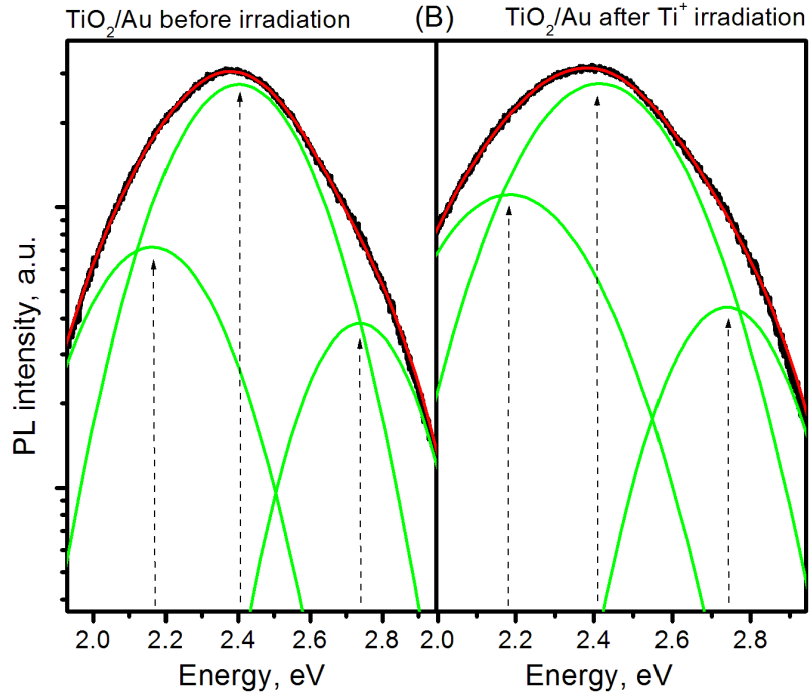


Figure 25(B). Comparison between low temperature PL spectra of the self-doped TiO_2/Au films. No significant changes are observed after Ti^+ -irradiation.

Additionally, such low-energy irradiation was instrumental in confirming the presence of certain gap states. For example, after Ti^+ irradiation, the gap state in the near-infrared range (at 1.4 eV above the VBM) is observed in the SPV spectra of most of the samples (this transition is very weak in TiO_2 and not observed in the Au-containing TiO_2). Figure 26 shows this transition for the $\text{TiO}_2/\text{ZrO}_2$ and TiO_2/Ag films. The intensity of this SPV transition follows a trend similar to that observed in non-irradiated samples, although with a greater amount of spectral noise in some samples: it is weak in the TiO_2 and $\text{TiO}_2/\text{ZrO}_2$ films, stronger in the TiO_2/Ag sample, and not observed in the TiO_2/Au film.

As discussed above, in SPV experiments we observed a 1.8 eV gap state in the non-irradiated TiO_2/Ag film and assigned it to Ag doping. After Ti^+ irradiation we also detected an SPV transition at 1.7 eV exclusively in the TiO_2/Ag sample (see Figure 27). This supports the hypothesis that the $\sim 1.7\text{-}1.8$ eV gap state could indeed be related to Ag doping.

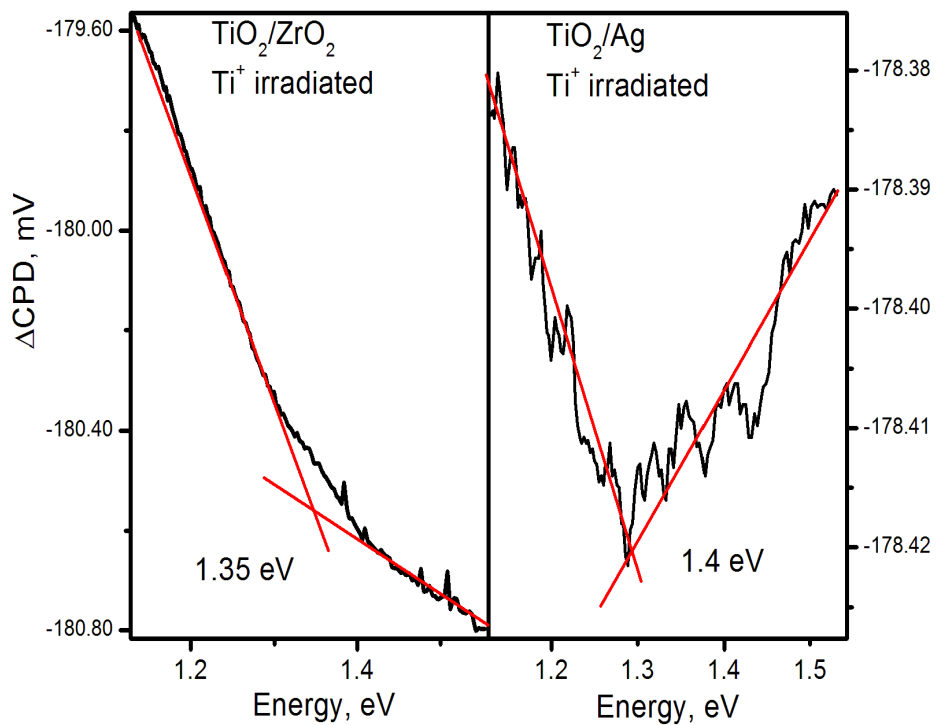


Figure 26. SPV transition at 1.4 eV observed in $\text{TiO}_2/\text{ZrO}_2$ and TiO_2/Ag after Ti^+ irradiation.

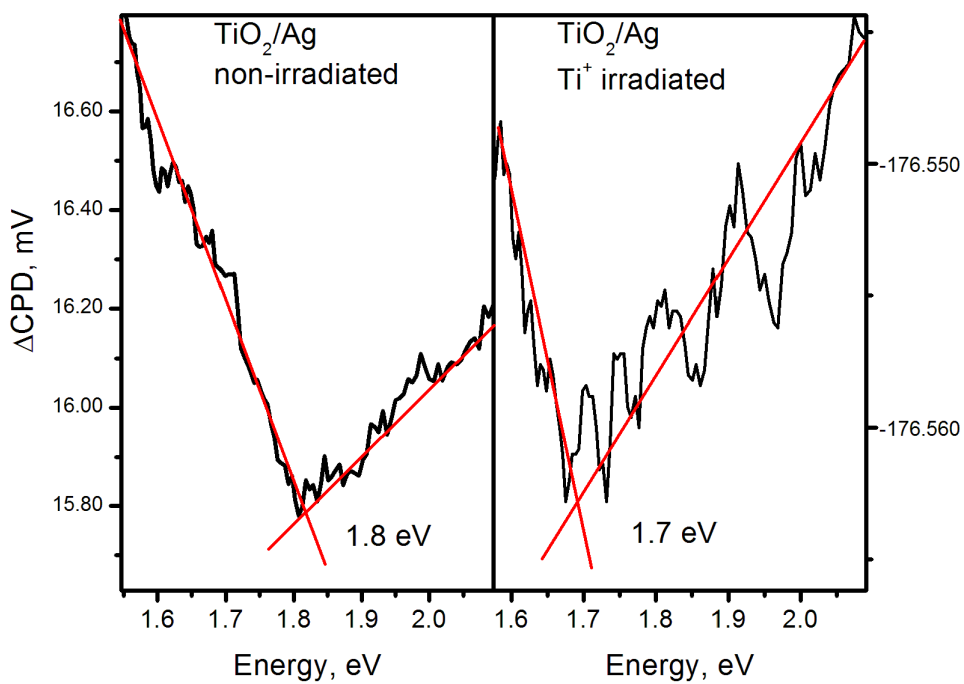


Figure 27. The SPV transition at ~ 1.7 - 1.8 eV observed in TiO_2/Ag film before and after Ti^+ irradiation.

Therefore, after low-energy Ti^+ irradiation no dramatic electronic structure changes were observed. This suggests that the studied films are chemically stable and robust. Further studies employing other irradiation types are necessary to confirm radiation-hardness of these specimens.

Conclusions

Based on the presented band gap diagrams, all the samples contain a significant number of oxygen deficiency-related defects. After addition of Ag to TiO_2 a new gap state is observed at ~ 1.8 eV which we assign to mixing of Ag $4d$ and Ti $3d$ states. In general, the electronic structure of TiO_2/Ag is quite different from that of the undoped TiO_2 , which could explain the enhanced visible light PC activity of TiO_2/Ag . For the TiO_2/Au system no significant changes were detected in comparison to the TiO_2 film and no states related to Au addition were observed. Addition of ZrO_2 does not induce Zr-related states. However, the number of states related to TiO_2 reduction increases, which could be the reason for the improved UV light PC activity of $\text{TiO}_2/\text{ZrO}_2$. Low energy Ti^+ irradiation did not significantly affect the gap structure of the films, demonstrating good radiation resistance and chemical stability of the studied specimens.

Chapter 4

4. Studies of optoelectronic characteristics of ZnO homoepitaxial thin films grown by atomic layer deposition

High quality single crystalline ZnO substrate wafers were purchased from Cermet, Inc.,. These wafers were prepared by the manufacturer by cutting hydrothermally grown ZnO boules perpendicular to the c axis and polished at the oxygen-terminated polar surface. The ZnO films were grown on those substrates at the University of Texas San Antonio (Prof. A. Chabanov's group) in a Savanna ALD instrument using diethylzinc and water as precursors. The films were grown at 120°C, 150°C and 200°C to a thickness of ~ 100 nm.

Among the three samples, the epilayer grown at 150°C had the best quality, as probed by XRD, TEM, PL and SPV. In particular, high resolution XRD measurements (not shown) demonstrate that although the film grown at 150°C is polycrystalline it has a strongly pronounced c -axis orientation. XRD-based reciprocal space mapping (RSM) analysis showed slight stress gradient in the obtained film. Overall the sample is textured, while the substrate and film peaks are not easily distinguished, which indicates their similar orientation.

High resolution transmission electron microscopy (HR TEM) images of the sample grown at 150°C reveal a very good epitaxy and a columnar structure of the grains strongly aligned with the c axis (see Figure 28). Inspecting the TEM image one can observe that extended defects are the source of formation of otherwise high-quality columnar grains. This is in good correlation with low temperature PL spectra, which point to the presence of extended defects in this sample as discussed below.

Grain boundaries

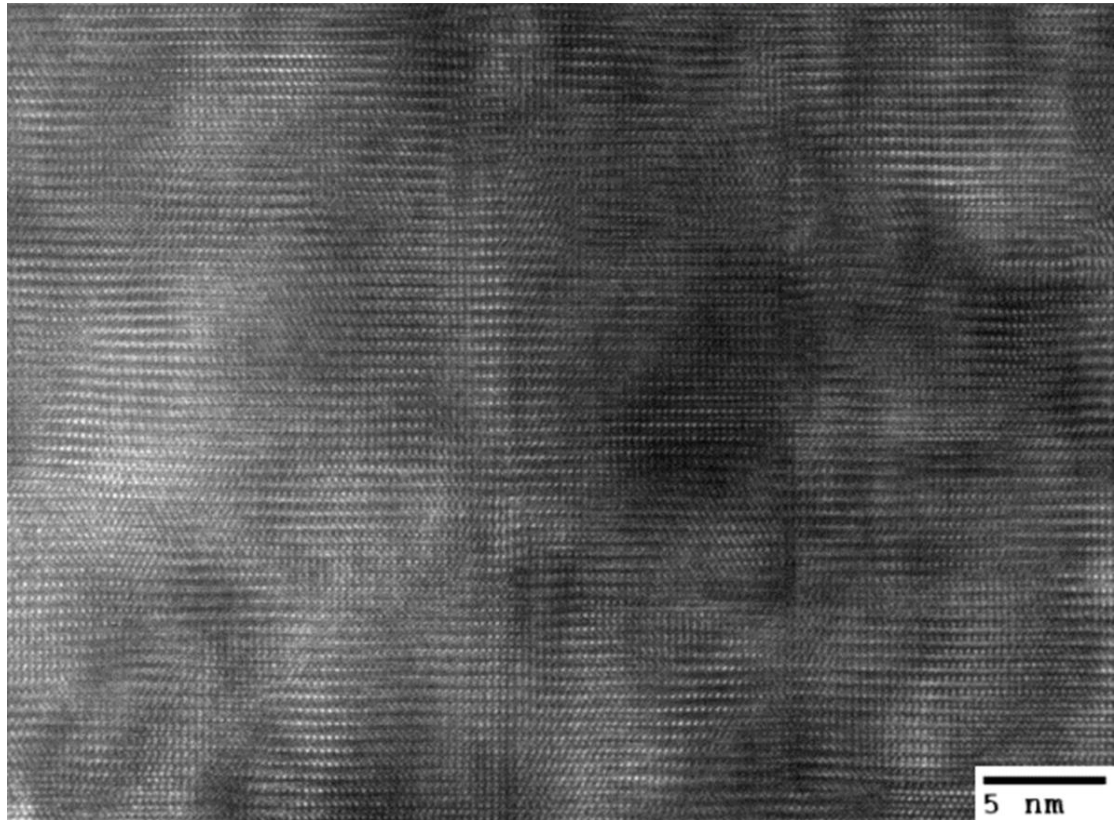


Figure 28. TEM image of ZnO thin film grown on O-face ZnO substrate at 150°C showing columnar growth and grain boundaries.

Our PL and SPV results confirmed the high quality of the epitaxial film grown at 150°C. PL spectra of this sample taken at room temperature and 8 K are presented in Figure 29. It should be noted that the thickness of the ALD-grown films is of the same order as the absorption depth of the laser radiation used for excitation (with a wavelength of 325 nm), thus the PL spectra could be attributed primarily to the grown thin films and not the underlying substrate. An SPV spectrum obtained for the sample grown at 150°C is shown in Figure 30. As one can see from these results, the “deep” defect signatures in the spectrum either have a very small relative intensity (PL) or non-observable (SPV), indicating low concentrations of visible luminescent centers and surface mid-gap traps.

By the same token, the near band edge luminescence is several orders of magnitude stronger than deep level emission, the low temperature excitonic lines are narrow, whereas the super-band gap SPV transition is sharp and well-defined.

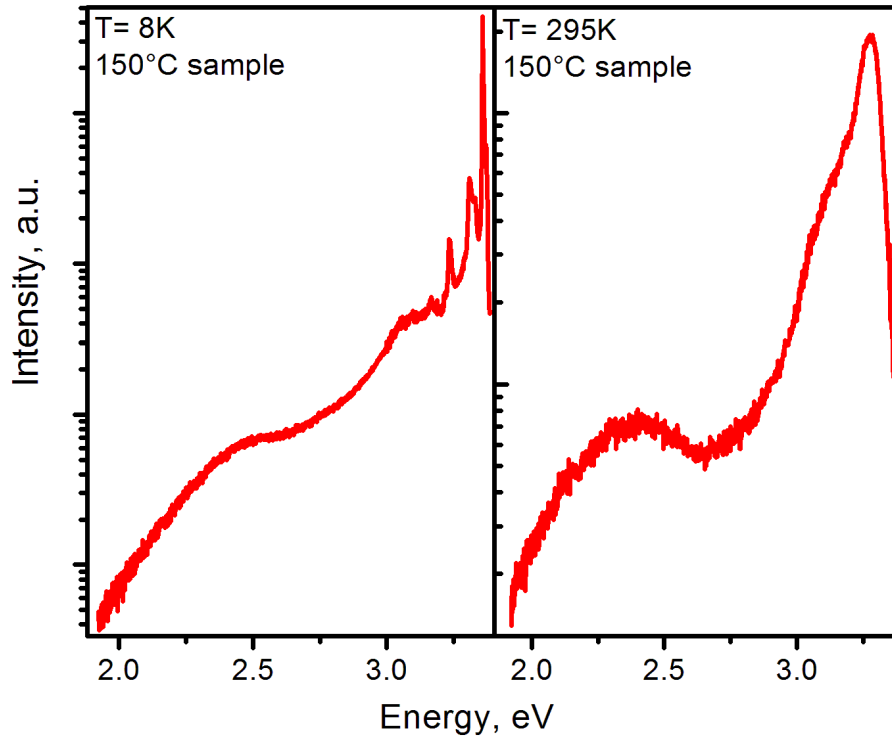


Figure 29. Low temperature (left) and room temperature (right) PL spectra of the ZnO thin film ALD-grown at 150°C.

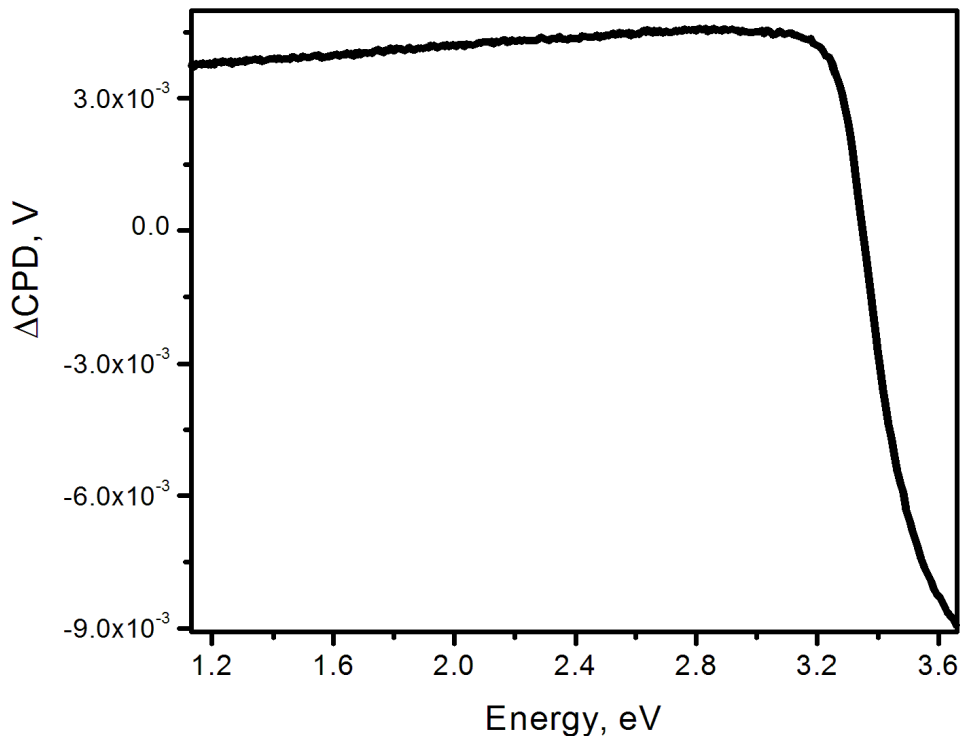


Figure 30. SPV spectrum of the ZnO film grown on a ZnO substrate at 150°C.

Detailed analysis of the excitonic luminescence in the low temperature PL spectrum reveals that there are three major BEx peaks present – I_4 , I_6 , and I_7 (using common notation for BEx lines⁸¹). Figure 31(A) shows evolution of these peaks' spectral positions and intensities with temperature in the 10 K- 55 K temperature range, as an example. To determine the energy positions of these peaks at every temperature, each spectrum is fitted with Lorentzians. The fitting procedure is similar to the one described above for TiO₂. The results of such fitting for the sample grown at 150°C are shown in Figure 31 (B).

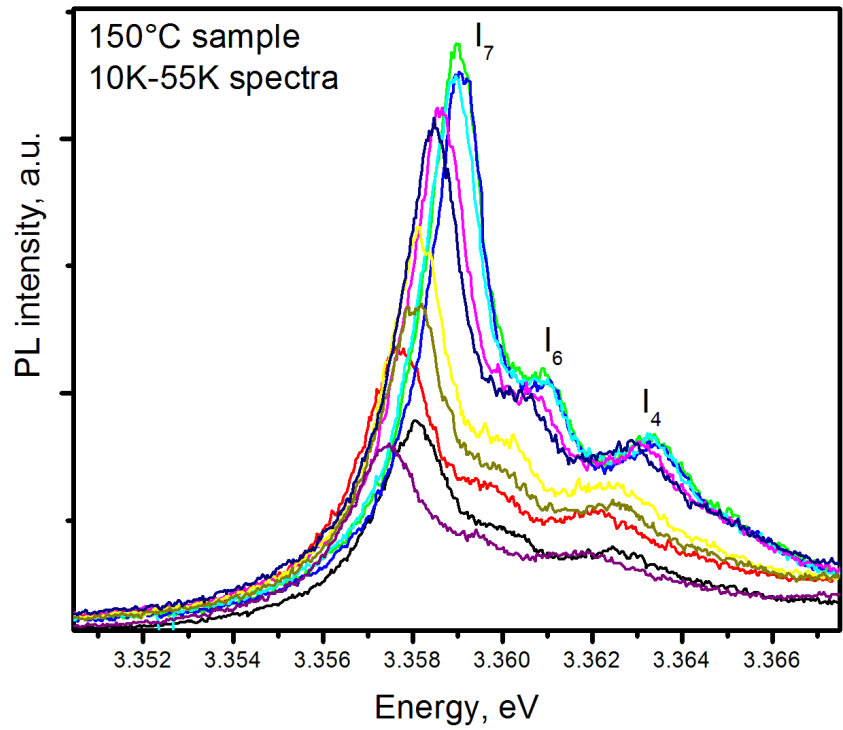


Figure 31 (A). Temperature dependence of the BEx peaks for the sample grown at 150°C in the 10 K - 55 K temperature range with a 5 K increment

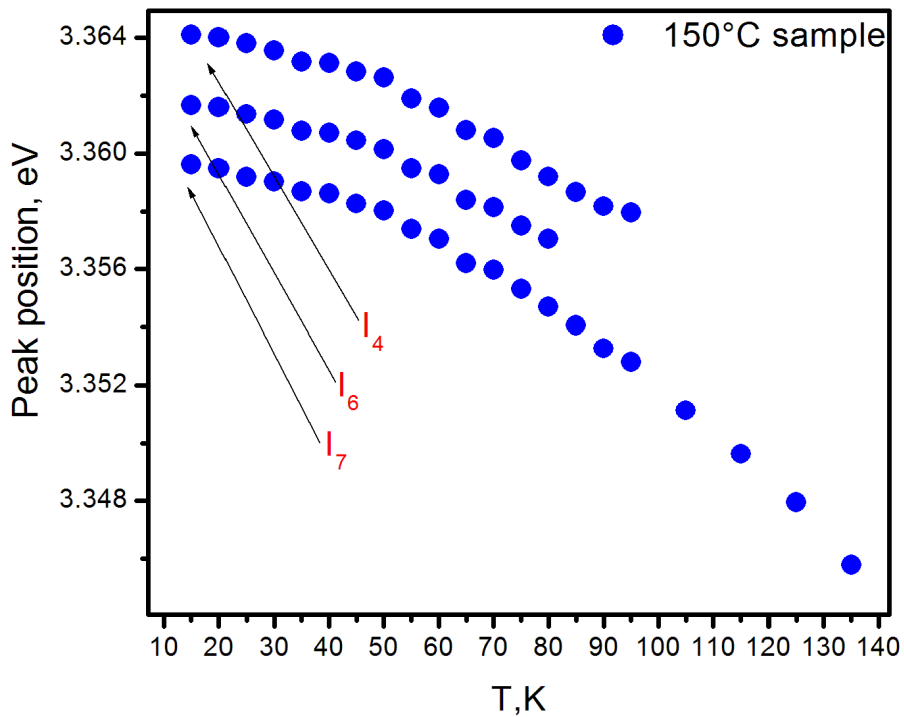


Figure 31(B). Temperature dependence of the excitonic peak positions for the sample grown at 150°C

The errors in peak positions for each fit were determined using the Origin software. They were $\sim 2 \mu\text{eV}$ for the I_7 peak, $\sim 9 \mu\text{eV}$ for the I_6 peak, and $\sim 8 \mu\text{eV}$ for the I_4 peak.

Figure 32 shows temperature dependence of the I_7 peak intensity for this sample. Following the literature,⁸¹ we assign the I_4 , I_6 , and I_7 BEx features to excitons bound to H neutral donor, Al neutral donor, and a neutral halogen donor. Such an assignment is not surprising since hydrogen is ubiquitous and participates in film synthesis, while aluminum can be incorporated during growth coming from Al-containing parts of the ALD apparatus. As mentioned in Chapter 2, temperature dependence of the BEx peak intensity provides information on the origins of the BEx peaks. This dependence is described by Eq. 2:

$$I(T) = \frac{I_0}{1 + Ae^{-E_a/kT}}$$

Using this formula to fit experimental data (Figure 31(A)) one can obtain the value of the activation energy, which oftentimes provides key information about the nature of the BEx recombination. Such fitting of the dependence shown in Figure 31A for I_7 yields activation energy of $\sim 19 \text{ meV}$ (Figure 32), in good agreement with previously reported values and the spectral location of the peak relative to the free excitonic features.

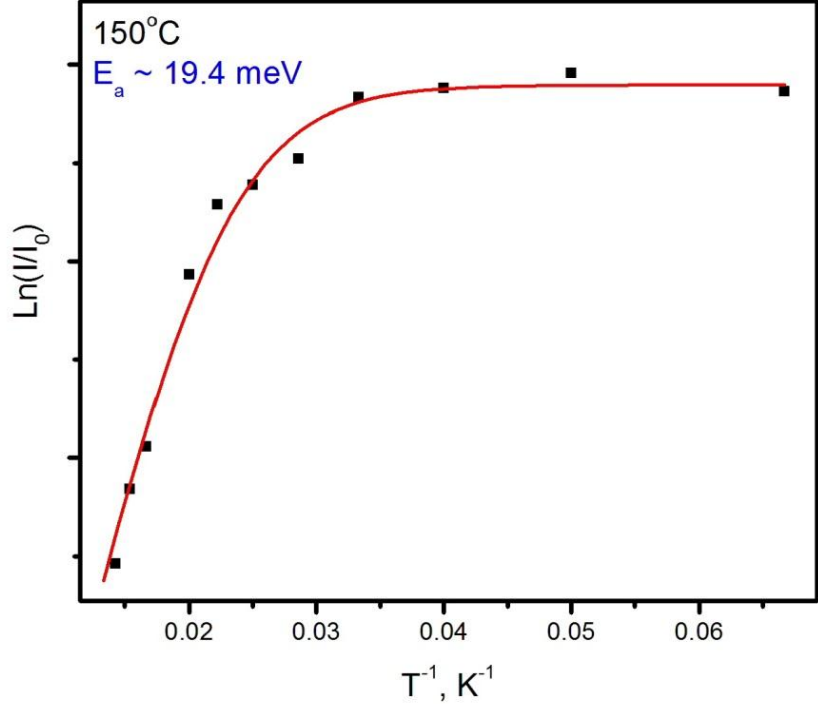


Figure 32. Temperature dependence of the intensity of the bound excitonic peak I_7 for the ZnO thin film grown at 150°C. The fit (red curve) to the theoretical dependence in Eq. 2 yields activation energy indicated in the graph.

In addition to the point defects discussed above (H, Al, halogen donor), PL measurements show that extended defects are present in the film grown at 150°C as well. A peak at ~ 3.33 eV observed in the low temperature PL spectrum of this sample (Figure 33) is commonly attributed to excitons bound to extended structural defects.⁸¹ In Ref. 89 the peak at 3.321 eV was attributed specifically to basal plane stacking faults in the ZnO layers ALD-grown on sapphire substrates. As mentioned above, HR TEM analysis of our sample grown at 150°C revealed significant amount of stacking faults (Figure 28). Our low temperature PL measurements support this conjuncture in good correlation with the TEM results. Therefore, the ZnO thin film grown at 150°C demonstrates excellent quality and overall low defect content.

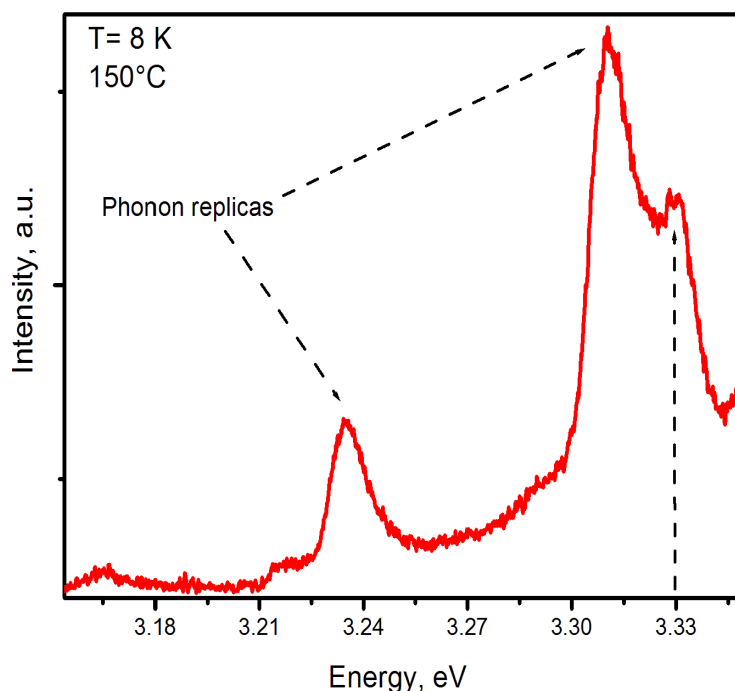


Figure 33. Low temperature PL spectrum of the ZnO film grown at 150°C demonstrating phonon replicas of the excitonic peaks and the ~ 3.33 eV peak related to the due to excitons bound to extended defects.

PL results for the samples grown at three different temperatures revealed a conspicuous resemblance at both room and low temperatures. Comparing the PL spectra for these samples (Figure 34) one can see that the near band edge luminescence is orders of magnitude higher than the deep level emission. All the samples exhibited the same BEx peaks, with similar temperature-dependent red shifts (Figure 35). The activation energies extracted from the temperature dependence of the I_7 peak intensity were also similar for all three samples (Figure 36). Also, the excitonic linewidth was not affected by the growth temperature and was ~ 1 meV at 8 K for all the samples, indicating similar lattice quality.

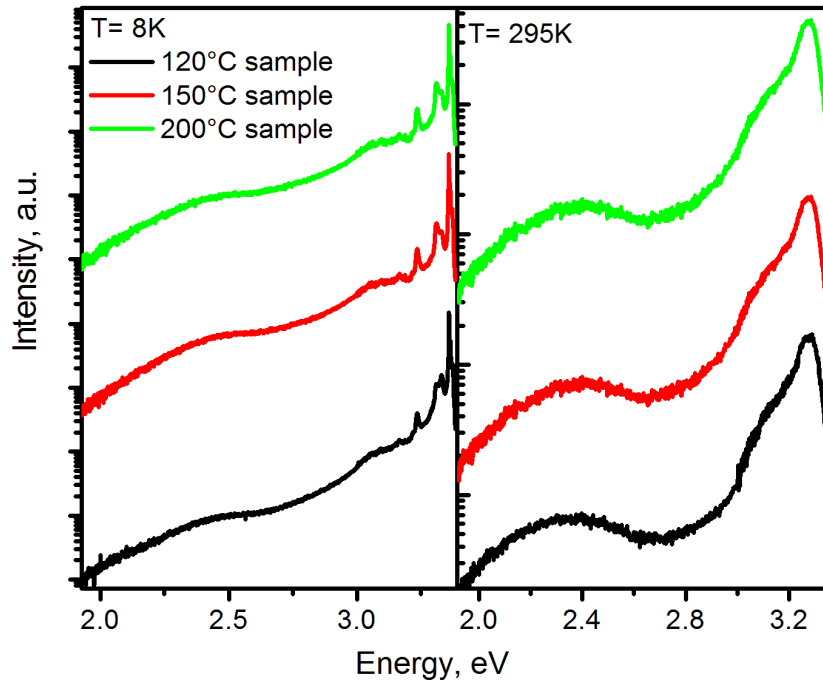


Figure 34. Low temperature (left) and room temperature (right) PL spectra of the ZnO thin films grown at three different temperatures.

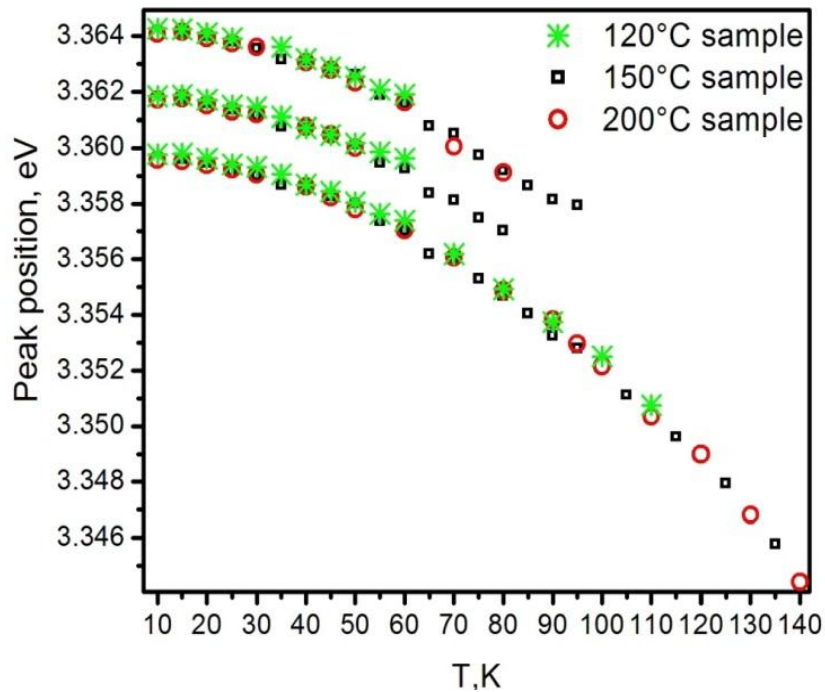


Figure 35. Temperature dependence of the excitonic peak positions for ZnO thin films grown at three different temperatures. The same red shifts are observed regardless of the growth temperature.

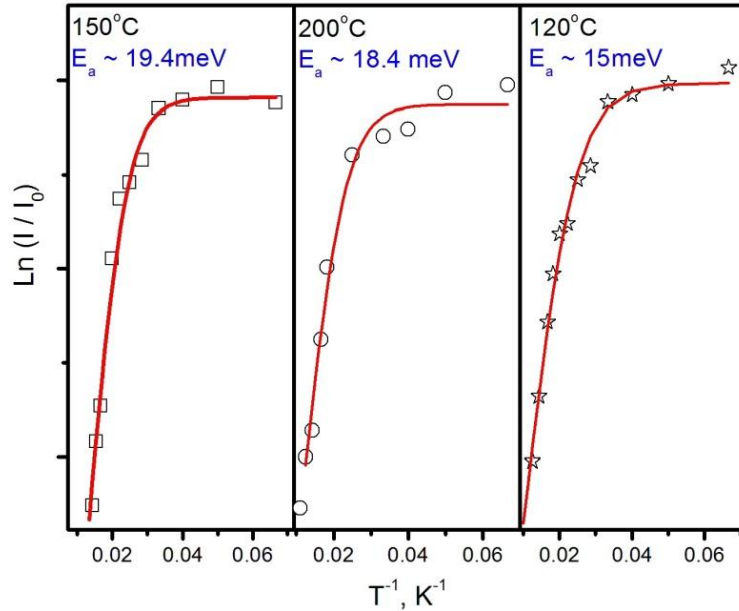


Figure 36. Temperature dependence of the intensity of the I_{7BEx} peak for the ZnO thin films grown at 120°C, 150°C and 200°C. The fits (red curves) to the theoretical dependence yield the activation energies indicated in the graphs.

These results demonstrate that the observed BEx emissions have the same nature for all the specimens grown at different temperatures. Therefore, the growth temperature does not significantly affect the type and relative abundance of point defects created during growth, making ALD homoepitaxial growth of high quality ZnO feasible in a wide range of relatively low temperatures.

Despite the many similarities in the optoelectronic properties of our samples, the thin films grown at different temperatures exhibited discrepancies associated with extended defects. For example, the relative intensity of the ~ 3.33 eV luminescence peak in the 8 K PL spectra (discussed above) was significantly greater for the sample grown at 120°C (cf. Figure 37).

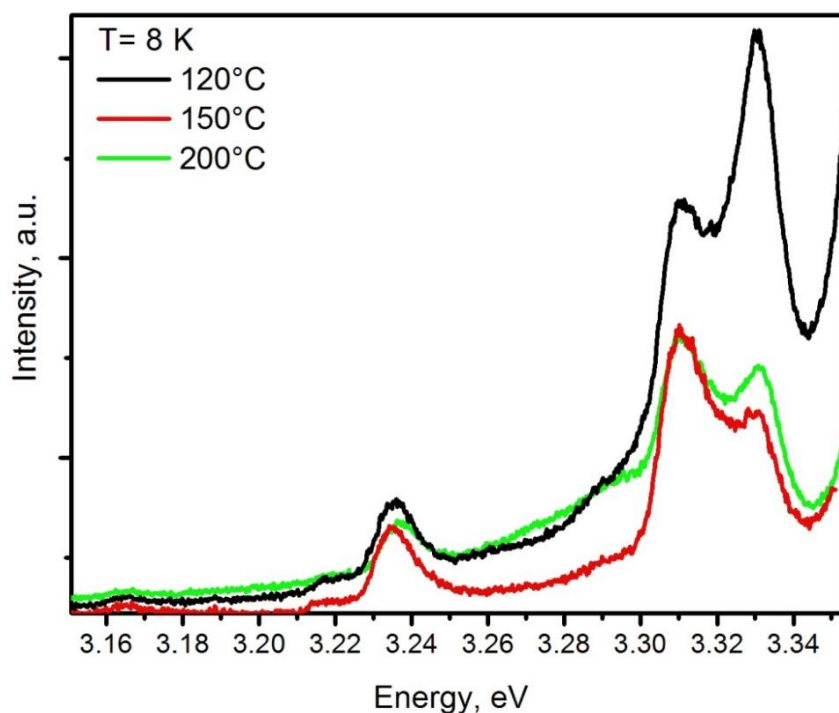


Figure 37. Low temperature PL spectra of the three ZnO films grown at different temperatures demonstrating the phonon replicas of the excitonic peaks and a varying relative intensities of the ~ 3.33 eV peak related to the excitons bound to structural defects.

The differences in the relative amount of extended defects (most likely stacking faults) in the samples grown at different temperatures can be correlated to reciprocal space mapping (RSM) results (not reported in detail here). RSM analysis gives information on the relative orientation of the substrate and the film, the preferred orientation of crystallites as well as sample texture (distribution of crystallographic orientations in a polycrystalline material).

As one can see in Figure 37, the PL spectra for the studied samples differ in the intensity of the peak at ~ 3.33 eV related to extended defects. The relative intensity of this peak, proportional to the concentration of extended defects, is much greater for the sample grown at 120°C . RSM for the texture of the three samples shows a trend consistent with this. For the samples grown at 150°C and 200°C exhibit a similar texture, with several sharp peaks. On the

other hand, for the sample grown at 120°C, the RSM results are rather different showing a single broad peak, which could indicate either a random texture or a significantly reduced average grain size. The latter option is fully consistent with the luminescence results shown in Fig. 34 demonstrating the efficiency of PL in resolving such ambiguities. Indeed, in our model, the sample grown at 120°C contains crystallites, still of high quality (Fig. 34), but which are smaller in size and thus have a greater abundance of grain boundaries and extended defects associated with them. Such differences in texture can strongly affect charge transport properties (e.g., mobility). Therefore, the temperature of the ALD growth can be used as a tool to fine-tune the properties of the homoepitaxial ZnO films.

The increased content of extended defects in the sample grown at 120°C could also lead to formation of point native defects and in turn influence the visible luminescence. Indeed, the deep level (visible) luminescence in the room temperature PL spectra was also different for the sample grown at 120°C, where the broad visible PL emission exhibited a substantial red shift (cf. Figure 38). The ~ 2.4 eV luminescence band is most often attributed to oxygen vacancies whereas the observed shift may indicate presence of the second lower-energy luminescent component usually associated with the Zn interstitial defects.

This suggests that formation of native defects associated with the stoichiometric oxygen deficiency is controlled by the ALD growth temperature and thereby could be engineered and optimized. For the sample grown at 120°C we don't exclude a direct relationship between the red shift in the visible luminescence and the higher relative intensity of the ~ 3.33 eV BEx line, though further studies would be necessary to confirm such a supposition. It is possible that temperature-mediated differences in the residual stress in thin films can have an impact on the defects and thus on the optoelectronic properties.

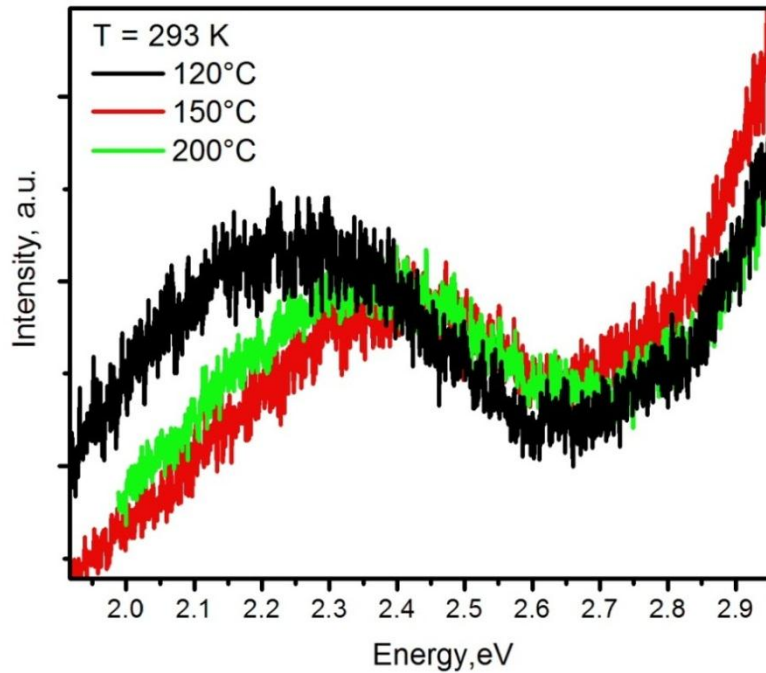


Figure 38. The visible luminescence range in the room temperature PL spectra of the ZnO samples grown at three different temperatures.

To conclude, we performed defect characterization of ZnO homoepitaxial thin films grown by ALD on ZnO substrates. The films were grown at three different substrate temperatures (120°C, 150°C and 200°C). We confirmed the high quality of all three specimens, but the sample grown at 150°C showed the best structural and defect-related characteristics. Unintentional contaminants are: Al, probably coming from the growth environment, and hydrogen. Growth temperatures affected the deep level luminescence and the concentration of extended defects. We contend that the suggested synthesis method can be a good foundation for the future production of *p-n* homojunctions.

Chapter 5

5. Optoelectronic surface-related properties in boron-doped and irradiated diamond thin films

Undoped and boron-doped diamond thin film samples used in this study were synthesized in a commercial ASTeX 5 kW microwave plasma-assisted CVD chamber on commercial Si(100) (Virginia Semiconductor Inc., Fredricksburg, VA) substrates. Briefly, Si wafers were ultrasonically rinsed in ethanol, followed by seeding with nanodiamond powder and the scratching residues introduced by ultrasonication served as nucleation sites. These films were deposited using CH₄/H₂/trimethylboron [TMB; B(CH₃)₃ for boron] source gas mixtures with [B]/[C]_{gas} = 0, 100, 1000, 2000, and 4000 ppm with a chamber pressure of ~ 40 Torr at the substrate temperature of ~ 720°C at 3.5 kW power and the growth time of 35 min yielding a thickness of ~ 200 nm. At the end of the deposition, the CH₄ and TMB gas flows were stopped and the films had continued exposure to H₂ plasma at 2 kW and 40 Torr for an additional 10 min. This post-growth annealing in atomic hydrogen served to gasify any unintentional nondiamond impurities, to minimize dangling bonds and to hydrogenate the surface. The boron concentration for the pristine B-doped films is estimated to be between 10¹⁸ cm⁻³ and 10²¹ cm⁻³ for all the samples using the Hall Effect.^{74,78,90,91} The diamond films were subjected to gamma radiation of 10³ kGy from a ⁶⁰Co source (12 kGy/h) at the Missouri University Research Reactor (MURR) at ambient temperature. Ultrananocrystalline diamond (UNCD) films were also grown with MPACVD technique using a similar chamber but with Ar gas instead of H₂ gas feedstock. Lastly, diamond thin films samples SG9 (with a higher B concentration) and SG10 (with a relatively lower B concentration) were grown using hot-filament chemical vapor deposition

(HFCVD) technique on Si (100) substrates employing hexaboride (B_2H_6) as a B-dopant (Courtesy of P. W. May, Bristol University-UK). Table 2 provides summary of the specimens used in this study.

Table 2 Description of studied diamond thin films

Sample ID	Growth technique	Growth/treatment parameters
UNCD	MPACVD	Undoped, in Ar dilution
Micro-diamond	MPACVD	Undoped, in high H_2 dilution
23B	MPACVD	in high H_2 dilution, 100 ppm of B in gas phase
20B	MPACVD	in high H_2 dilution, 2000 ppm of B in gas phase
19B-1	MPACVD	in high H_2 dilution, 4000 ppm of B in gas phase, pristine
19B-4	MPACVD	in high H_2 dilution, 4000 ppm of B in gas phase, gamma irradiated with dose of 10^3 kGy
27-1	MPACVD	in high H_2 dilution, 6427 ppm of B in gas phase
SG9	HFCVD	in high H_2 dilution, 3500 ppm of B in gas phase
SG10	HFCVD	in high H_2 dilution, 300 ppm of B in gas phase

Figure 39 shows scanning electron microscopy (SEM) images of the diamond thin films. SEM analysis provided a qualitative estimate of grain size by counting the number of grains over a certain area. The SEM micrographs yielded a grain size of > 200 nm for the least doped sample (100 ppm) that starts to turn relatively smaller grained with increasing boron concentration with feature sizes on the order of ~ 100 nm.⁷⁴

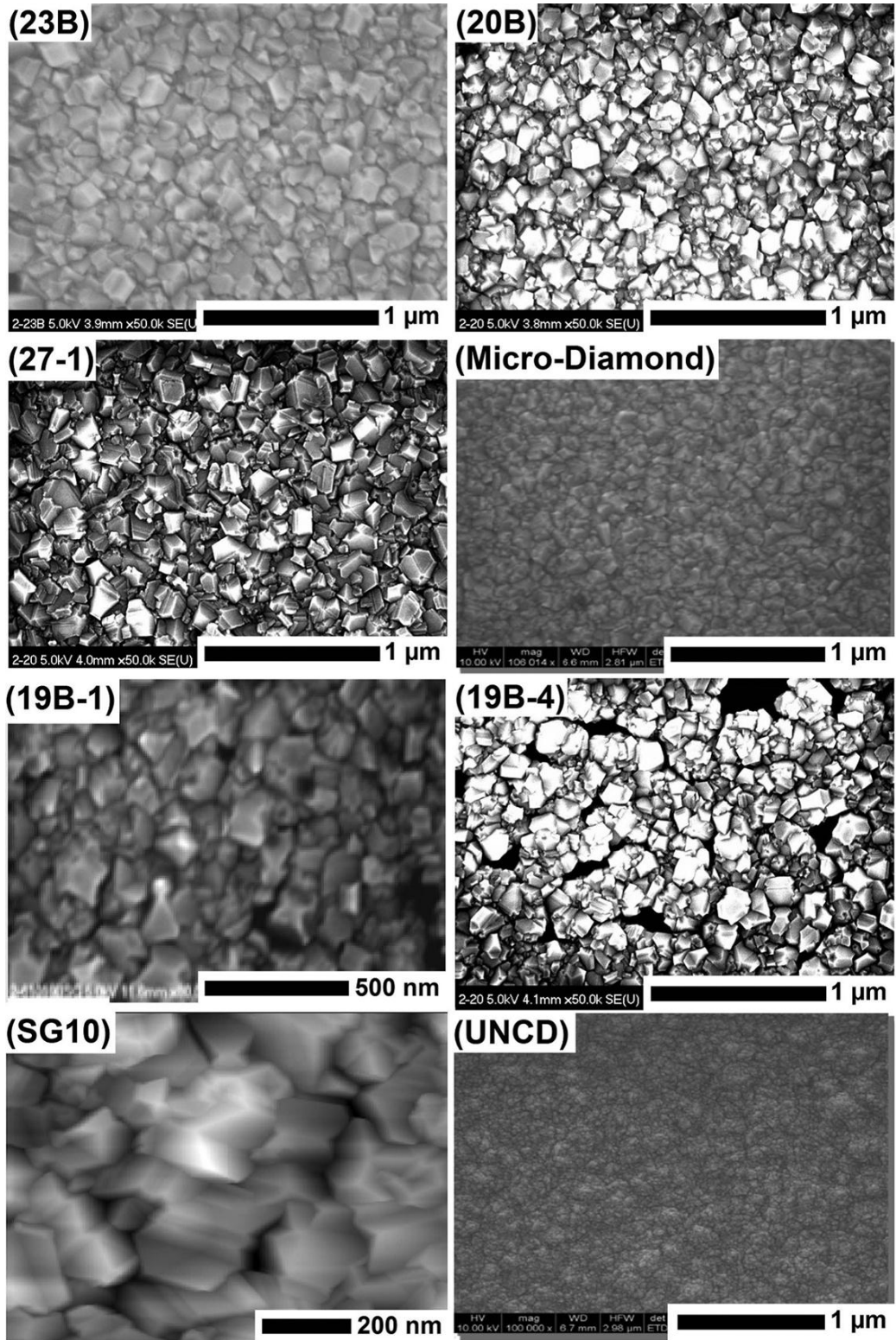


Figure 39. SEM images of the diamond thin film samples studied.

As we discussed above, SPV spectroscopy is able to detect surface states and determine their charge state as well as the donor versus acceptor-like character. This technique offers remarkable benefits such as identification of the conductivity type, conduction versus valence band nature of the electronic transitions, location of the defect states in the band gap, ability to detect surface state densities below 10^{10} cm^{-2} and surface state-related cross sections. Whereas research in diamond films is well-founded, its studies with SPV spectroscopy are largely missing. In recent years there were only a few published SPV studies of diamond^{92,93,94,95}, and most of them involved Kelvin probe microscopy without extraction of the spectroscopic information, and hence detailed characteristics of surface states. Moreover, these experiments were performed, as a rule, in ambient air. In our work, we implemented the spectroscopic SPV setup with *in vacuo* Kelvin probe offering a great deal of advantage in claiming true surface states as these films are rather sensitive to their surrounding environment. We obtained apparent and clear SPV spectral signatures of CVD-grown diamond films doped with boron and irradiated with gamma source.

In our SPV experiments there were two distinct types of spectral outcomes – either a spectrum with a good or at least a reasonable signal-to-noise ratio or essentially none. The best (i.e. least noisy) spectral response was observed for the undoped sample (UNCD). In the samples doped with a boron concentration in the gas phase up to 2000 ppm (samples ID: 23-B, SG10, 27-1) the signal-to-noise ratio was not as good as in the undoped sample, but still quite acceptable. The only exception was the 20-B sample, for which the signal-to-noise ratio was somewhat worse, yet the signal was still discernible. However, in samples with high doping levels, i.e. prepared with a relatively higher boron concentration above 2000 ppm (19B-1, SG9), the signal completely disappeared and the spectra contained only noise.

Yet, in the sample with a boron dose of 4000 ppm that was gamma irradiated with the dose of 10^3 kGy (19B-4) the signal re-emerged revealing a good signal-to-noise ratio.

Such behavior of the SPV signal, with its disappearance at high B doping levels and then re-appearance after the highly doped sample was gamma irradiated, is in a reasonably good agreement with the existence of an insulator-metal transition, which in B-doped diamond is predicted to occur for dopant concentrations above $\sim 2 \times 10^{20} \text{ cm}^{-3}$.⁹⁶ We argue that after the insulator-metal transition occurs in the conductive regions (especially at and near the surfaces of the grain boundaries) the separation of the electron-hole pairs at the surface, necessary to produce a non-zero SPV spectroscopic response, is disabled thus leading to the disappearance of the signal. Moreover, the reappearance of the SPV signal after irradiation also confirms the results reported in Ref. 74. The 19B-4 sample is showing the change in its electronic properties from the quasi-metallic to the semiconducting behavior similar to those doped with relatively lower concentrations as well as undoped diamond films. This may be the manifestation of the effect known as priming, i.e. improving the electronic properties of diamond through irradiation. Priming in diamond has been reported for gamma and pion irradiation.⁷⁴ For instance, in natural semiconducting diamond radiation was shown to compensate the boron acceptors to produce an insulating or a controlled impurity semiconducting material.^{74,78}

In all of the samples with observable SPV signal, the most prominent spectral element was the transition at $\sim 3.1\text{-}3.2$ eV (see Figure 40 for the 19B-4, 23-B, and 27-1 samples). It appears as a knee, with an upward change of the slope.⁹⁷ Even in the sample with a poorer signal-to-noise ratio (20-B) this transition was well pronounced. Naturally, the prevailing SPV transition at 3.1 eV is a reflection of the dominant surface state in the studied samples. In the literature the grain surfaces in a polycrystalline CVD diamond are presumed to be rather rich in the graphitic sp^2 bonded carbon. Clustering of sp^2 C was reported to form at grain boundaries.⁹⁸

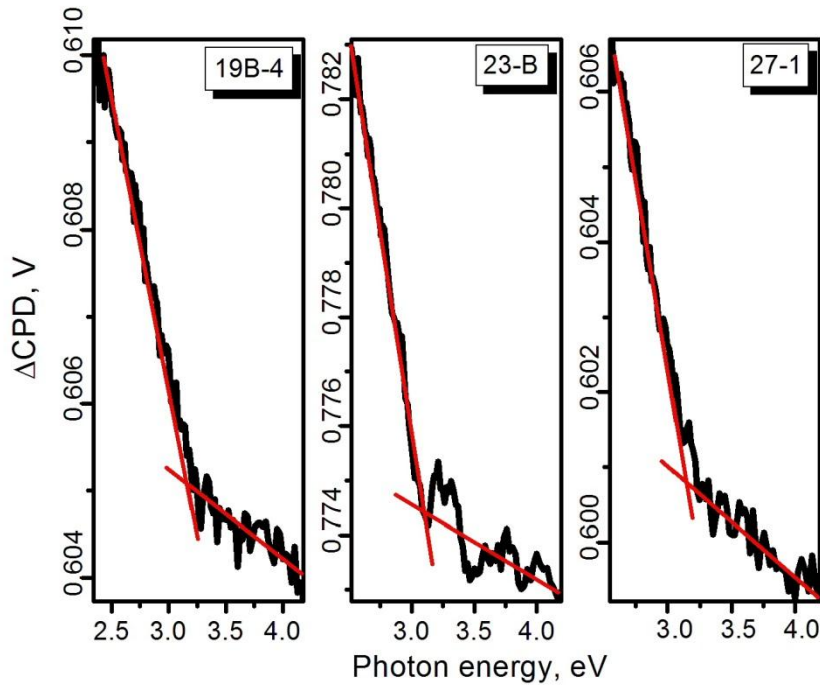


Figure 40. SPV transition for the surface state 3.1–3.2 eV above the top of the valence band for the samples 19B-4, 23B, and 27-1.

It has been reported recently^{99,100} that an electronic transition at 3.1 eV is observed in sp^2C clusters (and not necessarily in diamond) corresponding to an excitonic recombination. We therefore argue that the 3.1 eV SPV transition (as well as the 3.1 eV PL spectral feature, which we will discuss below) observed in our experiments corresponds to precisely this transition related to the sp^2C clustering phenomenon. Therefore, in our CVD diamond thin films the surface is rich in sp^2C clusters, which serve as a predominant channel for charge exchange via the surface states. In many samples studied here this “knee” (at 3.1 eV) looks akin to a super-band gap SPV transition which would be expected of the excitonic recombination. Several other SPV transitions, albeit weak, were observed in some specimens; however, they were not common and observed only in specific samples. For example, such transitions as ~ 1.9 eV in the

19B-4 and 23-B samples (not shown), etc. require more investigation to make unequivocal assignments to specific surface states.

In addition, in the spectra of several samples we observed periodic features in the 1.6 – 3.0 eV range. Such characteristic undulations were the most pronounced in the undoped UNCD sample (see Fig. 41 and inset schematic).

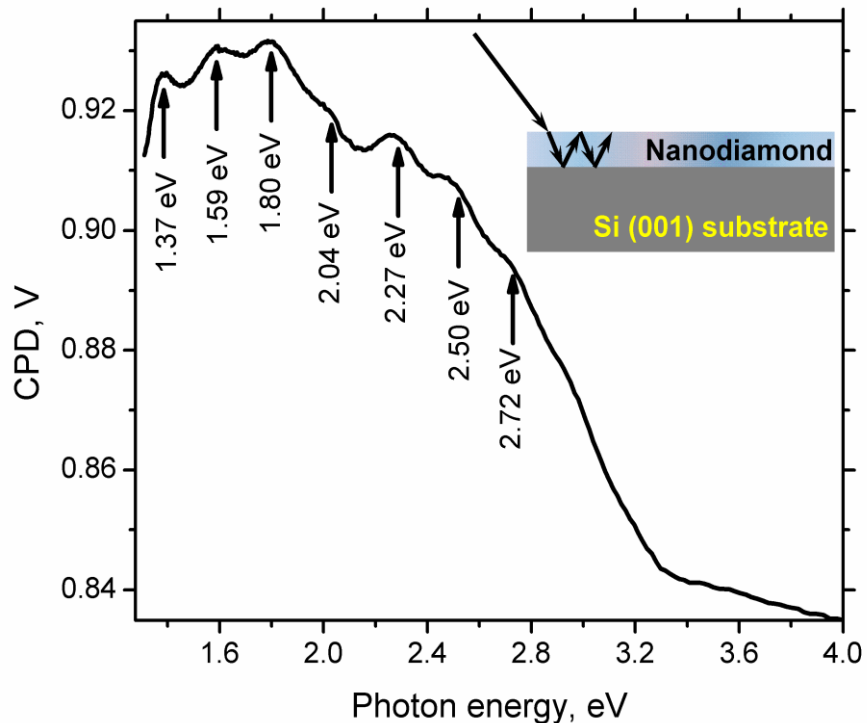


Figure 41. Undulations in the SPV spectrum of the UNCD sample. The inset diagram illustrates possible explanation of the undulations due to thin film interference.

The periodicity of these SPV spectral “oscillations” was ~ 0.2 eV. Such periodic features observed for the UNCD sample, as well as some others, could be explained as follows (see inset schematic in Fig. 41). The observed background of the SPV signal (essentially, the surface charge) is produced by the light incident on the sample from, as usual, the top surface (the diamond/vacuum interface). However, the refracted light may undergo multiple reflections

between the diamond/vacuum interface and the diamond/substrate interface (cavity resonance), especially if the thickness of the films is comparable with the wavelength of light. If, for a certain incident light wavelength, a destructive interference condition is satisfied, then there is no contribution to the production of the (vacuum) surface charge. However, if a constructive interference condition is satisfied, the light that is incident on the diamond/vacuum interface from beneath contributes to an additional surface charge generation, which corresponds to the maxima of these periodic spectral features. Observation of such interference depends on several factors, among them the relationship between the indices of refraction of the three media comprising the interfaces as well as the thickness of the diamond film. For our films the observed spectral periodicity of ~ 200 meV is in a good agreement with the geometry and make-up of the specimens. In principle, this interference is a nuisance obscuring the real defect-related SPV spectral features. For example, one can see in Fig. 41 that the spectral oscillations obscure possibly several transitions between 1.5 eV and 2.5 eV. In our future studies to eliminate this artifact we will attempt to make the thickness of the diamond films either non-uniform or incompatible with the range of the light wavelengths used in experiments.

PL spectra of all the samples were measured at room temperature and 8 K. Most samples in their PL spectra revealed three main luminescent features – broad bands at 2.4 eV and 2.9 eV and a weaker emission at ~ 3.1 - 3.2 eV, which most of the time was observed as a shoulder of the 2.9 eV spectral band. The absolute and relative intensities of the three emission peaks varied from sample to sample, and the examples of some of the spectra are shown in Figure 42.

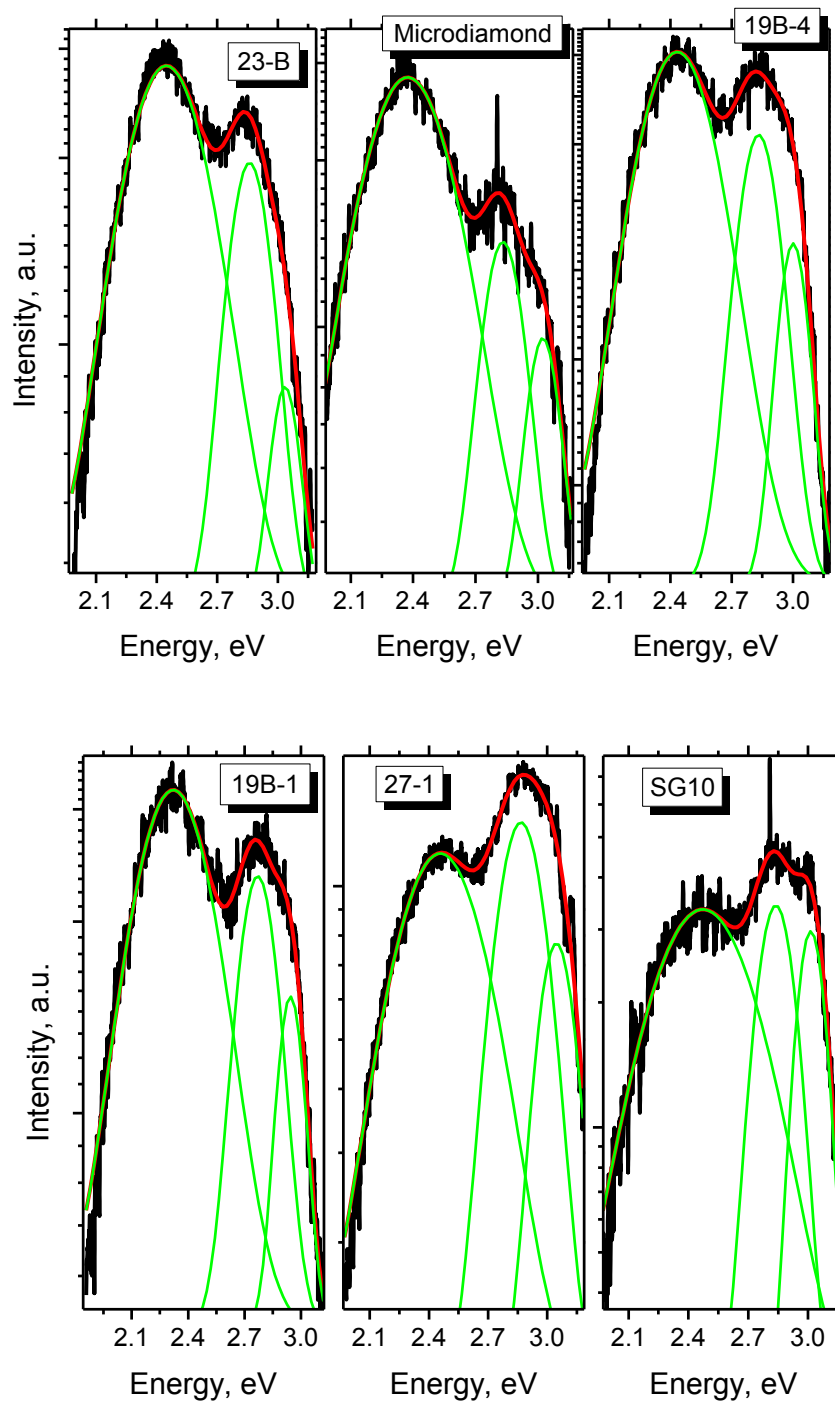


Figure 42. Visible parts of the low temperature (8 K) PL spectra for the 19B-4, 23B, Microdiamond, 19B-1, 27-1, and SG10 samples. Also shown is fitting obtained for each spectrum by a superposition of three Gaussian peaks at 2.4, 2.9, and 3.1 eV.

The most pronounced features in our PL spectra for the visible range, the two bands at ~ 2.4 eV and ~ 2.9 eV, are commonly observed in diamond. Whereas the latter feature, frequently referred to as an A-band, is ubiquitous in the luminescence of different diamond specimens and is attributed to microscopic structural defects, the former is often attributed to B doping. As can be seen in Figure 42, practically all spectra reveal a ~ 3.1 eV shoulder of the ~ 2.9 eV emission band. Unlike the more common 2.4 and 2.9 eV bands, the 3.1 eV emission is rather unusual for diamond. As discussed above, it is possible that it is associated with an excitonic luminescence in sp^2C clusters. Its relative weakness is probably related to primarily surface nature of this recombination (PL signal comes from both the surface and the bulk of the grain). Additional confirmation of this assumption can be found from the dependence of the relative intensity of this feature on the grain surface-to-volume ratio (Figure 43).

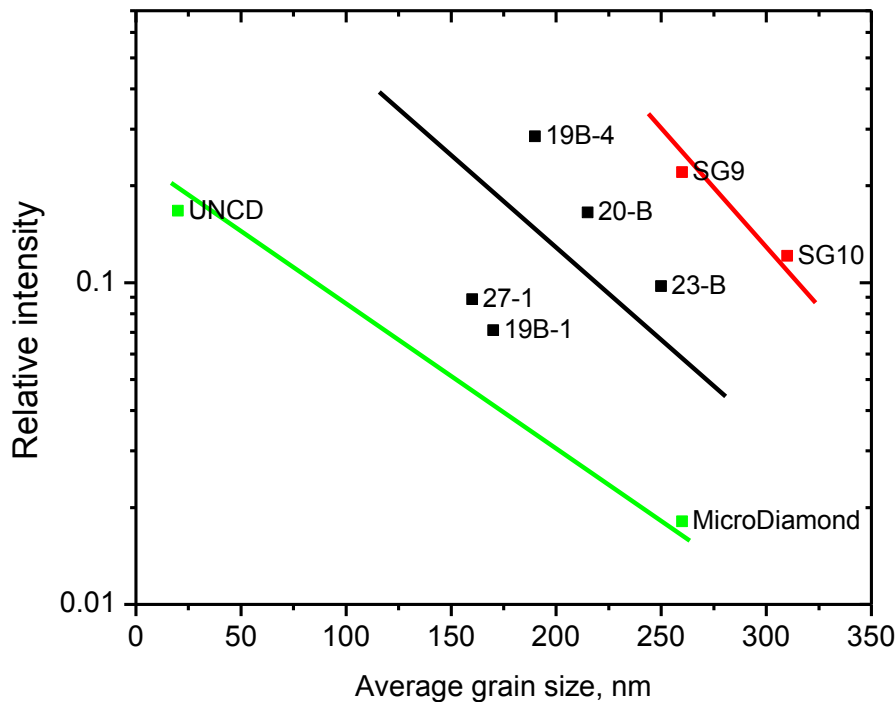


Figure 43. Dependence of the relative intensity of the PL band at 3.1 eV on the grain surface-to-volume ratio for three groups of diamond thin films – undoped, MPACVD-, and HFCVD-doped. The trend for the increase of the relative intensity of this feature with the decrease of the grain size is probably due the relative surface abundance the sp^2C clusters.

This dependence was obtained by fitting the visible part of the PL spectra with a superposition of three Gaussian peaks (see Figure 42). In Figure 43 one can see an obvious trend for the increase of the relative intensity of the 3.1 eV band with the decrease of the grain size for three groups of diamond thin films – undoped, MPACVD, and HFCVD doped diamond films. As was previously reported^{74,101}, the average grain size in CVD diamond thin films decreases with the increasing B concentration, probably driven by the relative surface abundance of boron in conjunction with the sp^2 bonded carbon during the deposition in the gas phase chemistry. Therefore, the trend observed in Figure 43 is an additional evidence confirming our assignment of the 3.1 eV transition to the sp^2 C clusters.

Notably, the PL spectra for the quasi-metallic samples (19B-1 and SG9) yielded a reasonable signal-to-noise ratio, unlike their SPV counterparts. This can be explained within the same set of arguments. Conductivity in our B-doped diamond (quasi-metallic conductivity included) is mediated by the boron acceptors primarily in the vicinity of the grain boundaries, which are also rich in the sp^2 carbon. On the other hand, the PL spectroscopy probes the entire volume of the samples, and thus the quasi-metallic samples yield signal from both the surface and the bulk, whereas the SPV spectra provide information primarily about the electronic processes in the vicinity of the surface, consequently yielding no meaningful signal for the quasi-metallic films. On a separate note, an interesting question would be whether the 2.4 eV band is truly related to the boron doping. We contend that in our samples it is not necessarily the case. The reason is that for the undoped samples the intensity of this luminescent transition was not weaker than in the B doped films (see Figure 42). In fact, there were earlier reports^{99,100} on the 2.4 eV luminescence in an undoped diamond where the authors attribute that to hydrogen. At this point, we leave the assignment for future investigations.

Besides, at 8 K many samples revealed yet another, very intense luminescence in the form of two narrow lines at ~ 3.32 and ~ 3.37 eV. Luminescent lines in exactly the same locations were recently reported for systems that include nanoscale Si-containing interfaces.^{102,103} For the Micro-diamond sample we ran temperature dependent spectra in the 3.25-3.42 eV range. Peak positions, intensities and widths of these depend on the temperature, as illustrated in Figure 44.

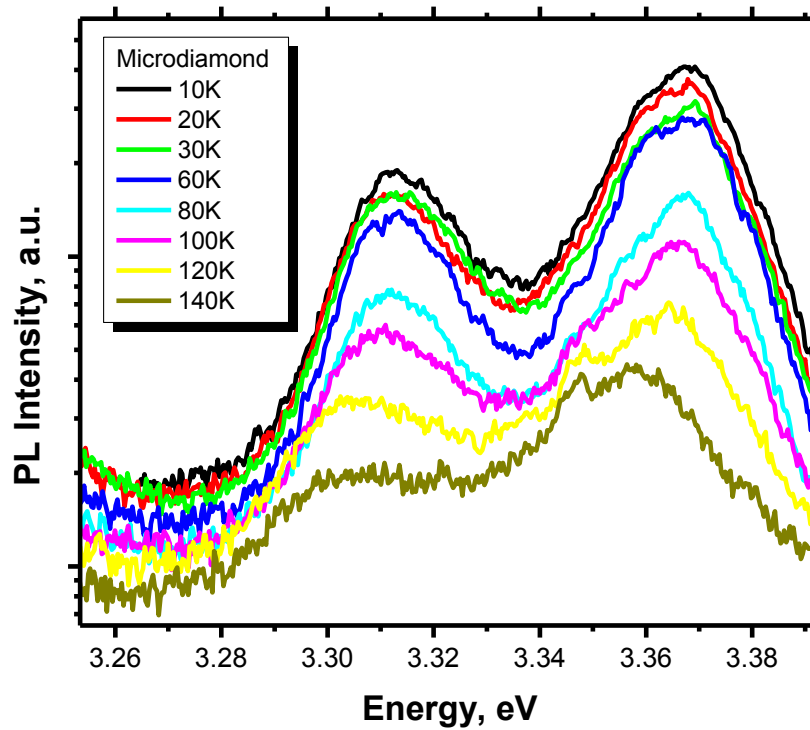


Figure 44. Temperature dependence of the PL spectra for the micro-diamond sample in the near-UV range featuring two narrow lines at 3.32 and 3.37 eV.

It is possible that in our samples this luminescence is produced not in the diamond films, but rather at the diamond/Si substrate interface where formation of nanoscale Si-containing structures is possible during the diamond film growth. The 325 nm UV laser beam goes through the diamond film, excites this UV luminescence at the interface, which in turn escapes the

diamond film mostly without any attenuation. This assumption is reinforced by the temperature dependence of the 3.32 eV and 3.37 eV peaks – see Figure 44 – which is very similar to that reported by other groups.¹⁰³

Thereby, employing PL and SPV spectroscopic probes, we thoroughly studied CVD diamond thin films with different levels of boron doping in conjunction with gamma irradiation effects. SPV measurements confirmed the earlier supposition that while the increase of the B concentration eventually leads to a semiconductor-metal transition, subsequent intense gamma irradiation reverts back the quasi-metallic samples to semiconducting state via the so called priming effect, in essence compensating electrical activity of boron acceptors through hydrogen. One of the most pronounced transitions observed in the SPV spectra was the 3.1 eV “knee”, also observed as a band or a shoulder in most of the PL spectra. We argue that this is a signature of the sp^2C clusters/layers in the vicinity of grain boundaries, consistent with our previous propositions. On the other hand, the 2.4 eV luminescence band, commonly attributed to boron impurities, was present in the undoped films as well, leading us to believe that this assignment may not be adequate and require further investigations.

Chapter 6

6. Conclusions

Titanium Dioxide

Using SPV and PL spectroscopy, we performed systematic studies of the electronic structure of sol-gel grown anatase TiO_2 , TiO_2/Ag , TiO_2/Au and $\text{TiO}_2/\text{ZrO}_2$ thin films. Our results can be summarized as follows.

1. We detected visible light-active gap states induced as a result of Ag, Au or ZrO_2 modifications of a sol-gel grown anatase TiO_2

Based on our PL and SPV studies we produced for the first time a systematic set of bandgap diagrams for the TiO_2/Ag , TiO_2/Au and $\text{TiO}_2/\text{ZrO}_2$. We established that all samples contain a significant number of oxygen deficiency-related gap states, which could be solar light-active.

In general, the electronic structure of TiO_2/Ag is quite different from that of the undoped TiO_2 , which could explain the enhanced visible light PC activity of TiO_2/Ag . Namely, in TiO_2/Ag in addition to oxygen deficiency-related defects new Ag-related gap state appears. This new state is observed at ~ 1.8 eV (above the VBM) and is assigned to mixing of Ag $4d$ and Ti $3d$ states. This state could be responsible for enhanced visible light activity of TiO_2/Ag .

For the TiO_2/Au system no significant changes were detected in comparison to the TiO_2 film and no states related to Au addition were observed. Only oxygen deficiency-related defects were present in this system. This conclusion is consistent with literature reports, which attribute visible light PC activity of TiO_2/Au to surface plasmon resonance absorption band in the visible range.

Addition of ZrO₂ does not induce Zr-related gap states. The number of states related to TiO₂ reduction increases, which could be the reason for the improved UV light PC activity of TiO₂/ZrO₂ reported in literature.

2. We analyzed the band structure of TiO₂, TiO₂/Ag, TiO₂/Au and TiO₂/ZrO₂ after Ti⁺ irradiation to trace its effects on the electronic structure

Low energy Ti⁺ irradiation did not significantly affect the electronic structure of the films, demonstrating good radiation resistance and chemical stability of the studied specimens, making them suitable for applications in harsh environments. Absence of dramatic gap structure changes can be due to low beam energy (~ 10 nm penetration depth) and/or non-uniform concentration of native defects prior to self-doping.

Future studies of the photoactivity of the films would be necessary to elucidate the contribution of the newly created states.

Zinc Oxide

We also analyzed homoepitaxial thin films of ZnO grown by ALD synthesized on single crystalline ZnO substrates at several different temperatures. Below is a synopsis of our results.

1. We determined the overall quality of the resulting ZnO layers ALD-grown on ZnO substrates

All studied films revealed good crystallinity and low concentration of defects. At room temperature, the intensity of the intrinsic defect-related emission was several orders of magnitude lower than the intensity of the bandgap emission. At low temperature, the line widths of the BEx peaks were as narrow as 1 meV. The SPV analysis showed very low concentration of surface traps. These results suggest that ALD synthesis method is suitable for homoepitaxy in a relatively wide temperature range.

2. We obtained information about the nature of defects in the as-grown ZnO films

Several defect signatures were identified in our samples. Among native defects there are extended defects as well as O vacancies and Zn interstitials. Unintentional contaminants are Al, probably coming from the growth environment, and the omnipresent hydrogen. High resolution microscopy studies showed that stacking faults are present in the films as well.

3. We established optimum conditions for obtaining films with a minimal concentration of defects

The studied ZnO layers were grown at three different substrate temperatures – 120°C, 150°C and 200°C. The sample grown at 150°C showed the best optoelectronic properties. The substrate temperature, which had a relatively weak effect on the overall quality of the thin films, can be used to fine-tune the defect properties.

We contend that the suggested synthesis method is adequate for the future production of *p-n* ZnO homojunctions.

Diamond

Employing PL and SPV we studied CVD diamond thin films with different levels of boron doping in conjunction with gamma irradiation effects. The following questions were addressed in our work.

1. What is the primary mechanism of conductivity in boron-doped diamond thin films? Is there any correlation with the microstructure?

We argue that conductivity in our B-doped diamond is mediated by the boron acceptors primarily in the vicinity of the grain boundaries, which are also rich in the sp^2 carbon. Additionally, the surface is rich in sp^2 carbon clusters, which serve as a predominant channel for charge exchange via the surface states. One of the most pronounced transitions observed in the

SPV spectra for diamond thin films was the 3.1 eV “knee”, also observed as a band or a shoulder in most of the PL spectra. We argue that this is a signature of the sp^2C clusters/layers in the vicinity of grain boundaries, consistent with our previous propositions.

2. What is the effect of increasing boron doping levels? What are the effects of gamma irradiation on films' conductivity?

SPV measurements confirmed the supposition that while the increase of the B concentration eventually leads to a semiconductor-metal transition, subsequent intense gamma irradiation reverts back the quasi-metallic samples to semiconducting state via the so called priming effect, in essence compensating electrical activity of boron acceptors through hydrogen.

Chapter 7

7. Future Work

TiO₂

Our studies of TiO₂ could help develop a new direction in our lab. Firstly, it would be interesting to study the correlation between the growth parameters and the stoichiometry of pristine TiO₂ thin films. This would greatly contribute to the understanding of the factors influencing the visible light-activated photocatalytic reaction at the surface of pristine TiO₂. For this project, the ability to grow large batches of TiO₂ samples in the lab is crucial. Recently we started growing TiO₂ thin films in our lab by the sol-gel spin-coating method. This procedure was adopted from Ref. [104] and the first results are rather promising. Figure 45 shows the low temperature PL spectrum of one of the grown films together with the actual picture of the obtained sample.

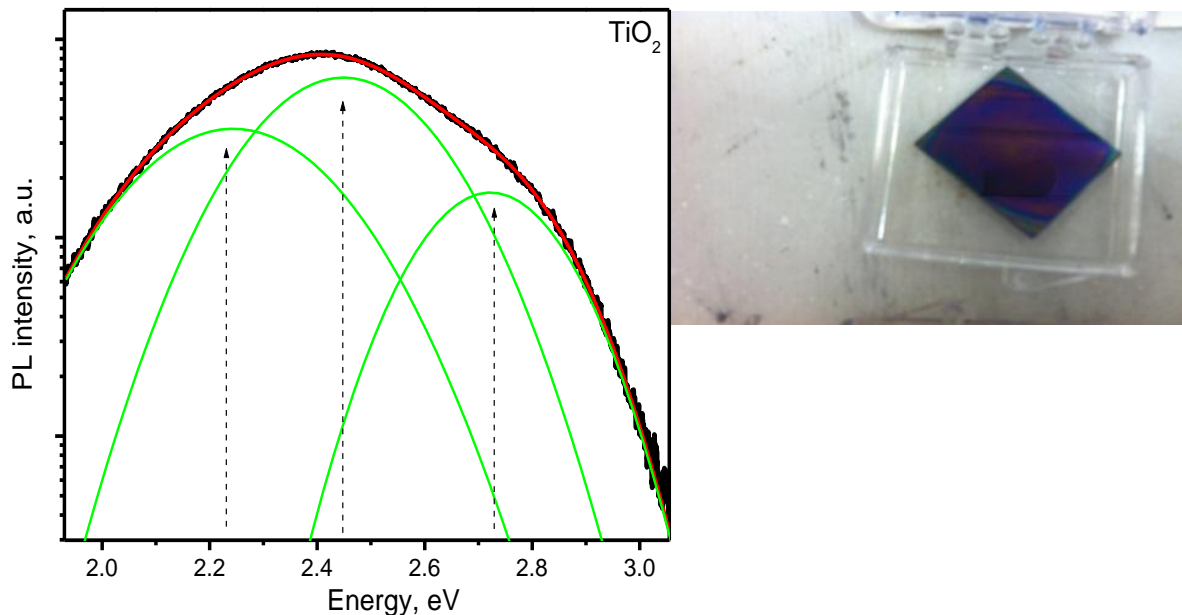


Figure 45. Low temperature (10 K) PL spectrum (left) of the TiO₂ film (right) synthesized in our lab.

Preliminary results show that growth parameters affect the relative intensities of PL bands related to native defects. Since these defects absorb visible light, the effect on the visible light PC activity of TiO₂ is expected. It would be desirable to correlate the native defect characteristics with the photocatalytic activity of the as-grown samples. Therefore a custom-built setup, where we can perform actual photocatalytic activity measurements is needed. Studies of the PC activity of such systems could isolate which type and content of native defects has a beneficial impact on PC reactions activated by visible light.

ZnO

As we observed in this work, the temperature of the substrate during the ALD growth could be used to tune the defect properties of the ZnO thin films. Studies of the effects of other ALD parameters on ZnO films' quality is a subject of future work. Such growth parameters as pulsing or purging times could be optimized to minimize structural defects.

Diamond

As we observed in this study, graphitic content at the grain boundaries in diamond thin films is strongly related to the conductivity and microstructure. In future studies it would be beneficial to investigate nanodiamond specimens in various configurations with well-controlled grain sizes and graphitic surface phase abundances.

References

- ¹ R. Ramesh and D. G. Schlom, *MRS Bulletin* **33**, (2008).
- ² A. Rahman, I. Ali, S.M. Al Zahrani, and R. H. Eleithy, *NANO* **6**, 185 (2011).
- ³ A.G. King, *Journal of Chemical Education* **87**, (2010).
- ⁴ L. Xiong, J. Li, B. Yang, and Y. Yu, *Journal of Nanomaterials*, **2012**, 1 (2012).
- ⁵ D. C. Look, G. C. Farlow, P. Reunchan, S. Limpijumnong, S. B. Zhang, and K. Nordlund
Physical Review Letters **95**, 225502 (2005).
- ⁶ N. Serpone, *J. Phys. Chem. B* **110**, 24287 (2006).
- ⁷ R. M. Sheetz, I. Ponomareva, E. Richter, A. N. Andriotis, M. Menon, *Physics Review B* **80**,
195314 (2009).
- ⁸ X. Chen and S. S. Mao, *Chem. Rev.* **107**, 2891 (2007).
- ⁹ U. Diebold, *Surface Science Reports* **48**, 53 (2002).
- ¹⁰ S. G. Kumar and L. G. Devi, *J. Phys. Chem. A* **115**, 13211 (2011).
- ¹¹ M. Tahir, N. A. Amin, *Energy Conversion and Management* **76** 194 (2013).
- ¹² B. J. Morgan and G. W. Watson, *J. Phys. Chem. C* **114**, 2321 (2010).
- ¹³ T. K. Tseng, Y. S. Lin, Y. J. Chen and H. Chu, *Int. J. Mol. Sci.* **11**, 2336 (2010).
- ¹⁴ T. A. Kandiel, A. Feldhoff, L. Robben, R. Dillert, and D. W. Bahnemann, *Chem. Mater.* **22**
2050 (2010).
- ¹⁵ D. J. Kima, S. H. Hahn, **57**, 355, (2002).
- ¹⁶ E. Finazzi, C. Di Valentin, and G. Pacchioni, *J. Phys. Chem. C* **113**, (2009).
- ¹⁷ G. Mattioli, P. Alippi, F. Filippone, R. Caminiti, and A. A. Bonapasta, *J. Phys. Chem. C* **114**,
21694 (2010).
- ¹⁸ T. Sekiya, S. Kamei, S. Kurita, *Journal of Luminescence* **87** 1140-1142 (2000).

- M. Scepanovic, Z. D. Dohcevic-Mitrovic, I. Hinic, M. Grujic-Brojcic, G. Stanisic, and Z. V. Popovic, *Materials Science Forum* **494**, 265 (2005).
- ¹⁹ A. Rothschild, A. Levakov, Y. Shapira, N. Ashkenasy, and Y. Komem, *Surface Science* **532**, 456 (2003).
- ²⁰ K. Iijima, M. Goto, S. Enomoto, H. Kunugita, K. Ema, M. Tsukamoto, N. Ichikawa, H. Sakama *Journal of Luminescence* **128**, 911 (2008).
- ²¹ M. Nolan, S. D. Elliott, J. S. Mulley, R. A. Bennett, . M. Basham, P. Mulheran *Physics Review B* **77**, 235424 (2008).
- ²² N. D. Abazovic, M. I. Cyomor, M. D. Dramicanin, D. J. Jovanovic, S. P. Ahrenkiel, and J. M. Nedeljkovic, *J. Phys. Chem. B*, **110**, 25366 (2006).
- ²³ H. Zhang, C. Xie, Y. Zhang, G. Liu, Z. Li, C. Liu, X. Ma, and W. F. Zhang *Journal of Applied Physics* **103**, 103107 (2008).
- ²³ S. Battiston, A. Leto, M. Minella, R. Gerbasi, E. Miorin, M. Fabrizio, S. Daolio, E. Tondello, and G. Pezzotti, *J. Phys. Chem. A*, **114**, 5295 (2010).
- ²⁴ D. Fang, K. Huang, S. Liu and J. Huang, *J. Braz. Chem. Soc.* **19**, 1059 (2008).
- ²⁵ G. Boschloo and D. Fitzmaurice, *J. Phys. Chem. B* **103**, 2228 (1999).
- ²⁶ F. Montoncello, M. C. Carotta, B. Cavicchi, M. Ferroni, and A. Giberti, C. Malagu and G. Martinelli, F. Meinardi, *Journal of Applied Physics* **94**, (2003).
- ²⁷ C. Di Valentin, G. Pacchioni, A. Selloni, *J. Phys. Chem. C* **113**, 20543–20552 (2009) and ref. therein.
- ²⁸ V. Kiisk, I. Sildos, A. Suisalu, J. Aarik *Thin Solid Films* **400** 130–133 (2001).
- ²⁹ S. Guha, K. Ghosh, J. G. Keeth, S. B. Ogale, S. R. Shinde, *Applied Physics Letters* **83** (2003).
- ³⁰ G. Pezzotti, A. Leto, S. Battiston, M. Minella, and W. Zhu, *Journal of Applied Physics* **111**, 103720 (2012).

- ³¹ H. Tang, F. Levy, H. Berger, and P. E. Schmid, *Physical Review B* **52**, (1995) and references therein.
- ³² J. Preclikova, P. Galar, F. Trojanek, S. Danis, B. Rezek, I. Gregora, Y. Nemcova, and P. Maly *Journal of Applied Physics* **108**, 113502 (2010).
- ³³ S. G. Lu, Z. K. Xu, H. Chen, C. L. Mak, K. H. Wong, K. F. Li, and K. W. Cheah, *Journal of Applied Physics* **99**, 064103 (2006).
- ³⁴ Y. Cao, L. Jing, X. Shi, Y. Luan, J. R. Durrant, J. Tang and H. Fu *Phys. Chem. Chem. Phys.*, **14**, 8530 (2012).
- ³⁵ J. Nowotny, T. Bak, M. K. Nowotny, and L. R. Sheppard *J. Phys. Chem. B* **110**, 18492 (2006)
- ³⁶ M. D. Hernandez-Alonso, I. Tejedor-Tejedor, J.M. Coronado, J. Soria, and M.A. Anderson, *Thin Solid Films* **502**, 125 (2006).
- ³⁷ X. Zhifu, L. Clark, Q. Yang, and M.A. Anderson *Environ. Sci. Technol.* **30** 647 (1996)
- ³⁸ J. H. Richter, P. G. Karlsson, and A. Sandella_ *Journal of Applied Physics* **103**, 094109 (2008)
- ³⁹ C. Sun, L. Liu, L. Qi, H. Li, H. Zhang, Ch. Li, F. Gao, L. Dong *Journal of Colloid and Interface Science* **364** 288 (2011).
- ⁴⁰ V. Subramanian, E. Wolf, and P. V. Kamat *J. Phys. Chem. B* **105** 11439 (2001).
- ⁴¹ K. Awazu, M. Fujimaki, C. Rockstuhl, J. Tominaga, H. Murakami, Y. Ohki, N. Yoshida, and T. Watanabe, *J. Am. Chem. Soc.* **9** (2008).
- ⁴² 43 M. A. Debeila, M. C. Raphulu, E. Mokoena, M. Avalos, V. Petranovskii, N. J. Coville, and M. S. Scurrrell, *Materials Science and Engineering A* **396**, 70 (2005).
- ⁴³ L. Dolgov, V. Kiisk, V. Reedo, A. Maaros, I. Sildos, and J. Kikas, *Phys. Status Solidi A* **207**, 1166 (2010).
- ⁴⁴ K. Zakrzewska, M. Radecka, A. Kruk, W. Osuch, *Solid State Ionics* **157** 349– 356 (2003)
- ⁴⁵ Y. Tian and T. Tatsuma, *J. Am. Chem. Soc.* **127**, (2005).

- ⁴⁶ H. Xing-Gang, L. An-Dong, H. Mei-Dong, L. Bin, and W. Xiao-Ling, *Chin. Phys. Lett.* **26**, 077106 (2009).
- ⁴⁷ Y. Zhu, W. Wei, Y. Dai, B. Huang, *Applied Surface Science* **258** 4806 (2012).
- ⁴⁸ Z. Yang, R. Wu, D. W. Goodman, *Physical Review B* **61** (2000).
- ⁴⁹ X. Liu, S. Gao, H. Xu, Z. Lou, W. Wang, B. Huang, and Y. Dai *Nanoscale* **5**, 1870 (2013)
- ⁵⁰ A. V. Krasheninnikov and K. Nordlund, *Journal of Applied Physics* **107**, 071301 (2010)
- ⁵¹ C. G. Van de Walle, *Physical Review Letters* **85** (2000).
- ⁵² S. Lany and A. Zunger, *Physical Review Letters* **98**, 045501 (2007) and references therein.
- ⁵³ C. H. Ahn, Y. Y. Kim, D. C. Kim, S. K. Mohanta, and H. K. Choa *Journal of Applied Physics* **105**, 013502 (2009).
- ⁵⁴ X. L. Wu, G. G. Siu, C. L. Fu, and H. C. Ong, *Applied Physics Letters* **78**, (2001).
- ⁵⁵ B. K. Meyer, H. Alves, D. M. Hofmann, W. Kriegseis, D. Forster, F. Bertram, J. Christen, A. Hoffmann, M. Straßburg, M. Dworzak, U. Haboeck, and A. V. Rodina, *Phys. Stat. Sol. (b)* **241**, 231 (2004).
- ⁵⁴ M. R. Wagner, T. P. Bartel, R. Kirste, A. Hoffmann, J. Sann, S. Lautenschläger, B. K. Meyer, C. Kisielowski, *Physical Review B* **79**, 035307 (2009).
- ⁵⁵ S. Kim, S. Jeong and B. Lee, *Semicond. Sci. Technol.* **22** 683 (2007).
- ⁵⁶ H. Matsui and H. Tabata, *Applied Physics Letters* **101**, 231901 (2012).
- ⁵⁷ D. Ehrentraut, H. Sato, Y. Kagamitani, A. Yoshikawa, T. Fukuda, J. Pejchal, K. Polak, M. Nikl, H. Odaka, K. Hatanakad and H. Fukumura, *J. Mater. Chem.* **16**, 3369 (2006).
- ⁵⁸ I. Bisotto, C. Granier, S. Brochen, A. Ribeaud, P. Ferret, G. Chicot, J. Rothman, J. Pernot, and G. Feuillet, *Applied Physics Express* 095802 (2010).
- ⁵⁹ M.W. Cho, C. Harada, H. Suzuki, T. Minegishi, T. Yao, H. Ko, K. Maeda, and I. Nikura, *Superlattices and Microstructures* **38**, 349 (2005).

- ⁶⁰ C. Klingshirn, *Phys. Stat. Sol. (b)* **244**, 3027 (2007).
- ⁶¹ H. Wensch, V. Kirchner, S.K. Hong, Y.F. Chen, H.J. Ko, T. Yao, *Journal of Crystal Growth* **227–228**, 944 (2001).
- ⁶² H. Matsui, H.Saeki, T. Kawai, A. Sasaki, M. Yoshimoto, M. Tsubaki, and H. Tabata, *J. Vac. Sci. Technol. B* **22**, (2004).
- ⁶³ T. Nakamura n, K. Masuko, A. Ashida, T. Yoshimura, N. Fujimura, *Journal of Crystal Growth* **318**, 516 (2011).
- ⁶⁴ K. Watanabe a, K. Matsumoto, Y. Adachi, T. Ohgaki, T. Nakagawa, N. Ohashi, H. Haneda, I. Sakaguchi, *Solid State Communications* **152**, 1917 (2012).
- ⁶⁵ K. Ogata, K. Maejima, Sz. Fujita, Sg. Fujita, *Journal of Crystal Growth* **248**, 25 (2003).
- ⁶⁶ K. Ogata, T. Kawanishi, K. Maejima, K. Sakurai, S. Fujita and S. Fujita, *Jpn. J. Appl. Phys.* **40**, L657 (2001).
- ⁶⁷ I.C. Robin, P.Marotel , A.H.El-Shaer, V.Petukhov, A.Bakin, A.Waag, M.Lafossas, J.Garcia, M. Rosina, A.Ribeaud, S.Brochen, P.Ferret, G.Feuillet, *Journal of Crystal Growth* **311**, 2172 (2009).
- ⁶⁸ H. von Wenckstern, M. Brandt, H. Schmidt, C. Hanisch, G. Benndorf, H. Hochmuth, M. Lorenz, and M. Grundmann, *Journal of the Korean Physical Society* **53**, 3064 (2008).
- ⁶⁹ N. El-Atab, S. Alqatari, F. B. Oruc, T. Souier, M. Chiesa, A. K. Okyay, and A. Nayfeh, *AIP Advances* **3**, 102119 (2013).
- ⁷⁰ Y. Kawamura, N. Hattori, N. Miyatake, M. Horita, and Y. Uraoka, *Japanese Journal of Applied Physics* **50** 04DF05(2011).
- ⁷¹ E. Przewdziecka, L. Wachnicki, W. Paszkowicz, E. Lusakowska, T. Krajewski, G. Luka, E. Guziewicz and M Godlewski, *Semicond. Sci. Technol.* **24** 105014 (9pp) (2009).

- ⁷² E Guziewicz, M Godlewski, L Wachnicki, T A Krajewski, G Luka1, S Gieraltowska, R Jakiela, A Stonert, W Lisowski, M Krawczyk, J. W Sobczak and A Jablonski, *Semicond. Sci. Technol.* **27** 074011, 1 (2012).
- ⁷³ E. Guziewicz, I. A. Kowalik, M. Godlewski, K. Kopalko, V. Osinniy, A. Wojcik, S. Yatsunenکو, E. Usakowska, W. Paszkowicz, and M. Guziewicz, *Journal of Applied Physics* **103**, 033515 (2008).
- ⁷⁴ S. Gupta, M. Muralikiran, J. Farmer, L. R. Cao, and R.G. Downing, *J. Mater. Res.* **24**, (2009).
- ⁷⁵ R. J. Tapper, *Rep. Prog. Phys.* **63**, 1273 (2000).
- ⁷⁶ P. W. May, *Phil. Trans. R. Soc. Lond. A* **358**, 473 (2000).
- ⁷⁷ A. Nemashkalo, P. R. Chapagain, R. M. Peters, J. Farmer, S. Gupta, and Y. M. Strzhemechny, *J. Appl. Phys.* **111**, 023704 (2012).
- ⁷⁸ S. Gupta, J. Farmer, D. Daghero, and R. Gonnelli, *J. Mater. Res.* **25**, 444 (2010).
- ⁸⁰ L. Kronik, Y. Shapira, *Surface Science Reports* **37**, 1-206 (1999).
- ⁸¹ B. K. Meyer, H. Alves, D. M. Hofmann, W. Kriegseis, D. Forster, F. Bertram, J. Christen, A. Hoffmann, M. Straßburg, M. Dworzak, U. Haboek, and A. V. Rodina, *Phys. Stat. Sol. (b)* **241**, 231 (2004).
- ⁸² J. Zhong, G. Saraf, H. Chen, Y. Lu, H. M. Ng, T. Siegrist, A. Parekh, D. Lee, and E. A. Armour, *Journal of Electronic Materials* **36**, 654 (2007).
- ⁸³ N. Kumar, R. Kaur, and R.M. Mehra, *Journal of Luminescence* **126**, 784 (2007).
- ⁸⁴ J. Grabowska, A. Meaney, K. K. Nanda, J.- P. Mosnier, M. O. Henry, J.-R. Duclère, and E. McGlynn, *Physical Review B* **71**, 115439 (2005).
- ⁸⁵ Handbook for Auger Electron Spectroscopy, L.E. Davis, N. C. MacDonald, P. W. Palmberg, G. E. Riach, and R.E. Weber, *Physical Electronics Industries* (1978).
- ⁸⁶ Studies of surface states in Zinc Oxide nanopowders”, by Raul Peters, Dissertation (2010).

- ⁸⁷ R. Liu, P. Wang, X. Wang, H. Yu, and J. Y., *J. Phys. Chem. C* **116**, 17721 (2012).
- ⁸⁸ J. C. Yu, J. Lin, and R. W. M. Kwok, *J. Phys. Chem. B* **102**, 5094 (1998).
- ⁸⁹ S. Yang, C.C. Kuo, W. R. Liu, B.H. Lin, H. C. Hsu, C. H. Hsu, and W. F. Hsieh, *Applied Physics Letters* **100**, 101907 (2012).
- ⁹⁰ E. Bustarret, P. Achatz, B. Sacepe, C. Chapelier, C. Marcenat, L. Ortega and T. Klein, *Phil. Trans. R. Soc. A* **366**, 267 (2008).
- ⁹¹ T. Klein, P. Achatz, J. Kacmarcik, C. Marcenat, F. Gustafsson, J. Marcus, E. Bustarret, J. Pernot, F. Omnes, B. E. Sernelius, C. Persson, A. F. da Silva, and C. Cytermann, *Phys. Rev. B* **75**, 165313 (2007).
- ⁹² A. Hoffman, A. Lafosse, and R. Azria, *Phys. Rev B* **73**, 085423 (2006).
- ⁹³ Rezek and C. E. Nebel, *Diamond & Related Materials* **14**, 466 (2005).
- ⁹⁴ B. Rezek, C. Sauerer, C.E. Nebel, M. Stutzmann, J. Ristein, L. Ley, E. Snidero, and P. Bergonzo, *Appl. Phys. Lett.* **82**, 14, 2266 (2003).
- ⁹⁵ B. Rezek, J. Cermak, A. Kromka, M. Ledinsky, P. Hubik, J. J. Mares, A. Purkrt, V. Cimrova, A. Fejfar, and J. Kocka, *Nanoscale Research Letters* **6**, 238 (2011).
- ⁹⁶ E. A. Ekimov, V. A. Sidorov, E. D. Bauer, N. N. Melnik, N. J. Curro, J. D. Thompson, and S. M. Stishov, *Nature* **428**, 542 (2004).
- ⁹⁷ A. Hoffman, A. Lafosse, and R. Azria, *Phys. Rev. B* **73**, 085423 (2006).
- ⁹⁸ A. Ilie, A. C. Ferrari, T. Yagi, and J. Robertson, *Appl. Phys. Lett.* **76**, 2627 (2000).
- ⁹⁹ D. Ghosh, G. Subhasha, C. H. Lee, and Y. K. Yap, *Appl. Phys. Lett.* **91**, 061910 (2007).
- ¹⁰⁰ J. Xu, J. Mei, X. Huang, W. Li, Z. Li, X. Li, and K. Chen, *Journal of Non-Crystalline Solids* **481**, 338 (2004).
- ¹⁰¹ S. Gupta, A. Dudipala, O. A. Williams, K. Haenen, and E. Bohannon, *J. Appl. Phys.* **104**, 073514 (2008).

¹⁰² X. Yang, X. L. Wua, S. H. Li, H. Li, T. Qiu, Y. M. Yang, P. K. Chu, and G. G. Siu, *Appl. Phys. Lett.* **86**, 201906 (2005).

¹⁰³ A. K. Singh, K. G. Gryczynski, F. D. McDaniel, S. Y. Park, M. Kim, and A. Neogi, *Applied Physics Express* **3**, 102201 (2010).

¹⁰⁴ Ch.-Ch. Chang, J.-Y. Chen, T.L. Hsu, C. K. Lin, and C. C. Chan, *Thin Solid Films* **516** 1743 (2008).

VITA

Personal Background	Daughter of Baynyat Ramakaeva and Boris Nemashkalo
Education	Bachelor of Science, Physics V. N. Karazin Kharkiv National University, Ukraine, 2009 Doctor of Philosophy, Physics Texas Christian University, Fort Worth, 2014
Experience	Teaching Assistantship, Texas Christian University Fort Worth, 2009-2014 Graduate Assistantship, Texas Christian University Fort Worth, 2013-2014
Professional Memberships	Materials Research Society

1. "Optoelectronic surface-related properties in boron-doped and irradiated diamond thin films", A. Nemashkalo, P. R. Chapagain, R. M. Peters, J. Farmer, S. Gupta and Y. M. Strzhemechny, *Journal of Applied Physics* (Volume 111, Issue 2, 2012), <http://dx.doi.org/10.1063/1.3678004>
2. "Photoluminescence of Surface Modified Silicon Carbide Nanowires", Polite D. Stewart, Ryan Rich, A. Nemashkalo and T. W. Zerda, *MRS Proceedings* (Volume 1350, 2011), doi:10.1557/opl.2011.1101
3. "Optical studies of electronic band structure in sol-gel anatase TiO₂ modified by Ag, Au, ZrO₂, and Ti⁺-irradiation", *ready for submission*
4. Optoelectronic Properties of High-Quality ZnO Thin Films Grown by Atomic Layer Deposition on Single Crystalline ZnO Substrates, *in preparation*

ABSTRACT

PHOTOLUMINESCENCE AND SURFACE PHOTOVOLTAGE STUDIES OF DEFECTS AT NANOSCALE SURFACES AND INTERFACES IN THIN FILMS OF ZnO, TiO₂ AND DIAMOND

By Anastasiia Nemashkalo, Ph.D., 2014
Department of Physics and Astronomy
Texas Christian University

Dissertation Advisor:
Dr. Yuri M. Strzhemechny, Associate Professor of Physics

The electronic properties of nanomaterials are greatly affected by their surfaces, which often contain significant numbers of defects that induce localized bandgap states. These localized states may have a significant impact on a material's optical absorption spectrum, conductivity, and charge dynamics – characteristics that are important in applications. The focus of the present work was on the surface defect properties of thin films of titanium dioxide, zinc oxide and diamond. Experimental methods sensitive to the spectral signatures of surface and bulk defects (photoluminescence and surface photovoltage spectroscopy) were used to estimate the electronic structure of each of these materials.

Band diagrams of TiO₂, TiO₂/Au, TiO₂/Ag, and TiO₂/ZrO₂ thin films have been obtained. The results suggest that all TiO₂-based films contain a significant number of native defect-related gap states. In addition, a new energy level at ~ 1.8 eV was detected in TiO₂/Ag and specifically attributed to the added Ag. The electronic structure of TiO₂/Au did not differ significantly from that of TiO₂. After the addition of ZrO₂, the number of native defect-related states increased. The TiO₂-based samples were also subjected to low energy Ti⁺-irradiation followed by similar

gap structure studies. The results are discussed relative to photocatalytic applications of the studied materials.

The optoelectronic properties of homoepitaxial ZnO thin films synthesized by the atomic layer deposition method were also studied. The films were grown at different temperatures in order to study the effects of growth conditions on the defect concentration. Surface photovoltage and temperature-dependent photoluminescence studies showed that our ZnO thin films have low concentrations of defects and excellent crystallinity. The growth temperature, however, has only a slight effect on the overall quality of the films.

Lastly, diamond thin films grown by the chemical vapor deposition method were studied. The films were doped with different amounts of boron and some were gamma irradiated. The mechanism for conductivity in diamond thin films with different boron concentrations was also studied. The impact of gamma irradiation on the films' conductive properties was investigated.